REPUBLIQUE ALGERIENNE DEMOCRATIQUE ET POPULAIRE
MINISTERE DE L'ENSEIGNEMENT SUPERIEUR ET DE LA RECHERCHE SCIENTIFIQUE
UNIVERSITE AMAR TELIDJI, LAGHOUAT

Faculté des Sciences
Département : Sciences de la Matière

Thèse de Doctorat 3ème cycle en physique

Option : Physique des matériaux

Par

ALLAL Adel

THEME

Etude ab-initio des propriétés physiques des nouveaux matériaux de sulfures de terres rares et d'alcalins ABS_2

Soutenue publiquement le: 26/06/2021

Devant le jury :

Mr: HELIFA Bachir	*Maître de conférences A, U. de Laghouat*	Président
Mr: HALIT Mohamed	*Professeur, U. de Laghouat*	Rapporteur
Mme: SAIB Salima	*Professeur, U.de M'sila*	Co-Encadreur
Mr: GUEDDOUH Ahmed	*Maître de conférences A, U. de Laghouat*	Examinateur
Mr: BENMAKHLOUF Abdennour	*Maître de conférences A, U. de Laghouat*	Examinateur
Mr: IBRIR Miloud	*Professeur, U. de M'sila*	Examinateur
Mr: BAADJI Nadjib	*Professeur, U. de M'sila*	Examinateur

2020-2021

Dedication

I dedicate this thesis

To my parents, for always supporting and encouraging me.

To my brothers, my sisters and my brother's wife

ملخص

حظيت أشباه الموصلات ABS_2 باهتمام كبير في السنوات الأخيرة. نظرًا لامتلاكها فجوات واسعة، فقد أصبحت مرشحًا واعدًا للعديد من التطبيقات مثل الإلكترونيات المحمولة ، الصمامات الثنائية الباعثة للضوء (LED) والخلايا الشمسية والإلكترونيات الشفافة. في هذه الرسالة ، بإستخدام نظرية الكثافة الوظيفية (DFT) قدمنا بدراسة نظرية للخواص الفزيائية لبعض المركبات من عائلة ABS_2. عن النتائج فقد قسمت الى قسمين:

القسم الأول تناولنا فيه كل من المركبات $KScS_2$ ، KYS_2 ، $KLaS_2$ ، $KLuS_2$ ، $RbLuS_2$ و $RbScS_2$. حيث وجدنا أن GGA-PBE تعطي نتائج أفضل من LDA في حساب الخصائص الهيكلية. في حين أن B3LYP تعطي تنبؤا ممتازا لفجوات الطاقة مقارنة بالقيم التجريبية و على هذا الأساس، تم اختيارها لحساب الخصائص البصرية. تظهر الخصائص البصرية أن هذه المركبات شفافة في كامل منطقة الأشعة تحت الحمراء والمنطقة المرئية. أخيرًا ، كنتيجة عامة من حساب الخصائص الديناميكية الحرارية هو أن هذه المواد أقل تأثرا بدرجات الحرارة الأقل من 100 كلفن في حين يظهر تاثرها جليا في درجات الحرارة الأكبر من 100 كلفن. اما في القسم الثاني فقد استعملنا تابعية الكثافة الصادرة والمطورة حديثا (SCAN meta-GGA) جنبًا إلى جنب مع تابعية الكثافة الهجينة HSE06 لدرسة كل من المركبات $CsScS_2$ ، $CsYS_2$ و $APmS_2$ (A= Li, Na, K, Rb, Cs) كمرشحين محتملين للمواد الموصلة الشفافة (TCMs) من النوع p. في الحقيقة هذه المركبات لم يتم تصنيعها مخبريا بعد. تؤكد نتائج حساب طاقة التكوين بالإضافة الى الفونونات أن هذه المواد مستقرة ديناميكيًا ويمكن تصنيعها تجريبيًا في البنية البلوريةα-$NaFeO_2$. تحتوي جميع المواد المدروسة على فجوة نطاق واسعة جدًا وهي شفافة في كل من منطقة الأشعة تحت الحمراء والمنطقة المرئية. الكتل الفعالة للثقوب للمواد المدروسة باستثناء LiPmS2صغيرة جدا تنافس تلك الموجودة في للمواد الموصلة الشفافة من النوع n المستخدمة قي الصناعة الحالية.

الكلمات المفتاحية : أشباه الموصلات، نظرية دالية الكثافة، اشباه الكمونات، الامواج المستوية، الخصائص البنيوية، الخصائص الالكترونية، الخصائص المرونية، الخصائص الضوئية

Abstract

Ternary alkali rare earth sulphides ABS_2, have been received much attention in recent years. Due to their wide band gap, they become a promising candidate for many applications ranging from portable electronics to light-emitting diodes (LED), solar cells and transparent electronics.

In this thesis, first principles calculations based on density functional theory (DFT), have been used to investigate structural, elastic, electronic, optical and thermodynamic properties of $KScS_2$, KYS_2, $KLaS_2$, $KLuS_2$, $RbLuS_2$, and $RbScS_2$. We found that GGA-PBE gives results better than LDA for structural properties. B3LYP functional leads an excellent agreement compared to the experimental ones. For this reason, it has been chosen to calculate the optical properties. The optical properties show that these compounds are transparent in the entire IR and visible regions. However, the thermodynamic properties of the considered materials are less affected by temperatures lower than 100 K. On the other hand, we have used the new developed SCAN meta-GGA functional together with accurate hybrid HSE06 functional, we have studied $CsScS_2$, $CsYS_2$, and $APmS_2$ (A= Li, Na, K, Rb, Cs) compounds as potential candidates for p-type transparent conducting materials (TCMs). These compounds have not been synthetized yet. The calculated results of the formation energy and phonon dispersion curves confirm that these materials are thermodynamically stable and feasible to synthesize experimentally with α-$NaFeO_2$ phase. All the considered materials have ultra-wide bandgap and they are transparent in the whole IR and visible regions. The

calculated hole effective masses are competitive with the industry standard n-type TCMs except for $LiPmS_2$ compounds.

Key words: Semiconductors, DFT, pseudo potentials, plane waves, electronic properties, structural properties, mechanical properties, optical properties.

Résumé

Les Sulfures de terres rares et d'alcalins ABS2 ont fait l'objet de beaucoup d'attention ces dernières années. En raison de leur large bande interdite, ils deviennent des candidats pour de nombreuses applications, l'électronique portable, les diodes électroluminescentes (LED), cellules solaires et l'électronique transparente.

Dans cette thèse, un calcul de premiers principes basés sur la théorie de la fonctionnelle de la densité (DFT) ont été utilisés pour étudier les propriétés structurales, élastiques, électroniques, optiques et thermodynamiques de $KScS_2$, KYS_2, $KLaS_2$, $KLuS_2$, $RbLuS_2$ et $RbScS_2$. Nous avons trouvé que GGA-PBE donne de meilleurs résultats que la LDA pour les propriétés structurales. Concernant la bande interdite, la fonctionnelle B3LYP donne un excellent accord par rapport à l'expérience. Pour cela, elle a été choisie pour calculer les propriétés optiques. Les propriétés optiques montrent que ces composés sont transparents dans les deux régions IR et visibles. Cependant, les propriétés thermodynamiques calculées révèlent que les matériaux considérés sont moins affectés par les températures inférieures à 100 K. D'autre part, nous avons appliqué la nouvelle fonctionnelle la plus développée SCAN avec la fonctionnelle hybrides HSE06, nous avons étudié $CsScS_2$, $CsYS_2$ et $APmS_2$ (A = Li, Na, K, Rb, Cs) comme candidats potentiels pour les matériaux transparents de type p (TCMs). Ces composés n'ont pas encore été synthétisés. Nos résultats de l'énergie de formation et de la dispersion des phonons confirment que ces matériaux sont thermodynamiquement stables et qu'il est possible de les synthétiser expérimentalement dans la phase α-$NaFeO_2$. Tous les matériaux considérés ont une bande interdite ultra-large et ils sont transparents dans toutes les régions IR et visibles. Les masses effectives des trous calculés sont compétitives dans l'industrie standard TCM de type n.

Mots clés : Les semiconducteurs, DFT, ondes planes, pseudo-potentiels, propriétés structurales, propriétés électroniques, propriétés mécaniques, propriétés optiques.

Acknowledgements

This phD thesis is realized in the Laboratoire Physique des Matériaux (LPM), University of Amar Telidji, Laghouat, Algeria. I would like to thank Professor **Ibn Khaldoun LEFKAIER**, head of the laboratory, and all the members.

Although a Ph.D. project is a one-man project, many contribute to its success, be it through support, advice or just making life enjoyable.

First of all, would like to express my profound gratitude to my supervisor professor **Mohamed HALIT** and Co-supervisor Professor **Salima SAIB** for their help, support, guidance, encouragement and given me freedom to explore a wide range of interesting problems throughout my thesis work.

I am incredibly grateful to Prof. **Rajeev AHAUJA** Professor at Department of Physics and Astronomy, Uppsala university-Sweden. who provided me opportunity to work in materials theory division as a visitor student, and helped me throughout my stay in Uppsala.

I would also like to thank the Dr. **Mohamed BOUCHENAFA** and Dr. **Said MAABED** for their advice, support, discussions and knowledge.

I would convey my overwhelming thanks to all the professors and administration of our department, they always manage an excellent working environment and ready to support.

I would like to thank Mr. **Bachir HELIFA** Maître de conferences "A" at University of Laghouat, to have accepted to chair the jury of this thesis.

I would also like to thank the thesis examiners Mr. **Miloud IBRIR** and Mr. **Nadjib BAADJI** Professors at University of M'sila, Mr. **Ahmed GUEDDOUH** et Mr. **Abdennour BENMAKHLOUF**, Maître de conferences "A" at University of Laghouat, for their participation in the jury.

To my friends and colleagues who making my journey as a Doctoral student at Laghouat University exhilarating one, who have helped in small ways, large ways, and all the ways in between. I owe you all. Thank you.

Contents

List of tables

List of Figures

List of Abbreviations, Variables and Constants

AE: All-electron

***B*:** Balk modulus

B3LYP: Becke, 3-parameter, Lee–Yang–Parr hybrid functional

C_{ij}: Elastic stiffness constants

CASTEP: Cambridge Serial Total Energy Package

CBM: Conduction band minimum

DOS: Density of states

DFT: Density functional theory

E: Energy

E_g**:** Band gap

E_F**:** Fermi energy

G: *S*hear modulus

GGA: Generalized gradient approximation **HF:** Hartee-Fock

GGA-PBE: GGA functional from Perdew, Burke and Ernzerhof's approximation

HF: Hartee-Fock

HSE: Heyd-Scuseria-Ernzerhof hybrid functional

HSE06: HSE functional, using 25% HF short range exchange potential

HH: Heavy-hole band

IR: infrared

LDA: Local density approximation

LED: Light emitting diode

LH: Light hole band

m_e^***:** Effective mass of electron

m_h^***:** Effective mass of hall

P: Pressure

PAW: Projector augmented wave

PDOS: Partial density of states

PP: Pseudopotential method

PW: Plane Wave

RE: Rare earth element

RF: Radio frequency

T: Temperature

TDOS: Total density of states

TCOs: Transparent conductor oxides

TCMs: Transparent conductor oxides

UV: Ultraviolet

UWBG: Ultra-wide bandgap semiconductors

VASP: Vienna ab-initio software package

VBM: Valence band maximum

WBG: Wide bandgap semiconductors

ZB: Brillouin zone

***z(S)*:** internal parameter

$\boldsymbol{\varepsilon(0)}$**:** Static dielectric constant

$\boldsymbol{\varepsilon_{kl}}$**:** Strain

$\boldsymbol{n(0)}$**:** Static value of refractive index

$\boldsymbol{\sigma_{ij}}$**:** Stress

Introduction

The multi-millennial history of human civilization shows that the significant increase in living and production levels is more often linked to the discovery of new materials with specific properties that are better and better adapted to real customer requirements that are becoming more sophisticated almost every day. This makes searching for new materials and their rapid optimization is critical field to enable future technological developments. Therefore, there will be no modern innovations without new materials, only existing bottlenecks. Historically, new materials have been discovered by either trial-and-error processes or serendipity. Where both are challenging experiments; require very time-consuming and high costs. With the numerous starting elements in the periodic table, there are almost unlimited potential combinations of multinary materials. In the past decade, with the development of computational tools, exploring new materials become possible systematically on a computer [1, 2]. Recently, the discovery progress has been developed and accelerated through a combination of High-throughput computing and large materials databases like AFLOWLIB[3], OQMD [4], CMR [5], and Materials Project [6]. Which based on first-principles calculations i.e. the density functional theory (DFT)[7-10].

Until recently, the determination of the crystal structure of materials and their properties was just linked to the experiment, where it has been considered as the only reliable source. However, since the advent the density functional theory (DFT), combined with modern computing power the situation became a quite different, where has allowed to anticipated the structures of many new materials, were later confirmed by experiments [8]. On the other hand, DFT gives a good understanding of not yet investigated properties of materials including structural, dynamical, magnetic, and electrochemical [11-14]. In other words, a given application requires a very one or many specific properties, which would be presented in only unique material. In addition, it became possible with high-throughput *ab initio* calculations to find the needed suitable properties of materials, and hence, we can decide whether it is a promising candidate for the considered applications without trial-experiments. This latter leads to saving time at lower costs [15-18].

Modern semiconductor technologies are only 70 years old, but they changed the world beyond anything that could have been imagined before them. The first spawn of semiconductors was in 1947, by the demonstration first transistor [19]. Until the late-1980s, semiconductors were limited to Ge, Si, and some “conventional” III-Vs, which all of them

have a small bandgaps lower than ≈ 2.3 eV. Recently, wide bandgap (WBG) and ultra-wide bandgap (UWBG) semiconductors, represent an exciting and challenging new area of research in materials sciences and applications. This kind of semiconductors has potential advantages over than narrower-bandgap in many relevant fields like; deep-UV optoelectronics high-power and RF electronics, as well as in transparent semiconducting, and quantum information, power switching and power amplifier applications as well [20-23]. Among the large group of UWGS semiconductor materials, the alkali rare earth sulfides ABS_2 (A= alkali metal and B = rare earth metal). Although these materials are known since 1964, studies dealing with them remained very rare. Recently, have been attracting more attention, since some of them are promising materials for solid state light emitting diode (LED), or X-ray phosphors, as they are potential candidates for many applications such as transparent materials, Na-ion batteries, nano-pigment, p-type transparent electrodes. Following our bibliographical research during this thesis, we found that, to date, there are no theoretical investigations on the most of these materials and some physical properties like; band structure, density of states, elastic properties, vibrational and linear optical are still unknown as well. Additionally, $CsScS_2$, $CsYS_2$, and $APmS_2$ (A= Li, Na, K, Rb, Cs) compounds are not-yet-synthetized.

The main objective of the research work carried out during this thesis is to investigate (**a**) the structural properties, elastic, electronic, chemical bonds and thermodynamic properties of $KScS_2$, KYS_2, $KLaS_2$, $KLuS_2$, $RbLuS_2$, and $RbScS_2$, compounds. (**b**) The crystal structure stability and physical properties of the ternary semiconductors $CsScS_2$, $CsYS_2$, and $APmS_2$ (A= Li, Na, K, Rb, Cs) as potential candidates for p-type transparent conductors by using pseudopotentials and plane waves based on the DFT as implemented in the CASTEP and VASP software. This thesis is organized as follows: in Chapter 1, we present the state of the art on ABS_2 family including structure types with their occurrence and relationship, and their different physical properties. We also give a brief presentation of some basic physical notions necessary can help to understand the obtained results. Chapter 2 is an introduction to the theoretical framework used in this thesis. Chapter 3 is a comparative investigation of structural, optoelectronic, mechanical, and thermodynamic properties of $KScS_2$, KYS_2, $KLaS_2$, $KLuS_2$, $RbLuS_2$, and $RbScS_2$ using LDA, GGA-PBE and hybrid B3LYP functional within CASTEP code. Then Chapter 4 is investigation of the structure and thermodynamic stability of $CsScS_2$, $CsYS_2$, and $APmS_2$ (A= Li, Na, K, Rb, Cs) compounds for p-type transparent conductors using GGA-PBE, SCAN and HSE06

functionals within VASP code. Finally, a brief conclusion is proposed including all the main results of this work.

References

[1] S. Atahan-Evrenk, A. Aspuru-Guzik, Prediction and calculation of crystal structures, Topics in Current Chemistry, 345 (2014).

[2] A.R. Oganov, C.J. Pickard, Q. Zhu, R.J. Needs, Structure prediction drives materials discovery, Nature Reviews Materials, 4 (2019) 331-348.

[3] S. Curtarolo, W. Setyawan, G.L. Hart, M. Jahnatek, R.V. Chepulskii, R.H. Taylor, S. Wang, J. Xue, K. Yang, O. Levy, AFLOW: an automatic framework for high-throughput materials discovery, Computational Materials Science, 58 (2012) 218-226.

[4] J.E. Saal, S. Kirklin, M. Aykol, B. Meredig, C. Wolverton, Materials design and discovery with high-throughput density functional theory: the open quantum materials database (OQMD), Jom, 65 (2013) 1501-1509.

[5] D.D. Landis, J.S. Hummelshoj, S. Nestorov, J. Greeley, M. Dulak, T. Bligaard, J.K. Norskov, K.W. Jacobsen, The computational materials repository, Computing in Science & Engineering, 14 (2012) 51-57.

[6] A. Jain, S.P. Ong, G. Hautier, W. Chen, W.D. Richards, S. Dacek, S. Cholia, D. Gunter, D. Skinner, G. Ceder, Commentary: The Materials Project: A materials genome approach to accelerating materials innovation, Apl Materials, 1 (2013) 011002.

[7] R. Jose, S. Ramakrishna, Materials 4.0: Materials big data enabled materials discovery, Applied Materials Today, 10 (2018) 127-132.

[8] F. Legrain, J. Carrete, A. van Roekeghem, G.K. Madsen, N. Mingo, Materials screening for the discovery of new half-heuslers: machine learning versus ab initio methods, The Journal of Physical Chemistry B, 122 (2018) 625-632.

[9] K. Gubaev, E.V. Podryabinkin, G.L. Hart, A.V. Shapeev, Accelerating high-throughput searches for new alloys with active learning of interatomic potentials, Computational Materials Science, 156 (2019) 148-156.

[10] A. Ludwig, Discovery of new materials using combinatorial synthesis and high-throughput characterization of thin-film materials libraries combined with computational methods, npj Computational Materials, 5 (2019) 70 D.

[11] S. Baroni, P. Giannozzi, A. Testa, Green's-function approach to linear response in solids, Physical Review Letters, 58 (1987) 1861.

[12] X. Gonze, Adiabatic density-functional perturbation theory, Physical Review A, 52 (1995) 1096 .

[13] C. Lee, D. Vanderbilt, K. Laasonen, R. Car, M. Parrinello, Ab initio studies on the structural and dynamical properties of ice, Physical review B, 47 (1993) 4863.

[14] D.-H. Seo, J. Lee, A. Urban, R. Malik, S. Kang, G. Ceder, The structural and chemical origin of the oxygen redox activity in layered and cation-disordered Li-excess cathode materials, Nature chemistry, 8 (2016) 692.

[15] M.S. Islam, C.A. Fisher, Lithium and sodium battery cathode materials: computational insights into voltage, diffusion and nanostructural properties, Chemical Society Reviews, 43 (2014) 185-204 .
[16] G. Sai Gautam, T.P. Senftle, N. Alidoust, E.A. Carter, Novel solar cell materials: insights from first-principles, The Journal of Physical Chemistry C, 122 (2018) 27107-27126.
[17] S.V. Alapati, J.K. Johnson, D.S. Sholl, Using first principles calculations to identify new destabilized metal hydride reactions for reversible hydrogen storage, Physical Chemistry Chemical Physics, 9 (2007) 1438-1452.
[18] X. Blase, C. Attaccalite, V. Olevano, First-principles GW calculations for fullerenes, porphyrins, phtalocyanine, and other molecules of interest for organic photovoltaic applications, Physical review B, 83 (2011) 115103.
[19] M. Riordan, L. Hoddeson, C. Herring, The invention of the transistor, More Things in Heaven and Earth, (1999) 563-578.
[20] J. Tsao, S. Chowdhury, M. Hollis, D. Jena, N. Johnson, K. Jones, R. Kaplar, S. Rajan, C. Van de Walle, E. Bellotti, Ultrawide-Bandgap Semiconductors: Research Opportunities and Challenges, Advanced Electronic Materials, 4 (2018) 1600501.
[21] C. Xie, X.T. Lu, X.W. Tong, Z.X. Zhang, F.X. Liang, L. Liang, L.B. Luo, Y.C. Wu, Recent progress in solar-blind deep-ultraviolet photodetectors based on inorganic ultrawide bandgap semiconductors, Advanced Functional Materials, 29 (2019) 1806006 .
[22] D. Laks, C. Van de Walle, G. Neumark, S. Pantelides, Role of native defects in wide-band-gap semiconductors, Physical Review Letters, 66 (1991) 648.
[23] K.A. Mengle, S. Chae, E. Kioupakis, Quasiparticle band structure and optical properties of rutile GeO2, an ultra-wide-band-gap semiconductor, Journal of Applied Physics, 126 (2019) 085703 .

CHAPTER I

Bibliographic study And Presentation of ABS_2 materials

I.1 Introduction

The ternary compounds with conventional chemical formula $A^{I}B^{III}C_2^{VI}$ have received a much attention in the recent years, since they are promising candidates for many applications such as light-emitting diodes[1], solar-cells [2], luminescence [3], vacuum-ultraviolet-transparent lenses used in optical lithography steppers[4], and nonlinear optical devices[5]. Among this large group of semiconducting material, the alkali rare earth sulfides ABS_2 (A= alkali metal and B = rare earth metal), inherent unique combination of exciting optical, magnetic and mechanical properties. Many of them are having higher melting points, promising candidates for infrared windows materials, p-type transparent electrodes, Na-ion batteries, white LED solid state lightings, X-ray phosphors, and some of these compounds show excellent semi conductive behaviors [6-17].

In this chapter and based on the available scientific works, we will present the ABS_2 (A= alkali metal and B = rare earth metal) semiconductors: their structural, electronic and optical properties. We will present first the different structure types of ABS_2 with their occurrence and relationship passing through a description of α-NaFeO2 type structure with a mention of the effect of the atomic number *Z* on the structural properties as well as the Synthesis method of ABS_2. We will give an overview of some bibliographic bases necessary to understand this study.

I.2 State-of-the-art of alkali rare earth sulphides ABS_2

Historically, the first synthesis of the ternary semiconductors ABS_2 (A = Li, Na and K) was in 1964 by Ballestracci and Bertaut[18, 19]. They synthesized and studied the structural properties of these compounds. Bronger[20] in 1973 has expanded this family by studying the structural properties $RbBS_2$ and $CsBS_2$ (B= rare earth elements) materials. These studies were followed by many researches [6, 8, 10, 21-29], all results of these works are summarized in the annexe (***Table S1***). Most of these researches have focused on the structural properties of such systems. Moreover, studies dealing with the other physical properties remained very rare.

In 2011, these materials family start to be studied in a pioneer work dealing with fundamental properties of pure and RE-doped (RE = Ce, Eu, Pr, Sm, Tb) $RbLaS_2$. where has been proposed as a novel material for solid state white light emitting diode (LED) lighting and X-ray phosphors[16]. Therefore, the ternary ABS_2 (B= rare earth elements) become a very interesting subject for many works, especially in the luminescence field [17, 30-39]. It is worth to mention that all the above-mentioned works are purely experimental. Recently, many theoretical studies on the title materials have been done using density functional theory (DFT) for different applications [14, 15, 40-44].

I.3 Structural types present in ABS_2, their occurrence and relationship

The information reported in the literature about the known structures of Alkali rare earth sulphides ABS_2 summarized in the annexe (**table S1)** are presented graphically in ***Figure I.1***. As can be seen from ***Figure I.1***, Among all possible ABS_2 stoichiometry (A=Li, Na, K, Rb or Cs; B= La–Lu, Y or Sc), four different crystalline structures have been reported (cubic Th_3P_4 with space group I-43d, cubic NaCl with Fm-3m space group, rhombohedral α-$NaFeO_2$ with space group R-3m and hexagonal β-$RbScO_2$ with space group P63/mmc). Most compounds belong to the α-$NaFeO_2$ structure-type and little less to the NaCl-type. Where α- $NaFeO_2$-type structure can be derived from the NaCl-type (***Figure I.2***). Both KBS_2 and $RbBS_2$ (B= rare earth elements) adopt only the rhombohedral α-$NaFeO_2$-type structure.

As matter of fact, the structure-type of these related compounds is significantly affected by the radius ratio $R_{B^{3+}}/R_{A^{+}}$ of the constituting cations. For room temperature $LiBS_2$ and $NaBS_2$ materials for larger values ($0.95 < R_{B^{3+}}/R_{A^{+}} < 1.08$) crystallized with NaCl-type structure, with increasing the difference of the radius between the monovalent A^+ and trivalent cations B^{3+} ($0.62 < R_{B^{3+}}/R_{A^{+}} < 0.95$), the compound tends to crystallize with α-

$NaFeO_2$-type [20, 21]. Additionally, the temperature is an important factor where the first-order phase transition from NaCl phase to α-$NaFeO_2$ structure type takes place for $LiYS_2$ (896 K) and $LiErS_2$ (966 K), for $NaNdS_2$, the temperature phase transition observed at 1160 K [25].

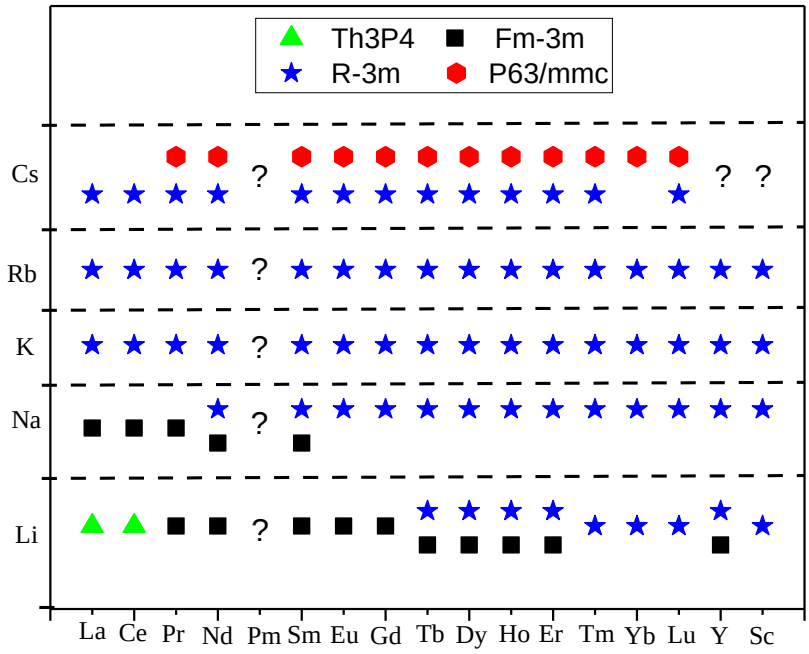

***Figure I.1**: Schematic representation of the deferent structure types in ABS_2 compounds*

I.4 Structural properties

I.4.1 Description of α-$NaFeO_2$ type structure for ABS_2 materials family

The layered rhombohedral α-NaFeO2-type structure that is described by R-3m (166) space group. Generally, this structure type can be derived from a cubic NaCl-type, where both cations A^+ and B^{+3} (which are randomly disordered with NaCl structure) are alternatively ordered in layers S^{2-}–A^+– S^{2-}– B^{+3}– S^{2-} perpendicular to the cubic [111] direction, as shown in **figure I.2**. Here, the difference between the ionic radii of these cations induces the appearance of this order and the rhombohedral distortion.

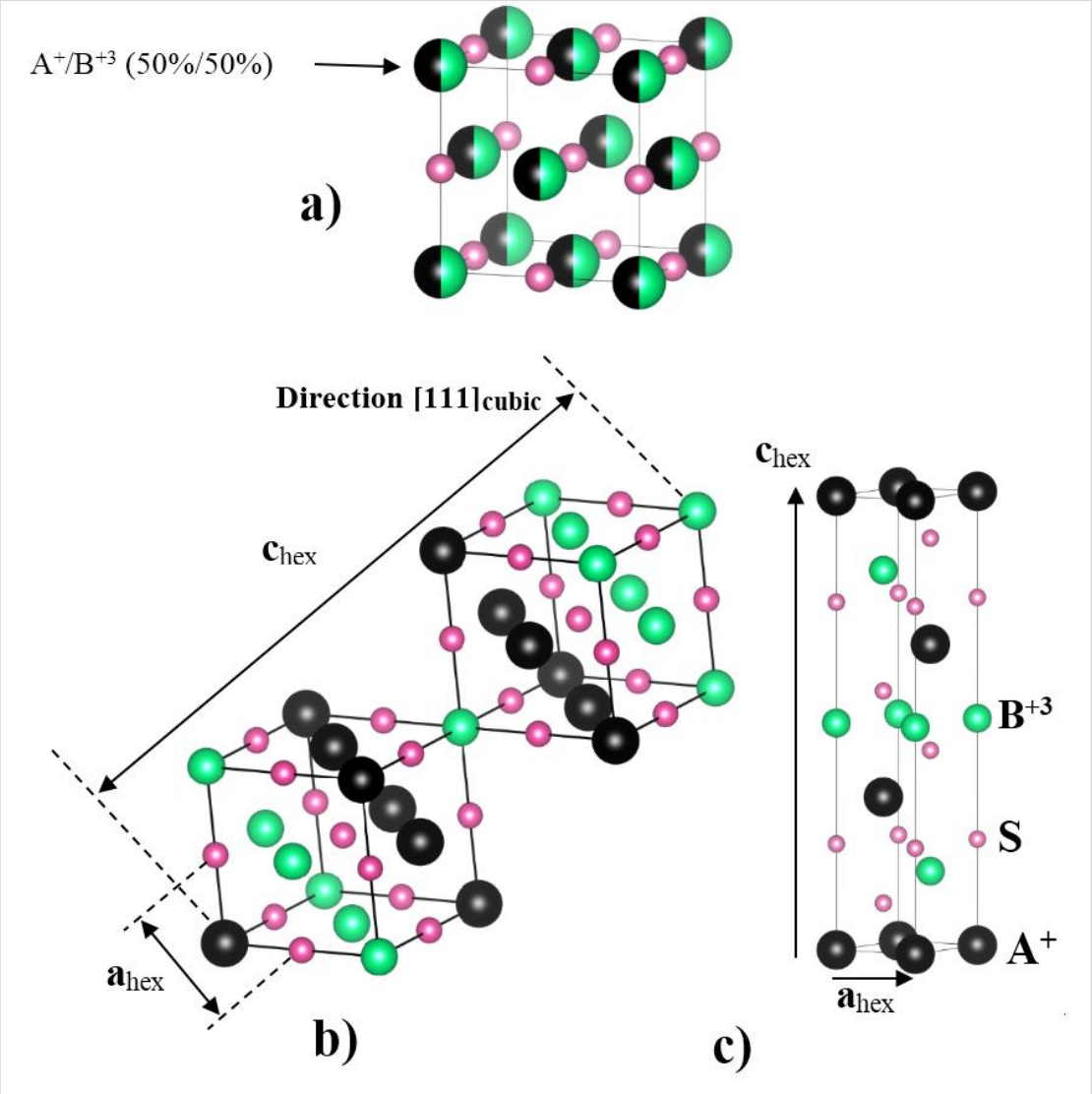

***Figure I.2**: Schematic representation of ABS_2 materials in the -$NaFeO_2$ structure (R-3m space group) **(c)**, derived from the NaCl structure **(a, b)**.*

In addition, this structure type can be described as infinite stacked layers of AS_6–RES_6–AS_6–RES_6.... edge-sharing octahedra along the c-axis. Both AS_6 and BS_6 octahedra characterized by identical bonds length A–S in AS_6 and B–S in BS_6, two unequal distances (S1–S2 and S2–S3 in AS_6 octahedral and S1–S2 and S4–S5 in BS_6 octahedral), two unequal angles (S1–A–S2 and S2–A–S3 in AS_6 octahedral and S3–B–S4 and S4–B–S5 in BS_6 octahedral), all these angles defer from 90 at ambient conditions; thickness *h* parallel to the axe c of the hexagonal unit cell where c_{hex}= 3*h*(AS_6) + 3*h*(BS_6) (***Figure I.3***).

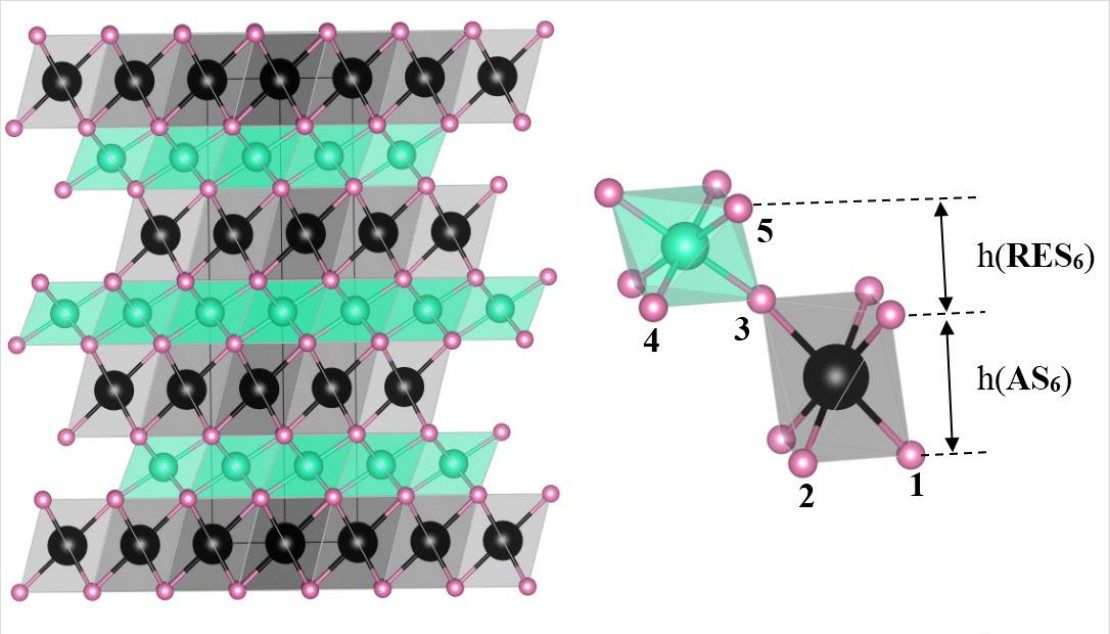

Figure I.3 *Schematic representation of the ABS_2 in α-$NaFeO_2$ structure showing the layered character of this type of material.*

However, In this structure the alkali atoms occupy the 3a Wyckoff position (0,0,0), the rare earth located at the 3b position (0,0,1/2), and sulfur atoms situated at 6c position (0,0,*z*), where *z* is the fractional coordinate. In fact, here the hexagonal unit cell is a conventional unit cell including three formula units, and one formula is the rhombohedral unit cell.

I.4.2 Structural parameters and atomic number *Z* relationship in α-$NaFeO_2$-type

From the available data in the literature about ABS_2 materials, it turned out that there is a relationship between the atomic number *Z* and the structural parameters including; unit-cell parameters *a* and *c*, fractional coordinate $z(S^{2-})$, the interatomic distance, and thickness of cationic layers $h(AS_6)$ and $h(BS_6)$. Which, allow confirming the reliability of the structural parameters of any of these compounds. For example, ***Figure I.4*** **(a, d)** indicate that there is some deviation in the determination of unit-cell parameters of $LiTbS_2$. Furthermore, ***Figure I.4*** **(d)** shows that the crystal structure of Y^{3+} compounds corresponds to those of Ho^{3+}, this is due to the very close crystal ionic radii of six-coordinated, Y^{3+} (1.040 Å) and Ho^{3+}(1.041 Å)[45].

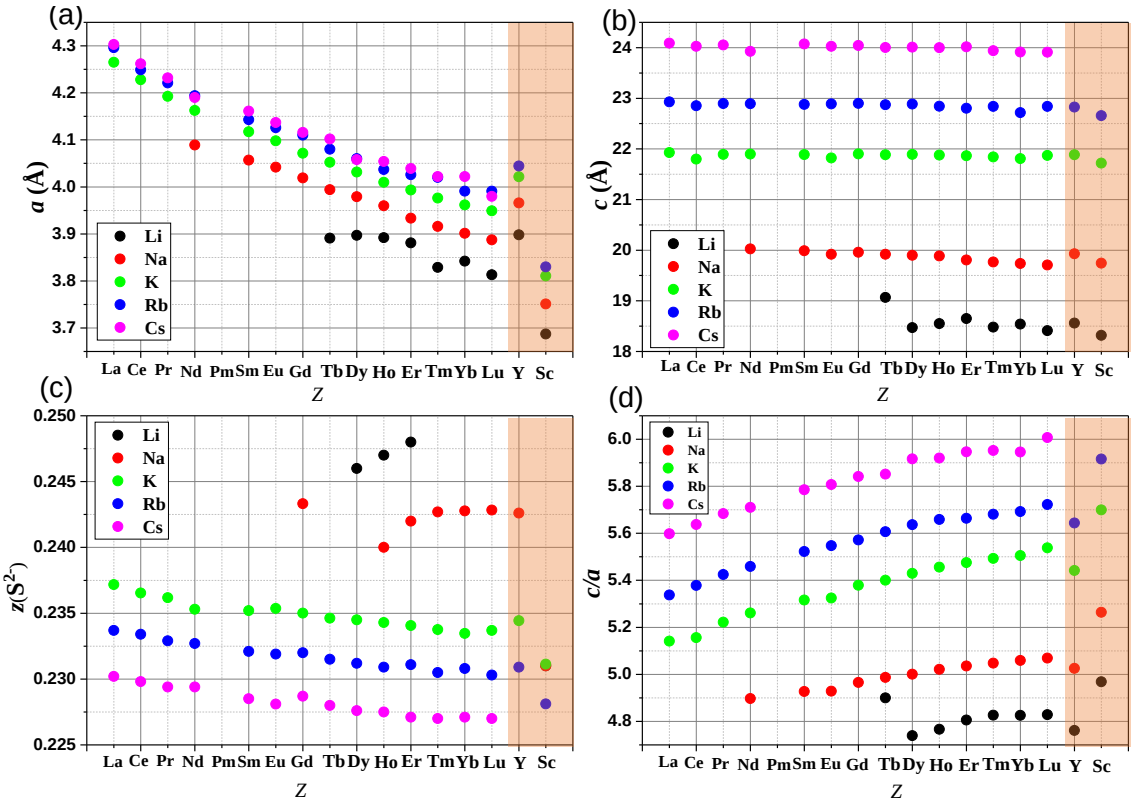

Figure I.4. *The dependence of the lattice parameters* ***(a)*** *a,* ***(b)*** *c,* ***(c)*** *fractional coordinate z(S^{2-}), and* ***(d)*** *the unit-cell ratio c/a on atomic number Z in ABS_2 materials (α-$NaFeO_2$ structural type)*

I.4.2.1 Effect of atomic number *Z* on the unit-cell parameter *a, c* and the fractional coordinate *z*(S^{2-})

As can be seen from ***Figure I.4*** **(a)**, The lattice parameter *a* decreases almost linearly with increasing atomic number *Z* of the trivalent cation B^{3+}(La-Lu). This figure also shows that the parameter *a* increases with increasing atomic number *Z* of the alkaline earth metals from Li^+ to Cs^+.

The first observation that can be clearly seen from the ***Figure I.4*** **(b)** is that the value of the parameter *c* remains rather constant with the change of atomic number *Z* of the rare earth elements B^{3+}(La-Lu). One can well notice that the value of the unit-cell parameter *c* increases with the increase of atomic number *Z* of the monovalent A^+ (Li-Cs).

As ***Figure I.4*** **(c)** shows, for the compounds KBS_2, $RbBS_2$, and $CsBS_2$, a fairly linear decrease of the fractional coordinate *z*(S^{2-}) is observed with increasing the number atomic *Z* of B^{3+}. This not observed for $LiBS_2$ and $NaBS_2$ materials. However, we can also note that there is a direct correlation between the *z*(S^{2-}) and the atomic number *Z* of alkalis, where *z*(S^{2-}) is decreased from Li to Cs.

I.4.2.2 Effect of atomic number *Z* on the interatomic distance and the layers width

As we can see from ***Figure I.5*** **(a)**, with the increase the atomic number *Z* from La to Lu a very small decrease (quasi-linear) is observed for the A^{+}–S^{2-} bonds, while these bonds increase with increase the atomic number *Z* from Li to Cs. On the other hand, the interatomic distances B^{3+}–S^{2-} decrease when going up from La to Lu with the exception of $LiBS_2$ and $NaBS_2$ materials. Furthermore, the bonds B^{3+}–S^{2-} almost unaffected by the change of monovalent cation size (Li-Cs) ***Figure I.5*** **(b)**.

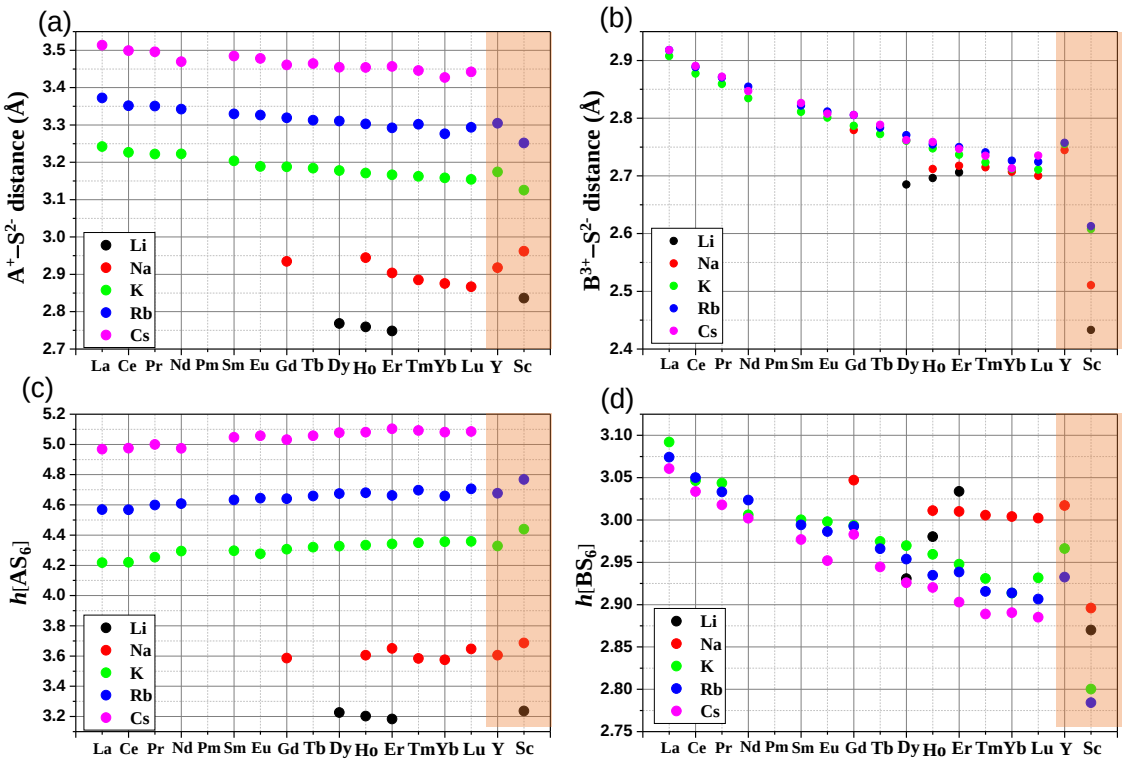

Figure I.5. *The dependence of the interatomic distances* ***(a)*** *A^{+}–S^{2-},* ***(b)*** *B^{3+}–S^{2-}, and layers width* ***(c)*** *$h(AS_6)$,* ***(d)*** *$h(BS_6)$ on atomic number Z in ABS_2 materials (α-$NaFeO_2$ structural type).*

similar to the interatomic distances, almost there is no effect of trivalent cations B^{3+} on the monovalent layers' width $h(AS_6)$ while becoming more thicker going from Li^{+} to Cs^{+} ***Figure I.5 (a)***. However, the trivalent layers width $h(BS_6)$ decrease with increase the atomic number *Z* (La-Lu) for K, Rb, and Cs materials. While a small decrease is observed with increase the atomic number Z of the alkaline earth metals from Li^{+} to Cs^{+} ***Figure I.5(d)***.

I.5 Synthesis of ABS_2

Several synthesis methods have been reported in the literature throughout the years from the first preparation in 1964. High temperature up to 900°C solid-state reactions under flowing H_2S starting with A_2CO_3 and B_20_3 [18, 19], or ACI and BCI_3 [10], directly from the elements in evacuated silica ampules [25]. By anion-exchange reaction [26]. currently, the most used method reported is the chemical reaction in an electric resistance furnace under the flow of hydrogen sulfide ***Figure I.6*** [16].

As example preparation of $RbLaS_2$ using the chemical reaction in an electric resistance furnace under the flow of hydrogen sulfide:

As starting materials, we need Rb_2CO_3, La_2O_3, Hydrogen sulfide gas (H_2S) and Nitrogen gas (N_2). Firstly, Rb_2CO_3 and LaO_3 materials are mixed in the molar ratio 1:80 (Rb_2CO_3 abundance). The prepared mixture is placed in a corundum boat and put into a corundum tube (inner volume of 0.9 dm^3), then heating it up to 1025 ºC using an electric resistance furnace with a heating rate of 5 ºC min^{-1} under the flow of argon gas. When the mixture reached the desired temperature, the reaction mixture was annealed for 1 h under the flow (15 dm^3 h^{-1}) of hydrogen sulfide. After annealing, the reaction system cooling under the flow of Ar (1 ºC min^{-1}, 0.3 dm^3 h^{-1}). Note that even after annealing, H2S mixed with Ar is still present in the reaction volume. Upon reaching room temperature (RT), the corundum boat is removed from the tube furnace and the reaction products are treated by a decantation process (three times by distilled water and once by ethyl alcohol), followed by drying under the Argon flow. The resulting product consisted of hexagonal platelets sized 1–2 mm. Photographs of RbLaS2 is presented in ***Figure I.7.***

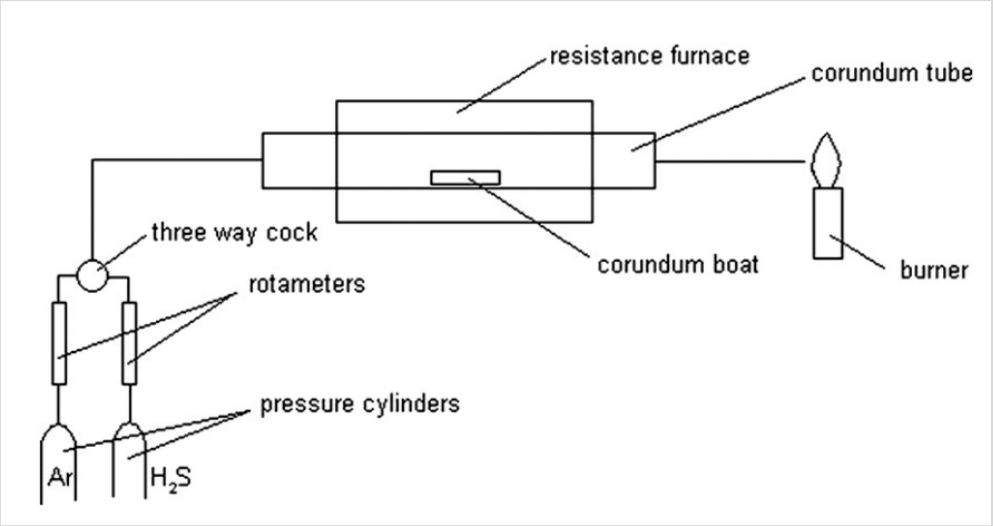

Figure I.6. *A scheme for the preparation of ABS_2 compounds[16].*

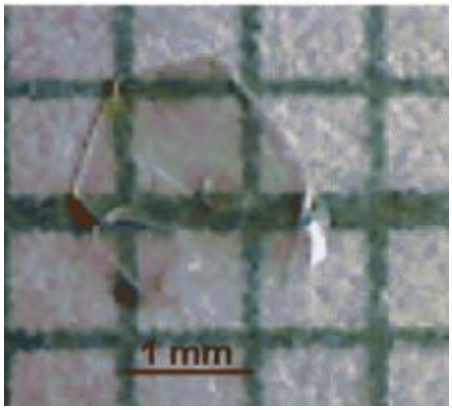

Figure I.7 *Photographs of $RbLaS_2$ compound[16].*

I.6 Electronic Properties

I.6.1 Concept of Band Structure

In an isolated atom, the electrons in each orbit possess definite energy. However, in the case of solids, when the atoms are closely arranged together, the electrons especially that in outermost orbit experiences an attractive force from the other atoms.

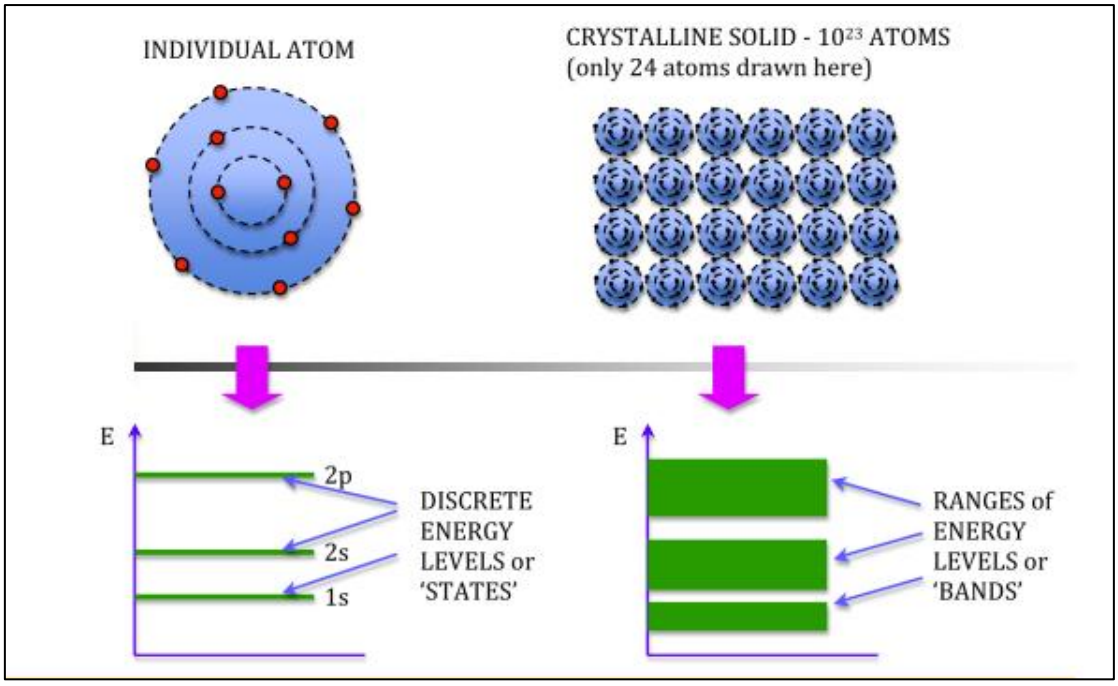

Figure I.8*. Basic concept of electronic band structure.*

Suppose two isolated atoms are brought close to each other, the electrons in the orbits of two atoms interact. Hence, the energies of valence electrons will slightly change to a lower and higher level than the original value. The same principles apply in a solid with N atoms **(*Figure I.8*)**. All of the same energy are taken and combined to form N number of closely energy levels. It is known as energy bands. These bands are separated by empty energy regions, called the forbidden band of energies. The band located above the band gap is called the conduction band (BC), unlike the band below band gap called the valence band (BV). In consequence, material can be classified based on its band gap value into three categories **(*Figure I.9*)**: - **Conductor** (metal) - **Insulator** – **Semiconductor.**

a) **Conductor**

For conductor, as results in the overlapping between the valence band (BV) and conduction band (BC), there is no energy gap between both bands. Moreover, a large number of free electrons exist at room temperature. *As example:* silver, copper, iron, gold, aluminium ...etc.

b) **Insulator**

An insulator has a high band gap up to 7 eV, which make the electrons transition from the valence band to the conduction band impossible. There is no free electrons and the material cannot conduct the electricity at all. *Example:* wood, paper, plastic …etc.

c) Semiconductor

For semiconductor, the conduction band is empty and the energy gap between the maximum valence band to the minimum conduction band is very small. Therefore, it is an insulator at 0K, while become a conductor under certain but not others, making it a good medium for electrical current control. *Example:* Silicon, Germanium …etc.

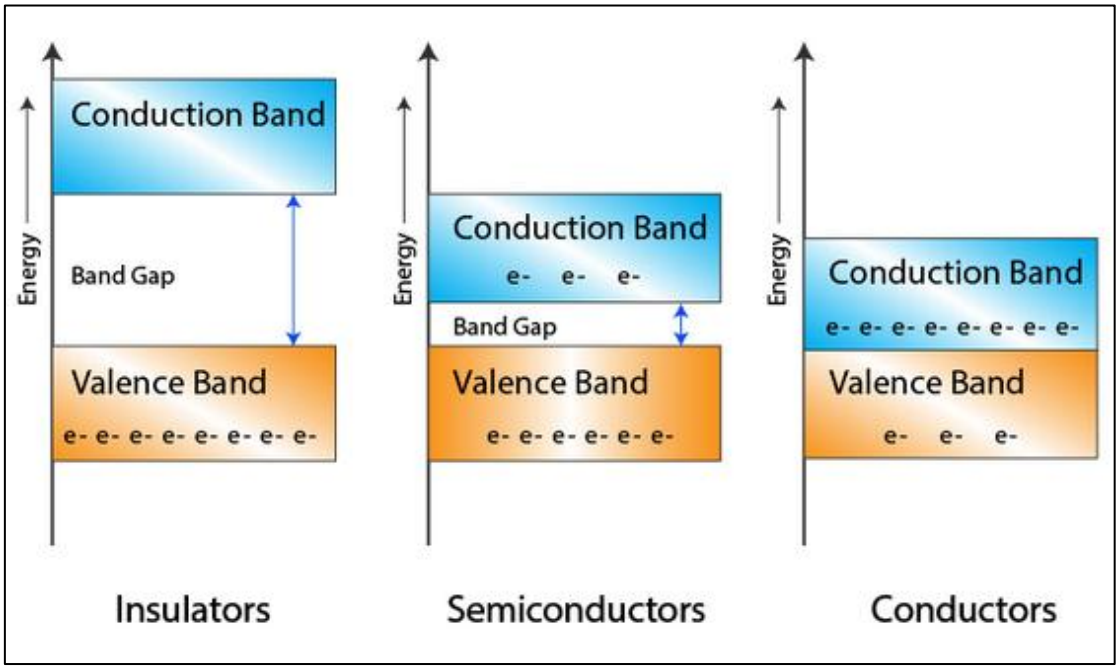

Figure I.9*. Classification of materials based on band energy theory.*

In **table I.1** we summarize the electronic band gap of some ABS_2 materials, which have been reported in the literature. Based on the data in **table I.1,** these ternary sulphides can be classified as indirect semiconductor with large band gap, where most values between (3.80 and 4.08 eV). Which make these materials very interesting for the ultrawide-bandgap semiconducting field.

Table I.1: the available electronic band gap of ABS_2 materials.

Compound	$Eg_{(ind)}$	method	Ref	Compound	Eg	method	Ref
$LiScS_2$	3.75	HSE	[15]	**$NaGdS_2$**	3.76	Exp	[37]
$NaScS_2$	1.81	PBE	[14]	**$NaLuS_2$**	4.08		
$NaEuS_2$	2.29 3.88 3.19	PBE PBE0 HSE	[41]	**$NaYS_2$**	4.01		
				$KLaS_2$	3.82		
				$KGdS_2$	3.76		
$KEuS_2$	2.48 4.10 3.41	PBE PBE0 HSE06		**$KLuS_2$**	4.03		
				KYS_2	4.01		
				$RbLaS_2$	3.84		
$RbEuS_2$	2.55 4.16 3.49	PBE PBE0 HSE		**$RbGdS_2$**	3.86		
				$RbLuS_2$	4.00		
				$RbYS_2$	4.04		
$CsEuS_2$	2.60 4.21 3.54	PBE PBE0 HSE06		**$RbTbS_2$**	2.1	Exp	[46]
KYS_2	3.37	HSE	[40]				
$KScS_2$	2.89						
$RbScS_2$	2.88						

I.6.2 Concept of effective mass

In semiconductor materials, due to the potential created by the other particles in the crystal, electrons unable to move as freely and will have different behaviour from the free electrons. The electron seems like it has a new mass that usually referred to as the **effective mass** ($\boldsymbol{m}^*$). The effective mass of the carriers may be larger or smaller than the free electron mass m_e (9.11×10^{-31} kg).

The most common calculation method of the effective mass of a semiconductor is by fitting the actual E-k diagram around the conduction band minimum for electrons ($\boldsymbol{m}_e^*$) or the valence band maximum for the holes ($\boldsymbol{m}_h^*$) by a parabola. The effective mass equation:

$$\left[\frac{1}{m^*}\right] = \frac{1}{\hbar^2}\frac{\partial^2 E(k)}{\partial k^2} \qquad (I.1)$$

✓ Small effective masses mean high mobility, and hence high conductivity.

I.7 Optical properties

In nature, light interacts with matter in many different ways. Metals are shiny, but water is transparent. Stained glass and gemstones convey certain colours, but absorb others. However, some materials such as milk appear white because they disperse the incoming light in all directions.

The wide-ranging optical properties observed in the interaction light-solid can be classified into three general phenomena, namely reflection, absorption and transmission, as illustrated in ***Figure I.10***.

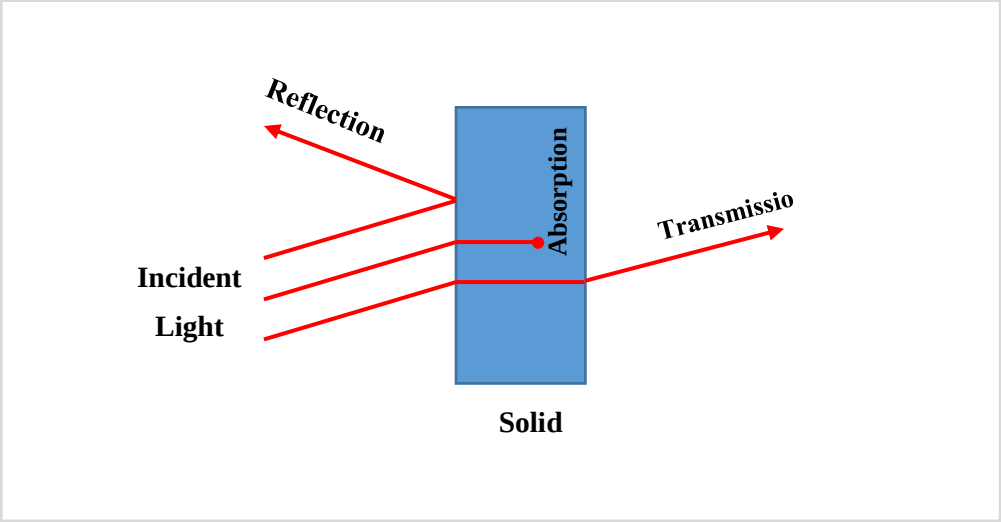

Figure I.10. *Interaction between light and matter.*

At the microscopic or quantum mechanical level the optical properties are closely connected with the band structure. The linear response of a material to the electromagnetic wave can be described by the dielectric function $\varepsilon(\omega) = \varepsilon_1(\omega) + i\varepsilon_2(\omega)$. The imaginary part $\varepsilon_2(\omega)$ of the dielectric function represents the absorption of the radiation induced by the electronic transition between the occupied and unoccupied states. The imaginary part $\varepsilon_2(\omega)$ can be calculated from the electronic structure. Where the real part $\varepsilon_1(\omega)$ can be derived from the imaginary part $\varepsilon_2(\omega)$ using Kramers-Kronig approach[47].

$$\varepsilon_2(\omega) = \frac{2\pi e^2}{m_e^2 \omega^2 \varepsilon_0} \sum_{C,V} \int_{BZ} |\langle \Psi_k^c | \vec{u}.\vec{r} | \Psi_k^v \rangle|^2 \delta(E_k^c - E_k^v - \hbar\omega) dk^3 \qquad \text{(I. 2)}$$

$$\varepsilon_1(\omega) = 1 + \frac{2}{\pi} P \int_0^{\infty} \frac{\acute{\omega}\varepsilon_2(\acute{\omega})}{\acute{\omega}^2 - \omega^2} d\acute{\omega} \quad \text{(I. 3)}$$

Where, P is the principal value of the integral.

It is easy to deduce the other optical properties, such as the refractive index n(ω), and the extinction coefficient k(ω), the absorption coefficient α(ω) and the optical reflectivity spectra R(ω), after our knowledge of the real $\varepsilon_1(\omega)$ and imaginary $\varepsilon_2(\omega)$ parts of the dielectric function $\varepsilon(\omega)$ by using the following equations:

$$n(\omega) = \frac{1}{\sqrt{2}} \left[\sqrt{\varepsilon_1^2(\omega) + \varepsilon_2^2(\omega)} + \varepsilon_1(\omega) \right]^{1/2} \quad \text{(I. 4)}$$

$$K(\omega) = \frac{1}{\sqrt{2}} \left[\sqrt{\varepsilon_1^2(\omega) + \varepsilon_2^2(\omega)} - \varepsilon_1(\omega) \right]^{1/2} \quad \text{(I. 5)}$$

$$R(\omega) = \left| \frac{\varepsilon(\omega)^{1/2} - 1}{\varepsilon(\omega)^{1/2} + 1} \right|^2 \quad \text{(I. 6)}$$

$$\alpha(\omega) = \sqrt{2}\omega \left[\sqrt{\varepsilon_1^2(\omega) + \varepsilon_2^2(\omega)} - \varepsilon_1(\omega) \right]^{1/2} \quad \text{(I. 7)}$$

I.7.1 Direct interband transition

Direct interband transition is the electronic transition from the valence band to the conduction band or vice versa at the same electron's $\vec{k}$-vector. Where the emitted or absorbed energy defined as:

$$\hbar\omega = E_f - E_i \quad \text{(I. 8)}$$

E_f and E_i represent the energies of the final and initial electron states.

I.7.2 Indirect interband transition

Indirect interband transition is the electronic transition from the valence band to the conduction band or vice versa, with different values of K between the initial and the final states. Other words, semiconductor will absorb or emit a phonon of energy $\hbar\omega_{phon}$ in this process:

$$\hbar\omega = E_f - E_i \pm \hbar\omega_{phon} \quad \text{(I. 9)}$$

Where: (+ sign) for emission and (− sign) absorption.

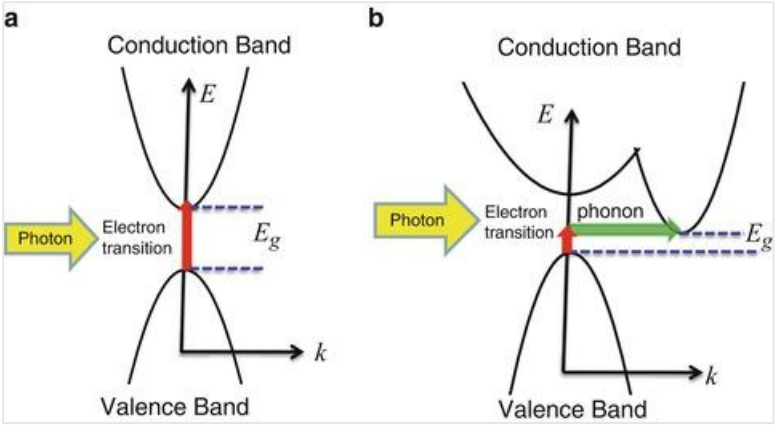

Figure I.11. *Direct and indirect interband transition*

Back to ABS_2 materials, *Ahmed et al* [48] have calculated the dielectric function of pure $KNdS_2$, $KHoS_2$, $KErS_2$ and $KLuS_2$. *Azzouz et al* [41] have calculated the optical properties such as dielectric function and the optical reflectivity spectra $R(\omega)$ for each $NaEuS_2$, $KEuS_2$, $RbEuS_2$ and $CsEuS_2$. As results of both studies, the optical properties of the studied compounds are anisotropic. Their static dielectric constants vary between 3.88 and 5.7. For each compound, the static dielectric constants along with *xx* direction are greater than along *zz* direction. The reflectivity in the infrared and visible of $AEuS_2$ (A = Na, K, Rb, Cs) is very small between 7 and 13%. While it is very high in the ultraviolet region.

I.8 Elastic and mechanical properties

I.8.1 Elastic constants and mechanical stability

Understanding the elastic properties of materials is very important for their application and advancement. Elastic stiffness constants C_{ij} are critical for assessing how a solid responds under applied stress or, conversely, the stress required to maintain a given deformation within the elastic limit. Elastic constants enable calculations of other parameters related to mechanical properties such as bulk modulus *B* and shear modulus *G*. which can give important information about the physical properties of materials like material ductility, strength, mechanical stability, etc.

Generally, there are two methods used to calculate the elastic constants (i) Stress-vs-strain and (ii) Energy-vs-stain method. In this Thesis, the Stress-vs-strain method has been used [49]. In this later, both stress σ_{ij} and strain ε_{kl} have six components in total, three tensile and three shear components. When a material is subjected to stress within its elastic limit, the proportionate amount of produced strain linearly proportional with the applied stress i.e. the ratio between the applied stress and the corresponding strain is constant (**stress/strain = constant)**. This known as ***Hooke's law***:

$$\sigma_{ij} = \sum_{k,l} C_{ijkl}\varepsilon_{kl} \qquad (\text{I. } 10)$$

Where the indices i, j, k et l take the values 1, 2 and 3. Hence, the elastic properties of material described by a fourth rank of elasticity tensor $3^4 = 81$ elements.

From The symmetry of the Cauchy stress tensor and the symmetry of the infinitesimal strain tensor, we find that $C_{ijkl} = C_{jikl}\ and\ C_{ijkl} = C_{ijlk}$. These two symmetries together called the minor symmetries of the stiffness tensor, which reduces the number of elastic constants from 81 to 36, can be arranged in a 6×6 matrix. Other symmetries called the major symmetries of the stiffness tensor $C_{ijkl} = C_{klij}$, this reduces the elastic contestants from 36 to 21 independent components. According to Voigt notation, the Hooke's law can be expressed in matrix notation as:

$$\sigma = \begin{pmatrix}\sigma_1\\ \sigma_2\\ \sigma_3\\ \sigma_4\\ \sigma_5\\ \sigma_6\end{pmatrix} = \begin{pmatrix}C_{11} & C_{12} & C_{13} & C_{14} & C_{15} & C_{16}\\ C_{21} & C_{22} & C_{23} & C_{24} & C_{25} & C_{26}\\ C_{31} & C_{32} & C_{33} & C_{34} & C_{35} & C_{36}\\ C_{41} & C_{42} & C_{43} & C_{44} & C_{45} & C_{46}\\ C_{51} & C_{52} & C_{53} & C_{54} & C_{55} & C_{56}\\ C_{61} & C_{62} & C_{63} & C_{64} & C_{65} & C_{66}\end{pmatrix}\begin{pmatrix}\varepsilon_1\\ \varepsilon_2\\ \varepsilon_3\\ \varepsilon_4\\ \varepsilon_5\\ \varepsilon_6\end{pmatrix} \qquad (\text{I. } 11)$$

Any symmetry present in the structure can make some of these components equal and others zero. Therefore, every structure system has its own elastic constants. For the ternary rare-earth sulphides ABS_2 with α-$NaFeO_2$ structure-type (R-3m space group), the elastic properties are described by six independent elastic constants namely: (C_{11}, C_{12}, C_{13}, C_{14}, C_{33}, and C_{44}), since C_{66} = 1/2(C_{11}–C_{12}). After Born et al, material is mechanically stable in any structure, its elastic constants should verify the mechanical stability criteria. In our case, the mechanical stability criteria of α-$NaFeO_2$ structure defined as [50]:

$$C_{11} > |C_{12}|;\ C_{44} > 0, C_{13}^2 < \frac{1}{2}C_{33}(C_{11} + C_{12}), C_{14}^2 < \frac{1}{2}C_{44}(C_{11} - C_{12}) \qquad (\text{I. } 12)$$

I.8.2 Elastic constants and mechanical Proprieties

Generally, knowledge of the elastic constants C_{ij}, allow us to calculate the macroscopic elastic parameters, for instance, the bulk modulus *B*, the shear modulus *G*. The bulk modulus *B*, and shear *G*, can be determined by applying the Voigt-Reuss-Hill relations (VRH)[51-53]:

$$B_H = \frac{1}{2}\,(B_R + B_V) \tag{I.13}$$

$$G_H = \frac{1}{2}\,(G_R + G_V) \tag{I.14}$$

$$B_V = \left(\frac{1}{9}\right)[2(C_{11} + C_{12}) + C_{33} + 4C_{13}] \tag{I.15}$$

$$B_R = \frac{\left((C_{11} + C_{12})C_{33} - 2C_{12}^2\right)}{(C_{11} + C_{12} + 2C_{33} - 4C_{13})} \tag{I.16}$$

$$G_R = \frac{5}{2}\left\{\frac{[(C_{11} + C_{12})C_{33} - 2C_{13}^2]C_{44}C_{66}}{3B_V C_{44}C_{66} + \left((C_{11} + C_{12})C_{33} - 2C_{12}^2\right)(C_{44} + C_{66})}\right\} \tag{I.17}$$

$$G_V = \left(\frac{1}{30}\right)(7C_{11} - 5C_{12} + 12C_{44} + 2C_{33} + 4C_{13}) \tag{I.18}$$

Where *V*, *R* and *H* index represent respectively, **Voigt**, **Reuss** and **Hill**.

. The Young's modulus (*E*) and Poisson's (υ) ratio can be calculated using the following equations[54]:

$$E = \frac{9BG}{G + 3B} \tag{I.19}$$

$$\upsilon = \frac{1}{2}\left[\frac{B - (2/3)G}{B + (1/3)G}\right] \tag{I.20}$$

Bulk modulus *B*: It may be defined as the ratio of normal stress (hydrostatic pressure) to the corresponding volumetric strain is found to be constant. It is a measure of material resistance to the change of volume.

Shear modulus or Rigidity Modulus (*G*): Is can be defined as the ratio of shear stress to the corresponding shear strain.

Young's modulus or module of elasticity (*E*): is the ratio of applied normal stress to the longitudinal strain. It is a measure of the resistance of materials to uniaxial deformation.

Poisson's Ratio (υ): It is the ratio of the lateral strain to the longitudinal strain. In addition, it is a measure of the deformation of a material in directions perpendicular to the direction of the applied stress.

The universal anisotropy index (A^U): is one of the most important materials property. For a completely isotropic crystal, A^U is equal to 0, while any deviation from 0 shows the degree of elastic anisotropy possessed by a crystal. The universal anisotropy index A^U can be evaluated using the following equation[55]:

$$A^U = \frac{5G_V}{GR} + \frac{B_V}{B_R} - 6 \qquad (\text{I}.21)$$

Pugh ratio: It may defined as the measure of material ductility based on the calculated parameters (bulk B, and shear G modulus). According to the empirical criterion of Pugh[56], a solid is brittle if the B/G ratio is less than 1.75, otherwise the material behaves in a ductile manner.

References

[1] J. Shay, L. Schiavone, E. Buehler, J. Wernick, Spontaneous-and Stimulated-Emission Spectra of CdSnP2, Journal of Applied Physics, 43 (1972) 2805-2810.

[2] J. Shay, S. Wagner, H. Kasper, Efficient CuInSe2/CdS solar cells, Applied Physics Letters, 27 (1975) 89-90.

[3] P.N. Yocom, J.P. Dismukes, Luminescent sulfides of monovalent and trivalent cations, in, Google Patents, 1976.

[4] G. Murtaza, I. Ahmad, A. Afaq, Shift of indirect to direct bandgap in going from K to Cs in MCaF 3 (M= K, Rb, Cs), Solid State Sciences, 16 (2013) 152-157.

[5] A. Verma, R. Singh, S. Rathi, An empirical model for dielectric constant and electronic polarizability of binary (A N B 8− N) and ternary (A N B 2+ N C 2 7− N) tetrahedral semiconductors, Journal of Alloys and Compounds, 486 (2009) 795-800.

[6] M. Aubert, P. Macaudiere, Rare-earth and alkali sulphide, method for preparing same and use thereof as a pigment, in, Google Patents, 2001.

[7] N. Matsuda, Light-emitting material, scintillator containing the light-emitting material, x-ray detector equipped with the scintillator, image display device using the light-emitting material, and light source using the light-emitting material, in, Google Patents, 2011.

[8] H. Lueken, W. Brüggemann, W. Bronger, J. Fleischhauer, Magnetic properties of NaCeS2 between 3.7 and 297 K, Journal of the Less Common Metals, 65 (1979) 79-88.

[9] H. Masuda, T. Fujino, N. Sato, K. Yamada, Electrical properties of Na 2 US 3, NaGdS2 and NaLaS 2, Materials research bulletin, 34 (1999) 1291-1300.

[10] M. Sato, G. Adachi, J. Shiokawa, Preparation and structure of sodium rare-earth sulfides, NaLnS2 (Ln; rare earth elements), Materials Research Bulletin, 19 (1984) 1215-1220.

[11] H. Li, W. Ding, Z. Gu, H. Li, J. Zhao, L. Fu, Preparation and infrared transmittance of NaLaS 2 ceramics, Materials Letters, 156 (2015) 62-64.

[12] M. Baenitz, P. Schlender, J. Sichelschmidt, Y. Onykiienko, Z. Zangeneh, K. Ranjith, R. Sarkar, L. Hozoi, H. Walker, J.-C. Orain, NaYbS 2: A planar spin-1 2 triangular-lattice magnet and putative spin liquid, Physical review B, 98 (2018) 220409.

[13] Z. Zangeneh, S. Avdoshenko, J. van den Brink, L. Hozoi, Single-site magnetic anisotropy governed by interlayer cation charge imbalance in triangular-lattice A Yb X 2, Physical review B, 100 (2019) 174436.

[14] X. Zhang, Z. Zhang, S. Yao, A. Chen, X. Zhao, Z. Zhou, An effective method to screen sodium-based layered materials for sodium ion batteries, npj Computational Materials, 4 (2018) 1-6.

[15] Z.-M. Xu, S.-H. Bo, H. Zhu, LiCrS2 and LiMnS2 Cathodes with Extraordinary Mixed Electron–Ion Conductivities and Favorable Interfacial Compatibilities with Sulfide Electrolyte, ACS applied materials & interfaces, 10 (2018) 36941-36953.

[16] L. Havlák, V. Jarý, M. Nikl, P. Boháček, J. Bárta, Preparation, luminescence and structural properties of RE-doped RbLaS2 compounds, Acta materialia, 59 (2011) 6219-6227.

[17] V. Jarý, L. Havlák, J. Bárta, E. Mihóková, M. Buryi, M. Nikl, ALnS2: RE (A= K, Rb; Ln= La, Gd, Lu, Y): New optical materials family, Journal of luminescence, 170 (2016) 718-735.

[18] R. Ballestracci, E.F. Lewy-Bertaut, Étude cristallographique de sulfures de terres rares et de sodium, Bulletin de Minéralogie, 87 (1964) 512-517.

[19] R. Ballestracci, Étude cristallographique de nouveaux sulfures de terres rares et de métaux alcalins M= Li, K, Bulletin de Minéralogie, 88 (1965) 207-210.

[20] W. Bronger, Ueber ternäre Sulfide mit Lanthanoiden und den Alkalimetallen Rubidium oder Cäsium, (1973).

[21] A. Verheijen, W. Van Enckevort, J. Bloem, L. Giling, Flux growth, analysis and crystallographic aspects OF alkali rare earth sulfides, Le Journal de Physique Colloques, 36 (1975) C3-39-C33-45.

[22] C. Plug, G. Verschoor, The crystal structure of KCeS2, Acta Crystallographica Section B: Structural Crystallography and Crystal Chemistry, 32 (1976) 1856-1858.

[23] C. Plug, A. Prodan, Long-and short-range ordering in LiTbS2, Acta Crystallographica Section A: Crystal Physics, Diffraction, Theoretical and General Crystallography, 34 (1978) 250-253.

[24] M. Van Dijk, C. Plug, The crystal structure of LiScS2 and NaScS2, Materials Research Bulletin, 15 (1980) 103-106.

[25] T. Ohtani, H. Honjo, H. Wada, Synthesis, order-disorder transition and magnetic properties of LiLnS2, LiLnSe2, NaLnS2 and NaLnSe2 (Ln= Lanthanides), Materials Research Bulletin, 22 (1987) 829-840.

[26] D. Kipp, T. Vanderah, Synthesis of α-NaFeO2-type LiYS2 by anion-exchange reaction, Materials Research Bulletin, 25 (1990) 933-937.

[27] W. Bronger, W. Brüggemann, M. Von der Ahe, D. Schmitz, Zur Synthese und Struktur ternärer Chalcogenide der Seltenen Erden AlnX2 mit A≙ alkalimetall und X≙ Schwefel, Selen oder Tellur, Journal of alloys and compounds, 200 (1993) 205-210.

[28] J.P. Cotter, J.C. Fitzmaurice, I.P. Parkin, New routes to alkali-metal–rare-earth-metal sulfides, Journal of Materials Chemistry, 4 (1994) 1603-1609.

[29] W. Bronger, J. Eyck, K. Kruse, D. Schmitz, Ternary rubidium rare-earth sulphides; synthesis and structure, Eur. J. Solid State Inorg. Chem, 33 (1996) 213-226.

[30] V. Jarý, L. Havlák, J. Bárta, M. Nikl, Preparation, luminescence and structural properties of rare-earth-doped RbLuS2 compounds, physica status solidi (RRL)–Rapid Research Letters, 6 (2012) 95-97.

[31] V. Jarý, L. Havlák, J. Bárta, E. Mihóková, M. Nikl, Luminescence and structural properties of RbGdS2 compounds doped by rare earth elements, Optical Materials, 35 (2013) 1226-1229.

[32] V. Jarý, L. Havlák, J. Bárta, E. Mihóková, M. Nikl, Optical properties of Eu2+-doped KLuS2 phosphor, Chemical Physics Letters, 574 (2013) 61-65.

[33] V. Jarý, L. Havlák, J. Bárta, E. Mihóková, P. Průša, M. Nikl, Optical properties of Ce3+-doped KLuS2 phosphor, Journal of luminescence, 147 (2014) 196-201.

[34] J. Fábry, L. Havlák, M. Dušek, P. Vaněk, J. Drahokoupil, K. Jurek, Structure determination of KLaS2, KPrS2, KEuS2, KGdS2, KLuS2, KYS2, RbYS2, NaLaS2 and crystal-chemical analysis of the group 1 and thallium (I) rare-earth sulfide series, Acta Crystallographica Section B: Structural Science, Crystal Engineering and Materials, 70 (2014) 360-371.

[35] L. Havlák, V. Jarý, M. Rejman, E. Mihóková, J. Bárta, M. Nikl, Luminescence characteristics of doubly doped KLuS2: Eu, RE (RE= Pr, Sm, Ce), Optical Materials, 41 (2015) 94-97.

[36] L. Havlák, V. Jarý, J. Bárta, M. Buryi, M. Rejman, V. Laguta, M. Nikl, Tunable Eu2+ emission in KxNa1− xLuS2 phosphors for white LED application, Materials & Design, 106 (2016) 363-370

[37] V. Jarý, L. Havlák, J. Bárta, M. Buryi, E. Mihóková, M. Rejman, V. Laguta, M. Nikl, Optical, Structural and Paramagnetic Properties of Eu-Doped Ternary Sulfides ALnS2 (A= Na, K, Rb; Ln= La, Gd, Lu, Y), Materials, 8 (2015) 6978-6998.

[38] V. Jarý, L. Havlák, J. Bárta, M. Buryi, M. Rejman, M. Pokorný, C. Dujardin, G. Ledoux, M. Nikl, Variability of Eu2+ Emission Features in Multicomponent Alkali-Metal-Rare-Earth Sulfides, ECS Journal of Solid State Science and Technology, 9 (2019) 016007.

[39] V. Jarý, L. Havlák, J. Bárta, M. Rejman, A. Bystřický, C. Dujardin, G. Ledoux, M. Nikl, Circadian Light Source Based on KxNa1-xLuS2: Eu2+ Phosphor, ECS Journal of Solid State Science and Technology, 7 (2017) R3182.

[40] J. Shi, T.F. Cerqueira, W. Cui, F. Nogueira, S. Botti, M.A. Marques, High-throughput search of ternary chalcogenides for p-type transparent electrodes, Scientific reports, 7 (2017) 43179.

[41] L. Azzouz, M. Halit, M. Sidoumou, Z. Charifi, A. Allal, M. Bouchenafa, H. Baaziz, Electronic Structure, Elastic and Optical Properties of AEuS2 (A= Na, K, Rb, and Cs) Ternary Sulfides: First-Principles Study, physica status solidi (b), 256 (2019) 1900136.

[42] L. He, J. Meng, J. Feng, Z. Zhang, X. Liu, H. Zhang, Insight into the Characteristics of 4f-Related Electronic Transitions for Rare-Earth-Doped KLuS2 Luminescent Materials through First-Principles Calculation, The Journal of Physical Chemistry C, 124 (2019) 932-938.

[43] A. Allal, M. Halit, S. Saib, L. Azzouz, S. Maabed, M. Bouchenafa, R. Ahuja, A comparative theoretical investigation of optoelectronic and mechanical properties of KYS2 and KLaS2, Materials Science in Semiconductor Processing, 113 (2020) 105048.

[44] A. Allal, M. Bouchenafa, M. Halit, S. Saib, Z. Liu, W. Luo, R. Ahuja, Structural stability, mechanical, electronic and optical behaviour of RbXS2 (X= Y and La) under high pressure: A first-principle study, Journal of alloys and compounds, 848 (2020) 156401.

[45] R.D. Shannon, Revised effective ionic radii and systematic studies of interatomic distances in halides and chalcogenides, Acta Crystallographica Section A: Crystal Physics, Diffraction, Theoretical and General Crystallography, 32 (1976) 751-767.

[46] B. Deng, D.E. Ellis, J.A. Ibers, New layered rubidium rare-earth selenides: Syntheses, structures, physical properties, and electronic structures for RbLnSe2, Inorganic chemistry, 41 (2002) 5716-5720.

[47] F. Wooten, Optical properties of solids, Academic press, 2013.

[48] N. Ahmed, J. Nisar, R. Kouser, A.G. Nabi, S. Mukhtar, Y. Saeed, M. Nasim, Study of electronic, magnetic and optical properties of KMS2 (M= Nd, Ho, Er and Lu): first principle calculations, Materials Research Express, 4 (2017) 065903.

[49] O. Nielsen, R.M. Martin, First-principles calculation of stress, Physical Review Letters, 50 (1983) 697.

[50] F. Mouhat, F.-X. Coudert, Necessary and sufficient elastic stability conditions in various crystal systems, Physical review B, 90 (2014) 224104.

[51] W. Voigt, Lehrbuch der Kristallphysik (Teubner, Leipzig, 1928), MATH Google Scholar, (1908) 716.

[52] A. Reuss, Berechnung der fließgrenze von mischkristallen auf grund der plastizitätsbedingung für einkristalle, ZAMM-Journal of Applied Mathematics and Mechanics/Zeitschrift für Angewandte Mathematik und Mechanik, 9 (1929) 49-58.

[53] R. Hill, The elastic behaviour of a crystalline aggregate, Proceedings of the Physical Society. Section A, 65 (1952) 349.

[54] Z.-j. Wu, E.-j. Zhao, H.-p. Xiang, X.-f. Hao, X.-j. Liu, J. Meng, Crystal structures and elastic properties of superhard Ir N 2 and Ir N 3 from first principles, Physical review B, 76 (2007) 054115

[55] S.I. Ranganathan, M. Ostoja-Starzewski, Universal elastic anisotropy index, Physical review letters, 101 (2008) 055504 .

[56] S. Pugh, XCII. Relations between the elastic moduli and the plastic properties of polycrystalline pure metals, The London, Edinburgh, and Dublin Philosophical Magazine and Journal of Science, 45 (1954) 823-843.

CHAPTER II

Theoretical and Computational Backgrounds

The atomic interactions at the Angstrom-scales can be described by quantum mechanics. At the heart of this is the many-body Schrodinger equation. However, it is impossible to solve this equation directly, so approximations are required to allow ground state solutions to be found of the studied systems. One of the most powerful and successful computational methods is density functional theory (DFT), which is extensively used to solve puzzles of many-electron problems in materials science. With a long continuous development since 1970s, the DFT approach has undoubtedly demonstrated its reliability in the prediction of electronic structures and physical properties of materials at an affordable cost. Thus, it has been considered as an extremely valuable standard determining the future of advanced materials science. Without it, would be difficult to achieve understanding the basic nature of materials, based solely on experimental strategies. In this chapter, we outline the fundamental principles and methods applied to conduct all of the calculations in this thesis. The first part describes the foundation of many-body problems in quantum mechanics. Subsequently, we present a brief concept of the DFT method along with all associated approximations that help to simplify the many-electron problems.

II.1 The Many-body problem & Schrödinger Equation


Erwin Schrödinger
1887-1961

As generally known, all physical matter is composed of combinations of atoms, and each atom consists of fundamental particles, namely electrons and nuclei. A large range of materials properties can be determined by describing the complexity of interactions between these large number of particles in matter, which known as the many-body problem. In the quantum mechanical framework, motions of particles can be described by Schrödinger wave equation [1], which expressed in the following form:

$$H\Psi = E\Psi \tag{II.1}$$

The Hamiltonian *H* is taken the following form:

$$H = T_e + T_n + V_{ee} + V_{en} + V_{nn} \tag{II.2}$$

With:

$$T_e = \frac{-\hbar^2}{2m_e}\sum_i \nabla_i^2 \,, T_n = \frac{-\hbar^2}{2M_I}\sum_I \nabla_I^2 \,, V_{ee} = \frac{1}{2}\sum_{i\neq j}\frac{\mathrm{e}^2}{|\mathrm{r}_i - r_j|},$$
$$V_{en} = \sum_{i,j}\frac{Z_I e^2}{|r_i - R_I|},\ V_{nn} = \frac{1}{2}\sum_{I\neq J}\frac{Z_I Z_J e^2}{|R_I - R_J|} \tag{II.3}$$

Where the first and second terms in equation (II.2) represent the kinetic energy operators for the electrons and nuclei, respectively. The third, fourth and fifth terms are the potential operators that describe interactions; electron-electron, electron-nucleus and nucleus-nucleus, respectively. Replacing the Hamiltonian *H* (II.2) in equation (II.1) will be possible to resolve exactly only for the hydrogen atom. While for a complex many-body problem, several approximations are required.

II.2 Born-Oppenheimer Approximation:

The Born-Oppenheimer approximation idea [2], which is called also adiabatic, is that the nucleus is 10^3-10^5 times heavier than an electron. Which can be considered relatively fixed among a number of the moving electrons. This allows neglecting the kinetic energy of nuclei, and the interactions nuclei-nuclei will be regarded as a constant to the total energy. Finally, the effect of the nucleus can be taken as an external potential V_{ext}.

$$H = \frac{-\hbar^2}{2m_e}\sum_i \nabla_i^2 + \frac{1}{2}\sum_{i\neq j}\frac{\mathrm{e}^2}{|\mathrm{r}_i - r_j|} + V_{ext} \tag{II.4}$$

So, after Born-Oppenheimer approximation the complexity of the system become much simpler. But it still too difficult to be solved.

II.3 Hartree-Fock method:

Hartree (1928) [3] considered that each electron is independent and interacts with the other electrons in an average way. This means that, an n-electron system becomes a set of no interacting one-electrons where each electron moves in the average field of the rest.

D. Hartree
1897–1958

$$\left(\frac{-\hbar^2}{2m_e}\sum_i \nabla_i^2 + V_{ext} + V_H\right)\Psi(\mathrm{r}) = E\Psi(\mathrm{r}) \qquad \text{(II.6)}$$

V_{ext} represents the interaction between electrons and nuclei, and V_H; is the Hartree potential.

Then, the wave function n-electron can be simply approximated as the product of n wave functions of one-electron.

$$\Psi = \varphi_1 \times \varphi_2 \times \ldots \times \varphi_n \qquad \text{(II.7)}$$

Fock in (1930) enhanced the Hartree method by introducing the antisymmetric principle of the wave function in the form of **Slater determination** [4]. Where, two electrons cannot occupy the same spin wave functions, and thus the Pauli's principle is satisfied. The general expression of the Slater determinant for an n-electron system is:

$$\Psi(r_1, r_2 \ldots r_n) = \frac{1}{\sqrt{n!}}\begin{vmatrix} \varphi_1(r_1) & \varphi_2(r_1) & \cdots & \varphi_n(r_1) \\ \varphi_1(r_2) & \varphi_2(r_2) & \cdots & \varphi_n(r_2) \\ \vdots & \vdots & \ddots & \vdots \\ \varphi_1(r_n) & \varphi_2(r_n) & \cdots & \varphi_n(r_n) \end{vmatrix} \qquad \text{(II.8)}$$

where $\sqrt{n!}$ is the normalization factor.

II.4 Density Functional Theory (DFT):

II.4.1 Hohenberg and Kohn theorems:

Hohenberg and Kohn[5] have proposed the first fundamental theorem of DFT in 1964. With two main theorems:

W. Kohn
1923-2016
Nobel 1998

1. The ground state energy of a system of interacting electrons in external potential $V_{ext}(r)$ is a unique function of the electronic density$\rho(r)$.

2. for any external potential, there exists a universal energy functional F[n]. The minimum value of the energy functional for a specific external potential $V_{ext}(r)$ is the

ground state energy where the density that minimizes the functional is the ground state density$\rho_0(r)$.

II.4.2 The Kohn-Sham equations:

Based on Hohenberg and Kohn theorems, the main idea of Kohn and Sham (1965) [6] to solve the many-body problem, is to replace the interactive system by a non-interactive one, assuming that gives the same ground state density as the real system. According to Kohn and Sham one-particle equations can be written as:

$$\left(\frac{1}{2}\nabla^2 + V_H[\rho(r)] + V_{ext}(r) + V_{xc}[\rho(r)]\right)\varphi_i(\mathrm{r}) = E_i\varphi_i(r) \qquad \text{(II.9)}$$

φ_i and E_i represent the wavefunction and energy of electron i resepectively.

∇ is the kinetic energy of the independent electrons, V_H is the Hartree potential,

V_{xc} is the exchange and correlation potential which can be written as:

$$V_{XC} = \frac{\partial E_{xc}}{\partial n(r)} \qquad \text{(II.10)}$$

V_{ext} is the external potential created by the nuclei, and finally $\rho(r)$ is the electronic density at position r , defined by:

$$\rho(r) = \sum_i^N \varphi_i^*(r)\varphi_i(r) \qquad \text{(II.11)}$$

So, the exchange-correlation E_{xc} is the only unknown term in Kohn and Sham equitation. A several different approximations have been made to describe this term. The next section provides a description of some Exchange-Correlation functionals.

II.5 Exchange-Correlation Functionals:

II.5.1 The Local Density Approximation (LDA):

The local-density approximation (LDA), is the simplest method for describing the exchange-correlation E_{xc} energy. The LDA approximation assumes that the charge density on the atomic scale varies slowly and that inhomogeneous electronic systems can be considered as homogeneous locally. Moreover, the exchange-correlation energy can take the following form:

$$E_{xc}^{LDA}[\rho] = \int \rho(r)\varepsilon_{xc}^{HEG}\big(\rho(r)\big)dr \qquad \text{(II.12)}$$

$\varepsilon_{xc}^{HEG}(\rho)$: is the exchange-correlation energy per electron of a homogeneous electron gas (HEG) of density ρ.

Many different correlation functionals that have been made to complement LDA functional. The most commonly used are CAPZ(Ceperley, Alder, Perdew and Zunger) [7] and VWN (Vosko, Wilk and Nusair)[8]. Even though LDA is surprisingly successful in some case, it has a serious problem, where becomes a poor approximation for energetic details, such as bond energies, energy barriers, etc. Therefore, it is of limited use in materials sciences.

II.5.2 Generalized Density Approximation (GGA):

Further than LDA which considers the exchange-correlation energy only depending on the density$\rho(r)$, the generalized gradient approximation (GGA) takes into account the gradients of the electron density. Therefore, the exchange-correlation energy at a particular point defence on both density $\rho(r)$ and its gradients of density $\nabla\rho(r)$. The exchange-correlation energy with GGA approximation can be expressed as:

$$E_{xc}^{GGA}[\rho] = \int \rho(r)\varepsilon_{xc}^{GGA}(\rho(r), \nabla\rho(r))dr \qquad \text{(II.13)}$$

In particular, the GGA-functional used in this thesis is that proposed by Perdew, Burke and Ernzerhof (PBE) [9].

Generally, GGA has succeeded with almost all systems and corrects most of the overbidding problems of LDA. Where it can give most the structural properties within a 1 to 3% error. However, it has been suffering from some limitations. The most prominent we can mention is the band gap underestimation commonly reaches up to 50% as a comparison to the experimental data.

II.5.3 SCAN (Strongly-Constrained and Appropriately-Normed) functional:

The SCAN (strongly-constrained and appropriately-normed) functional has been constructed recently in 2015 [10]. SCAN functional belongs to a class of meta-GGA functionals, which use the kinetic energy density in addition to the density and the magnitude of the gradient of the density.

of the gradient of the density.

$$E_{xc}^{SCAN} = dr\rho(r)\varepsilon_{xc}\big(\rho\uparrow(r), \rho\downarrow(r), \nabla\rho\uparrow(r), \nabla\rho\downarrow(r), \tau\uparrow(r), \tau\downarrow(r)\big) \qquad \text{(II.14)}$$

Where ε_{xc} is the exchange-correlation energy density. The kinetic energy density is defined as following:

$$\tau_\sigma(r) = \sum_i \frac{1}{2}|\nabla\varphi_{\sigma i}(r)|^2 \qquad \text{(II.15)}$$

Where $\nabla\psi_{\sigma i}$ are the Kohn-Sham single-particle wave functions. In the SCAN meta-GGA functional, a new dimensionless variable is defined as function of the kinetic energy density:

$$\alpha(r) = \frac{(\tau(r) - \tau^{w}(r))}{\tau^{unif}} \quad \text{(II.16)}$$

$\tau^{w}(r)$ is given by the weizsacker kinetic energy density,

$$\tau^{w}(r) = \frac{|\nabla\rho(r)|^2}{8\rho(r)} \quad \text{(II.17)}$$

The uniform-density limit is defined as

$$\tau^{unif}(r) = \frac{3}{10}(3\pi^2)^{2/3}\rho(r)^{5/3} \quad \text{(II.18)}$$

As matter of fact, SCAN meta-GGA has shown excellent performance. Where it has been tested for different systems and properties with improved predictive accuracy over than LDA and GGA functionals including solids [11-13], molecules [14], surfaces [15], and liquids [16-18]. Further, previous studies have revealed that SCAN functional is a better choice than PBE, LDA+U and PBE-based for the energetics and structural parameters[12]. Gives more accurate predicting for transition pressures [19, 20], reactions energies, structure parameters, volume and bulk modulus[21-23]. Also, SCAN showed an efficient prediction regarding the structural, energetic and electric properties for conventional perovskite ferroelectric materials [13, 24], accurate descriptions for the intermediate-range van der Waals (vdW) interaction[15, 25, 26]. It correctly predicts that ice is less dense than water[17], which that LDA and GGAs functionals have failed to do.

II.5.4 Hybrid functionals:

Since each approximation has its own strengths and drawbacks differently, a remarkable strategy emerged for integrating the energy of exchange-correlation based on two different methods, called hybrid functionals, which are a combination of the exchange-correlation E_{xc} within the standard DFT and the exact exchange E_x in Hartree-Fock (HF) approach. Till now, three hybrid functional formulations have been proposed:

- **B3LYP** (Becke, 3-parameter, Lee–Yang–Parr)[27]:

$$E_{xc}^{B3LYP} = E_x^{LDA} + a_0(E_x^{HF} - E_x^{LDA}) + a_x(E_x^{GGA} - E_x^{LDA}) + E_c^{LDA} + a_c(E_c^{GGA} - E_c^{LDA}) \quad \text{(II.19)}$$

Where E_x^{GGA} and E_c^{GGA} are, respectively, Becke's exchange and Lee–Yang– Parr's correlation functionals in the GGA, while E_x^{LDA} and E_c^{LDA} denotes, respectively, the ordinary exchange and Vosko–Wilk–Nusair's correlation functionals in the LDA. The mixing parameters: $a_0 = 0.20$, $a_x = 0.72$, $a_c = 0.81$.

- **PBE0** [28]:

$$E_{xc}^{PBE0} = \frac{1}{4}E_x^{HF} + \frac{3}{4}E_x^{PBE} + E_c^{PBE} \quad \text{(II.20)}$$

Where E_x^{HF} is the Hartree–Fock exact exchange functional, E_x^{PBE} and E_c^{PBE} are, respectively, the exchange and correlation in PBE functional.

- HSE (Heyd–Scuseria–Ernzerhof)[29]:

$$E_{xc}^{HSE}(\omega) = \alpha E_x^{HF,SR}(\omega) + (1-\alpha)E_x^{PBE,SR}(\omega) + E_x^{PBE,LR}(\omega) + E_c^{PBE} \quad \text{(II.21)}$$

Where SR and LR stand for the short-range and long-range components, respectively. α is a mixing parameter and ω is an adjustable parameter controlling the short-rangeness of the interaction. For HSE06 α and ω are 0.25 and 0.2Å^{-1}, respectively.

II.6 Computational methods

II.6.1 Bloch's Theorem and Plane Wave Basis Sets

F. Bloch
1905-1983

The real bulk material is an infinite number of electrons moving in the static potential of an infinite number of ions. This leads to a very big domain of the wave functions in the entire space in the crystalline. Therefore, it still difficult for DFT to solve the problem. According to Bloch's theorem, and based on the periodic nature of the crystals[30, 31]; it is possible to represent these wave functions based on the plane-wave basis set with a periodic function,

$$\varphi(r)_{j,k} = e^{ik.r}\phi_{j,k}(r) \quad \text{(II.22)}$$

M. Brillouin
1854-1948

The k denotes a reciprocal vector of a Bravais lattice in the first Brillouin zone. $\phi_{j,k}(r)$ is the periodic function of the crystal lattice which can be expanded in Fourier series as following:

$$\phi_{j,k}(r) = \sum_G C_{j,G}e^{iG.r} \quad \text{(II.23)}$$

With, **G** is a wavevector within the first Brillouin zone and $C_{j,G}$ is the plane wave coefficients. The full wave function takes the form:

$$\varphi(r)_{j,k} = \frac{1}{\sqrt{V_{cell}}}\sum_G C_{j,(k+G)}e^{i(k+G),r} \quad \text{(II.24)}$$

V_{cell} is the volume of the unit cell.

By the use of Bloch's theorem, another problem will be created, i.e., expressing the wave function in terms of an infinite number of reciprocal space vectors within the first Brillouin

zone. However, as the wave function varies slowly, in other words, the wave functions for the values k over small regions of k-space are almost identical. Therefore, a finite number of distinct k-points can be sampled, which essentially represent a whole k-space. In practice, we determine the sufficiently high number of k-points of the studied system from the convergence in its total energy.

II.6.2 Pseudopotentials:

The key points are that the core electrons shielded by the valence electrons, as well the most physical properties are more depending on the valence band. Therefore, the system can be divided into two groups, effectively freezing the nucleus and the core electrons together, and valence electrons.

One might say that electrons are all the same as each other in an atomic system in the sense that they normally have the same mass, charges, spin-ups and downs, etc. Yet their role, depending on where they are, is very different. As atoms get together to create a solid, the core electrons stick tightly to their nucleus in a deep potential well and remain unchanged under certain situations, the core electrons stay that well and rarely contribute in any change of the system. In other terms, they are so localized and only oscillate rapidly because of the strong Coulomb potential by nuclei, where they do not notice whether they are in an isolated atom or in a solid. Thus, when isolated atoms are brought together to form a material, the core electrons' contribution to bonding is minimum. On the contrary, the valence electrons far from the nucleus and their potential well are rather independent and quite active in everything. They are responsible for forming bonds, conducting electricity, being ionized, forming bands, and performing other atomic activities. In metals, they can even be moving in the whole solid.

In practice, the pseudopotentials are constructed by Choosing a proper r_c, where the pseudopotential and the pseudo-wave functions must be identical to the true potential and all-electron wave functions for $r > r_c$.

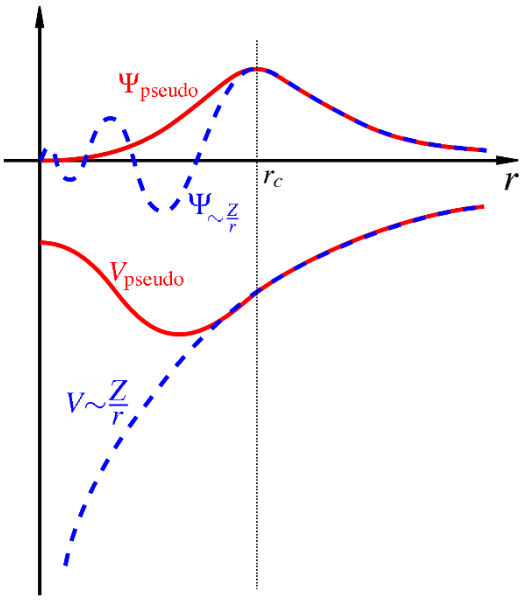

Figure II.1 Schematic of a pseudo wave function and pseudopotentials.

II.6.3 Norm-conserving Pseudopotentials:

Hamann et al (HSC) first proposed Norm-conserving pseudopotential in 1979 [32] and further developed by Kleinman and Bylander [33]. Here, the pseudo- and all-electron charge densities within the core are constructed to be equal for $r < r_c$.

$$\int_0^{r_c} |\Psi_{PP}(r)|^2 dr = \int_0^{r_c} |\Psi_{AE}(r)|^2 dr \qquad \text{(II.25)}$$

$\Psi_{PP}(r)$ is the pseudo wave function and $\Psi_{AE}(r)$ is the all electron wave function.

II.6.4 PAW method:

Projector Augmented Waves (PAW) method first proposed by Blöchl (1994) [34]. Where unifies the efficiency of pseudopotentials and the accuracy of the all-electron potential. Since wave functions oscillate rapidly near the nucleus due to the requirement that they be orthogonal to core states; which requires many Fourier components to describe the wave functions accurately. The PAW approach transforms these rapidly oscillating wave functions into smooth wave functions.

The linear transformation $\mathcal{T}$ which describe the relation between all-electron wave function Ψ_q and the smooth wave function $\widetilde{\Psi}_q$:

$$|\Psi\rangle = \mathcal{T}|\widetilde{\Psi}\rangle \qquad \text{(II.26)}$$

With

$$\mathcal{T} = 1 + \sum_R \tilde{\mathcal{T}}_R \quad \text{(II.27)}$$

Not that $\mathcal{T}$ acts only inside the core region (Ω_R), while the all-electron (AE) and pseudo (PS) must be identical outside.

Inside the core region, it is possible to expand the pseudo waves into spatial waves partial waves

$$\tilde{\Psi} = \sum_i |\tilde{\phi}_i\rangle c_i \quad \text{(II.28)}$$

The all-electron wave function then can take be expressed

$$|\Psi\rangle = \mathcal{T}|\tilde{\Psi}\rangle = |\tilde{\phi}_i\rangle c_i \quad \text{(II.29)}$$

c_i are linear functions of the pseudo wave functions take the following form:

$$c_i = \langle \tilde{p}_i | \tilde{\phi}_i \rangle \quad \text{(II.30)}$$

We consider

$$\sum_i |\tilde{\phi}_i\rangle\langle\tilde{p}_i| = 1 \quad \text{(II.31)}$$

Which implies that

$$\langle \tilde{p}_i | \tilde{\phi}_j \rangle = \delta_{ij} \quad \text{(II.32)}$$

So the linear transformation we can write as:

$$\mathcal{T} = 1 + \sum_i (|\phi_i\rangle - |\tilde{\phi}_i\rangle)\langle\tilde{p}_i| \quad \text{(II.33)}$$

The final form of all-electro wave function given in (2.29) is:

$$|\Psi\rangle = |\tilde{\Psi}\rangle + \sum_i (|\phi_i\rangle - |\tilde{\phi}_i\rangle)\langle\tilde{p}_i|\tilde{\Psi}\rangle \quad \text{(II.34)}$$

II.6.5 Softwares and input files:

Until date, many codes based on DFT to solve the equations in a self-consistent manner have been developed. Each code has different strengths and weaknesses. We can mention as an example:

- Plane-wave pseudopotentials (PW-PP) software like VASP[35], CASTEP[36] and QUANTUM ESPRESSO[37].
- All-electron software like Wien2k[51] and Elk[38].
- Linear scaling software like ONETEP[39].

All the calculations in this research have been done using both CASTEP and VASP codes.

II.6.6 CASTEP package:

CASTEP (Cambridge Serial Total Energy Package) is an academic and commercial software package, which uses density functional theory (DFT) or Hartree-Fock (HF) scheme with plane-wave pseudopotential (PW-PP). It treats materials as periodic supercell, which makes it most suitable for crystal solids simulation. However, it can also be used for surfaces, molecules, liquids and amorphous materials. It could be applied to calculate a huge range of material properties including Energies and enthalpies of electronic systems, Structural properties (lattice parameters and atomic positions), electronic properties, vibrational and thermodynamic properties. On the other hand, by using CASTEP a wide range of spectroscopic features such as infra-red and Raman spectroscopies, NMR, and core level spectra, which link directly to experiment can be determined.

The first version was written in Fortran 77, by TCM Group of the Cavendish Laboratory in Cambridge University in the late 1980s and early 1990s. Form 1999-2001was completely rewritten using Fortran 95 and MPI by researchers at the Universities of York, Cambridge, Durham, St. Andrews, and Rutherford Labs.

II.6.7 VASP code:

The Vienna ab-initio Simulation package (VASP) is a software package for performing *ab initio* and quantum molecular dynamics (MD) calculations based on density functional theory (DFT) or Hartree-Fock (HF) scheme, with the plane-wave (PW) basis set. Pseudopotentials approach (PP), or the projector augmented wave method (PAW), are used to describe the interactions between ions and electrons. VASP relaxes the atoms into their instantaneous ground-state by calculating Forces and the full stress tensor. A rather ``traditional" and ``old fashioned" self-consistency cycle are used to calculate the electronic ground-state.

For a standard production runs, VASP needs four major input files written in uppercase: INCAR, POSCAR, POTCAR and KPOINT.

The INCAR file is the central input file of VASP. Contain a range of keywords (tags) by set each tag in one line or several tags on a single line (tag = value or word) separated by a semicolon ';'. By means of these tags, we can determine the kind of calculation (static calculation, geometry optimization, DOS, dielectric properties...), and how to do it (required precision, requested convergence, functional, algorithms...).

The POSCAR file contains all the information on the starting lattice geometry including crystal structure type, lattice parameters and ionic positions.

The POTCAR file contains the relevant information concerning the pseudopotentials for each atomic species used in the calculation. If the system contains more than one atomic species, the corresponding POTCAR files should have all the pseudopotentials of atoms, concatenated in the same order as the atomic species are given in the POSCAR file.

The KPOINTS file is used to specify the Bloch vectors (k-points) that will be used to sample the first Brillouin zone in the calculation.

References:

[1] E. Schrödinger, An undulatory theory of the mechanics of atoms and molecules, Physical review, 28 (1926) 1049.

[2] M. Born, R. Oppenheimer, Zur quantentheorie der molekeln, Annalen der physik, 389 (1927) 457-484.

[3] L. Brillouin, Les champs" self-consistents" de Hartree et de Fock, Paris, 1934.

[4] J.C. Slater, The theory of complex spectra, Physical review, 34 (1929) 1293.

[5] P. Hohenberg, W. Kohn, Physical review 136, B864, (1964).

[6] W. Kohn, L.J. Sham, Self-consistent equations including exchange and correlation effects, Physical review, 140 (1965) A1133.

[7] D.M. Ceperley, B.J. Alder, Ground state of the electron gas by a stochastic method, Physical Review Letters, 45 (1980) 566.

[8] S.H. Vosko, L. Wilk, M. Nusair, Accurate spin-dependent electron liquid correlation energies for local spin density calculations: a critical analysis, Canadian Journal of physics, 58 (1980) 1200-1211.

[9] J.P. Perdew, K. Burke, M. Ernzerhof, Generalized gradient approximation made simple, Physical Review Letters, 77 (1996) 3865.

[10] J. Sun, A. Ruzsinszky, J.P. Perdew, Strongly constrained and appropriately normed semilocal density functional, Physical Review Letters, 115 (2015) 036402.

[11] F. Tran, J. Stelzl, P. Blaha, Rungs 1 to 4 of DFT Jacob's ladder: Extensive test on the lattice constant, bulk modulus, and cohesive energy of solids, The Journal of chemical physics, 144 (2016) 204120.

[12] Y. Hinuma, H. Hayashi, Y. Kumagai, I. Tanaka, F. Oba, Comparison of approximations in density functional theory calculations: Energetics and structure of binary oxides, Physical review B, 96 (2017) 094102.

[13] Y. Zhang, J. Sun, J.P. Perdew, X. Wu, Comparative first-principles studies of prototypical ferroelectric materials by LDA, GGA, and SCAN meta-GGA, Physical review B, 96 (2017) 035143.

[14] L. Goerigk, A. Hansen, C. Bauer, S. Ehrlich, A. Najibi, S. Grimme, A look at the density functional theory zoo with the advanced GMTKN55 database for general main group thermochemistry, kinetics and noncovalent interactions, Physical Chemistry Chemical Physics, 19 (2017) 32184-32215.

[15] A. Patra, J.E. Bates, J. Sun, J.P. Perdew, Properties of real metallic surfaces: Effects of density functional semilocality and van der Waals nonlocality, Proceedings of the National Academy of Sciences, 114 (2017) E9188-E9196.

[16] R.C. Remsing, M.L. Klein, J. Sun, Dependence of the structure and dynamics of liquid silicon on the choice of density functional approximation, Physical review B, 96 (2017) 024203.

[17] M. Chen, H.-Y. Ko, R.C. Remsing, M.F.C. Andrade, B. Santra, Z. Sun, A. Selloni, R. Car, M.L. Klein, J.P. Perdew, Ab initio theory and modeling of water, Proceedings of the National Academy of Sciences, 114 (2017) 10846-10851.

[18] G. Zhao, S. Shi, H. Xie, Q. Xu, M. Ding, X. Zhao, J. Yan, D. Wang, Equation of state of water based on the SCAN meta-GGA density functional, Physical Chemistry Chemical Physics, 22 (2020) 4626-4631.

[19] C. Shahi, J. Sun, J.P. Perdew, Accurate critical pressures for structural phase transitions of group IV, III-V, and II-VI compounds from the SCAN density functional, Physical review B, 97 (2018) 094111.

[20] N. Sengupta, J.E. Bates, A. Ruzsinszky, From semilocal density functionals to random phase approximation renormalized perturbation theory: A methodological assessment of structural phase transitions, Physical review B, 97 (2018) 235136.

[21] X. Zhang, Z. Zhang, S. Yao, A. Chen, X. Zhao, Z. Zhou, An effective method to screen sodium-based layered materials for sodium ion batteries, npj Computational Materials, 4 (2018) 1-6.

[22] G.-X. Zhang, A.M. Reilly, A. Tkatchenko, M. Scheffler, Performance of various density-functional approximations for cohesive properties of 64 bulk solids, New Journal of Physics, 20 (2018) 063020.

[23] C.J. Bartel, A.W. Weimer, S. Lany, C.B. Musgrave, A.M. Holder, The role of decomposition reactions in assessing first-principles predictions of solid stability, npj Computational Materials, 5 (2019) 1-9.

[24] B.J. Kennedy, Q. Zhou, S. Zhao, F. Jia, W. Ren, K.S. Knight, Low-temperature structure and the ferroelectric phase transitions in the CdTi O 3 perovskite, Physical review B, 96 (2017) 214105.

[25] J. Sun, R.C. Remsing, Y. Zhang, Z. Sun, A. Ruzsinszky, H. Peng, Z. Yang, A. Paul, U. Waghmare, X. Wu, Accurate first-principles structures and energies of diversely bonded systems from an efficient density functional, Nature chemistry, 8 (2016) 831.

[26] J.H. Yang, D.A. Kitchaev, G. Ceder, Rationalizing accurate structure prediction in the meta-GGA SCAN functional, Physical review B, 100 (2019) 035132.

[27] A.D. Becke, Density-functional thermochemistry. I. The effect of the exchange-only gradient correction, The Journal of chemical physics, 96 (1992) 2155-2160.

[28] C. Adamo, V. Barone, Toward reliable density functional methods without adjustable parameters: The PBE0 model, The Journal of chemical physics, 110 (1999) 6158-6170 DOI.

[29] J. Heyd, G.E. Scuseria, M. Ernzerhof, Hybrid functionals based on a screened Coulomb potential, The Journal of chemical physics, 118 (2003) 8207-8215.

[30] C. Kittel, P. McEuen, Introduction to solid state physics, Wiley New York, 1996.

[31] F. Bloch, Über die quantenmechanik der elektronen in kristallgittern, Zeitschrift für physik, 52 (1929) 555-600.

[32] D. Hamann, M. Schlüter, C. Chiang, Norm-conserving pseudopotentials, Physical Review Letters, 43 (1979) 1494.

[33] L. Kleinman, D. Bylander, Efficacious form for model pseudopotentials, Physical Review Letters, 48 (1982) 1425.

[34] P.E. Blöchl, Projector augmented-wave method, Physical review B, 50 (1994) 17953.

[35] J. Hafner, G. Kresse, D. Vogtenhuber, M. Marsman, The Vienna Ab initio Simulation Package (VASP), in, University of Vienna: Vienna, Austria, 2017.

[36] S.J. Clark, M.D. Segall, C.J. Pickard, P.J. Hasnip, M.I. Probert, K. Refson, M.C. Payne, First principles methods using CASTEP, Zeitschrift für Kristallographie-Crystalline Materials, 220 (2005) 567-570.

[37] P. Giannozzi, S. Baroni, N. Bonini, M. Calandra, R. Car, C. Cavazzoni, D. Ceresoli, G.L. Chiarotti, M. Cococcioni, I. Dabo, QUANTUM ESPRESSO: a modular and open-source software project for quantum simulations of materials, Journal of physics: Condensed matter, 21 (2009) 395502.

[38] P. Blaha, K. Schwarz, F. Tran, R. Laskowski, G.K. Madsen, L.D. Marks, WIEN2k: An APW+ lo program for calculating the properties of solids, The Journal of chemical physics, 152 (2020) 074101.

[39] C.-K. Skylaris, P.D. Haynes, A.A. Mostofi, M.C. Payne, Introducing ONETEP: Linear-scaling density functional simulations on parallel computers, The Journal of chemical physics, 122 (2005) 084119.

CHAPTER III

Study of ternary ABS_2 (A= K, Rb; B=Sc, Y, La and Lu)

III.1 Introduction

Wide bandgap (WBG) and ultra-wide bandgap (UWBG) semiconductors, is a modern area of research that is exciting and demanding in materials sciences and applications. This kind of semiconductors has potential advantages over than narrower-bandgap in many relevant fields like; deep-UV optoelectronics high-power and RF electronics, as well as in transparent semiconducting, and quantum information, power switching and power amplifier applications as well [1-10].

Recently, very interesting ultra-wide bandgap (UWBG) semiconductors ABS_2 (A= alkali metal and B = rare earth metal), have been investigated. These ternary materials are promising candidate for a lot of applications for including infrared windows materials, Na-ion batteries, and some of them have excellent semi conductive behaviors [11-20]. In recent researches, ABS_2 compounds with A=K and Rb, have become the subject of interest, they have been intensively searched for their scintillation and luminescence properties, due to their potential applications for X-ray and white LED phosphors, when doped with rare-earth elements[21-27]. The isostructural compounds $KScS_2$, KYS_2, $KLaS_2$, $KLuS_2$, $RbScS_2$, and $RbLuS_2$ have been synthesized by a chemical reaction in an electric resistance furnace under the flow of hydrogen sulfide in the crystalline hexagonal platelets form. Their crystal structures were determined by X-ray powder diffraction, these results are reported in [28, 29]. Their experimental band gaps are 4.01 eV, 3.82 eV, 4.03 eV, and 4.00 eV in KYS_2, $KLaS_2$, $KLuS_2$, and $RbLuS_2$ [30], respectively. No experimental band gap reported for $KScS_2$ and $RbScS_2$ in the literature. The theoretical band gap of $KScS_2$, KYS_2 , and $RbScS_2$ are 2.89, 3.37 2.88 eV[31], respectively, and 2.39 for $KLuS_2$ [32]. The optical properties of

RE-doped ternary sulfides ABS_2 (A= K, Rb. B= Y, La, Gd, and Lu. RE=Ce, Pr, Sm, Eu, Tb, Tm) were investigated by means of electron paramagnetic resonance, X-ray excited fluorescence and me-resolved luminescence spectroscopy [30, 33, 34], where KYS_2 and $KLaS_2$, $KLuS_2$, $RbLuS_2$ showed prospective applications for X-ray phosphors and materials for white LED solid-state lighting. Theoretically, $KScS_2$, KYS_2 and $RbScS_2$ was studied for p-type transparent electrodes using hybrid functional (HSE06) [31].

To the best of our knowledge, the physical properties of pure $KScS_2$, KYS_2, $KLaS_2$, $KLuS_2$, $RbLuS_2$, and $RbScS_2$, are still obscure. Our ambition is to offer additional information on the physical properties of these materials from the first-principle calculations, which can be used to reveal the potential technological applications of these ternary materials. In this chapter, comparative investigations of the structural, elastic properties, electronic structures, optical constants and thermodynamic properties of $KScS_2$, KYS_2, $KLaS_2$, $KLuS_2$, $RbScS_2$, and, $RbLuS_2$ are carried out using density functional theory (DFT) calculations and the quasi-harmonic Debye model.

III.2 COMPUTITIONAL DETAILS

In order to get theoretical insight into the ground state properties, the density functional theory (DFT) based calculations have been performed using pseudopotential plane-wave approach (PP-PW), implemented in the CASTEP code [35]. The exchange–correlation effects are considered as both generalized gradient approximation in the form of Perdew–Burke–Ernzerhof (GGA-PBE) [36], and local density approximation of Ceperley and Alder as parameterized by Perdew and Zunger (LDA-CAPZ) [37, 38]. It has been reported in the –literatures that both LDA and GGA underestimates the band gaps [39], therefore, Becke, 3-parameter, Lee–Yang–Parr hybrid functional (B3LYP)[40] has been employed for better accuracy in the electronic structure and optical properties of the investigated materials. The interactions of ion cores with valence electrons are modeled using norm-conserving pseudopotentials [41]. The K-$3s^2\ 3p^6\ 4s^1$, Rb-$s^2\ 4p^6\ 5s^1$, Sc-$3d^1\ 4s^2$, Y-$4d^1\ 5s^2$, La-$5d^1\ 6s^2$, Lu-$4f^{14}\ 5s^2\ 5p^6\ 5d^1\ 6s^2$, and S-$3s^2\ 3p^4$ electron states are considered explicitly as valence electronic states. The energy cut off of plane waves is set to be 1200 eV for GGA-PBE and LDA, and 400eV in case of the hybrid functional B3LYP. We have sampled the Brillouin zone using a 8×8×6 Monkhorst-Pack special *k*-mesh [42] for GGA-PBE and LDA, while 3×3×2 mesh is used in case of B3LYP functional. The convergence tolerance is set to 1×10^{-6} eV/atom, the maximum ionic force, maximum stress and maximum displacement are less than 1×10^{-4} eV/Å, 1×10^{-4} GPa and 1×10^{-4} Å

respectively. Single elastic constants C_{ij} are determined by applying the stress–strain approach [43] based on Hook's law, with the following convergences criteria: 10^{-6} eV/atom for the total energy precision, 0.002 eV/Å for ionic Hellmann–Feynman force, and 1×10^{-4} Å for maximum ionic displacement.

III.3 Structural properties

As we have mentioned previously (Chapter I), the ternary semiconductors $KScS_2$, KYS_2, $KLaS_2$, $KLuS_2$, $RbScS_2$ and $RbLuS_2$, adopt the layers' rhombohedral structure (space group R-3m, number 166) described by $a = b = c$ and $\alpha = \beta = \gamma \neq 90°$. The premetive cell of this structure contains a single formula ***figure III.1***. Here in ABS_2, all A, B, and S atoms are surrounded by six atoms, the alkali metal (K and Rb) and rare earth atoms by six sulfurs (AS_6, and BS_6 octahedral), while the sulfur atom is surrounded by three alkali atoms and three rare earth atoms[44-46]. This structure often described by hexagonal system, where one conventional unit cell in the hexagonal crystal contains three rhombohedral primitive unit cells (***figure III.1***).

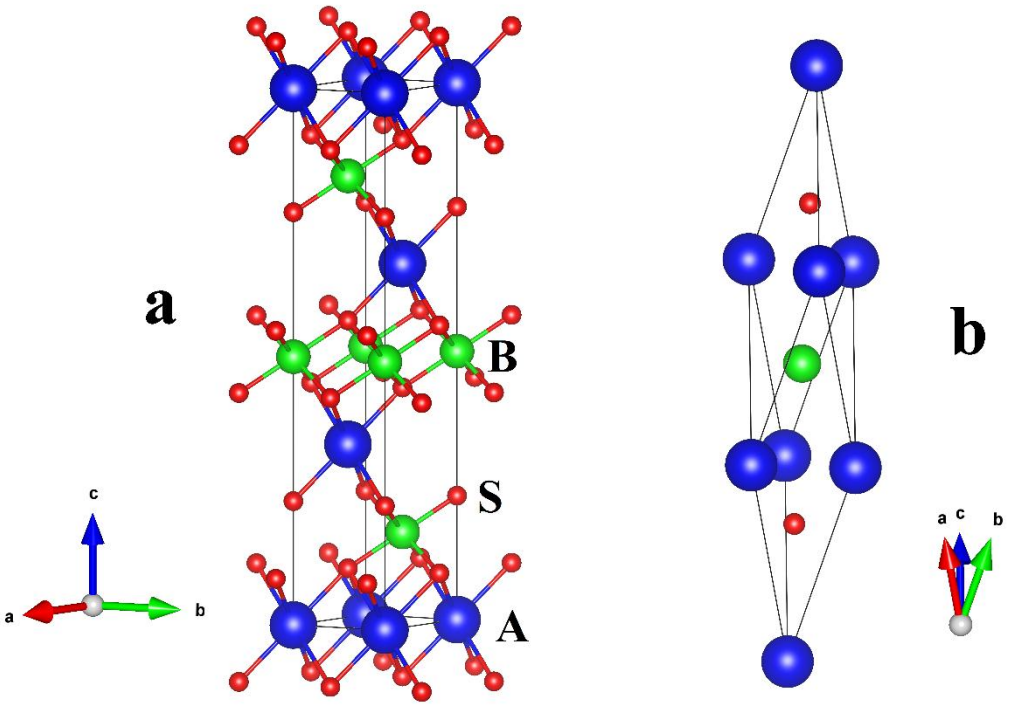

Figure III.1: *schematic representation* ***(a)*** *Hexagonal conventional unit cell and* ***(b)*** *rhombohedral primitive unit cell of* ABS_2.

The first important step in an ab-initio calculation is the determination of the structural properties of the considered material. Knowledge of this information allows us to investigate the other physical properties (electronic, optical, thermodynamic, etc.). The ground state structural parameters of $KScS_2$, KYS_2, $KLaS_2$, $KLuS_2$, $RbScS_2$ and $RbLuS_2$ materials are optimized at 0 GPa and 0 K, using the Broyden–Fletcher–Goldfarb–Shanno [BFGS] algorithm [47]. ***Table III.1*** summarizes the equilibrium lattice parameters *a* and *c*, volume of unit cell, interatomic distance and the ratio c/a, of the studied materials using both LDA and GGA-PBE functionals, along with corresponding experimental values [28].

Table III.1*: The calculated unit-cell parameters (a and c, in Å), the lattice parameter ratio c/a, the internal parameter z(S), unit-cell volume (V in Å^3), interatomic distance (A^+–S and B^{3+}–S, in Å), and thickness of cationic layers ($h(A^+S_6)$ and $h(B^{3+}S_6)$, in Å).*

	Method	$KScS_2$	KYS_2	$KLaS_2$	$KLuS_2$	$RbScS_2$	$RbLuS_2$
a	**GGA**	3.852	3.973	4.171	4.023	3.876	4.048
	LDA	3.785	3.920	4.125	3.898	3.802	3.915
	EXP	3.811[a]	4.022[b]	4.265[b]	3.949[b]	3.830[a]	3.991[c]
c	**GGA**	21.854	22.03	22.061	22.096	22.682	22.943
	LDA	21.250	21.389	21.330	21.370	22.117	22.253
	EXP	21.719	21.884	21.929	21.871	22.656	22.838
c/a	**GGA**	5.67342	5.545	5.289	5.492	5.852	5.668
	LDA	5.61427	5.456	5.171	5.482	5.817	5.684
	EXP	5.699	5.441	5.141	5.538	5.915	5.722
***z*(S)**	**GGA**	0.2308	0.2332	0.2350	0.2338	0.2280	0.2309
	LDA	0.2329	0.2358	0.2377	0.2348	0.2300	0.2318
	EXP	0.2311	0.2344	0.2372	0.2337	0.2281	0.2303
V	**GGA**	280.82	301.19	332.40	309.70	295.10	325.58
	LDA	263.64	284.63	314.31	281.20	276.87	295.38
	EXP	273.18	306.51	345.47	295.37	287.81	315.03
A–S*	**GGA**	3.156	3.182	3.241	3.197	3.27	3.314
	LDA	3.053	3.078	3.136	3.081	3.168	3.196
	EXP	3.125	3.174	3.242	3.154	3.251	3.293
B–S*	**GGA**	2.629	2.722	2.841	2.757	2.636	2.763
	LDA	2.600	2.703	2.823	2.681	2.604	2.685
	EXP	2.608	2.755	2.907	2.710	2.613	2.724
h*(AS_6)*	**GGA**	4.479	4.411	4.338	4.395	4.774	4.699
	LDA	4.265	4.172	4.080	4.209	4.568	4.519
	EXP	4.439	4.328	4.217	4.358	4.768	4.706
h*(BS_6)*	**GGA**	2.805	2.931	3.015	2.970	2.786	2.949
	LDA	2.818	2.957	3.030	2.914	2.804	2.898
	EXP	2.800	2.966	3.093	2.932	2.784	2.906

[a]:[28], [b]:[29], [c]:[48]

* $d^2(X-S) = \frac{1}{3}a^2 + \frac{1}{4}h^2(XS_6)$. Here $X = A$ or B

** $h(AS_6)2c\left(\frac{1}{3} - z(S)\right), h(BS_6) = c(2z(S) - \frac{1}{3})$

As can be seen from ***Table III.1***, our values of structural parameters obtained either by GGA or by LDA are in excellent concordance with the experimental values. In addition, ***Table III.1*** confirm that switching from LDA to GGA improves the results found compared to the experimental data; better results are obtained with the GGA method.

The relative deviation of the optimized volume cell *V* in $KScS_2$, KYS_2, $KLaS_2$, $KLuS_2$, $RbScS_2$ and $RbLuS_2$, employing GGA (LDA), are less than 02,79 % (3,49 %), 01,73 % (07,14 %), 03,78 % (09,02 %), 04,85 % (04,79 %), 02,53 % (03,80 %), and 03,35 %(06,24 %), respectively. We can conclude that this computational methodology is reliable and can be employed to investigate other physical properties as well. It can be noticed from the table that, material with larger atomic size has larger unit-cell parameters.

III.4 Elastic properties

Elastic constants are very important quantities to describe the mechanical properties of materials. They are evidently and directly employed to evaluate the elastic strains or energies in materials under stress of various origins: external, internal, thermal, etc. Values of elastic constants provide valuable information on the structural stability, the bonding characteristic between adjacent atomic planes, and the anisotropic character of the bonding, determining the strength of the material [49, 50]. The rhombohedral (R-3m) structure is described by six different elastic constants namely: (C_{11}, C_{12}, C_{13}, C_{14}, C_{33}, and C_{44}), since $C_{66} = 1/2(C_{11}-C_{12})$. The evaluated elastic constants C_{ij} for the optimized crystal structures of $KScS_2$, KYS_2, $KLaS_2$, $KLuS_2$, $RbScS_2$ and $RbLuS_2$ materials using GGA and LDA are depicted in ***Table III.2***. Till date, there are neither experimental nor theoretical results existing in the literature, for the elastic constants of the considered semiconductors to be compared with our theoretical results. All the C_{ij} are positive and satisfy simultaneously the mechanical stability criteria of a rhombohedral crystal [51]:

$$C_{11} > |C_{12}|;\ C_{44} > 0, C_{13}^2 < \frac{1}{2}C_{33}(C_{11} + C_{12}), C_{14}^2 < \frac{1}{2}C_{44}(C_{11} - C_{12}) = C_{44} + C_{66} \quad \text{(III.1)}$$

The elastic constants C_{11} and C_{33}, reflect the resistance of crystals to the linear compression along [100] and [001] directions respectively. Where, the larger value indicating the high resistance to the uniaxial stress. While, resistance ability against shear deformation along the [001] and [110] directions on the (100) plane, can be described by the elastic constants C_{44} and C_{66}, respectively[52, 53].

Table III.2: *Calculated elastic constants (C_{ij}, in GPa) for $KScS_2$, KYS_2, $KLaS_2$, $KLuS_2$, $RbScS_2$ and $RbLuS_2$ using two functional GGA and LDA.*

		C_{11}	C_{33}	C_{44}	C_{12}	C_{13}	C_{14}	C_{66}
$KScS_2$	GGA	96.55	88.23	29.45	27.03	25.86	9.85	34.76
	LDA	106.29	97.91	37.36	30.51	32.78	14.00	37.89
KYS_2	GGA	100.57	79.02	34.47	25.49	25.68	11.82	37.54
	LDA	107.59	88.52	35.72	27.83	31.22	13.92	39.88
$KLaS_2$	GGA	93.86	62.92	28.46	22.64	22.25	10.28	35.61
	LDA	99.47	68.9	29.85	26.29	27.88	10.74	36.59
$KLuS_2$	GGA	90.09	71.90	28.18	23.78	24.29	9.86	33.16
	LDA	105.84	86.21	37.33	27.81	33.24	15. 50	39.01
$RbScS_2$	GGA	89.35	91.12	28.57	25.33	24.89	9.59	32.01
	LDA	98.56	107.77	38.55	29.14	33.89	14.17	34.71
$RbLuS_2$	GGA	82.97	76.81	26.26	22.02	23.57	9.44	30.47
	LDA	97.19	94.93	37.77	25.75	32.68	15.43	35.72

The studied materials are characterized by a high value of C_{11} and C_{33} compared to the other elastic constants. Which means that they are more resistant to unidirectional compression than to shear deformations.

For all the considered compounds, the elastic constant C_{11} value is slightly larger than C_{33} indicating that the resistance for compression along the [100] direction is larger than that along the [001] except for RbScS2 which has C_{33} larger than C_{11}. However, can notice that the difference value between C_{11} and C_{33}, increase along $KScS_2 < KYS_2 < KLuS_2 < KLaS_2$. Which is in fact with increase the ionic radii of the trivalent cation (see ***table S2*** in the annexe). For all the studied materials C66 > C44, suggests that [100](001)shear is easier than shear [100](010).

The elastic constants obtained by the LDA calculations are relatively higher than those obtained by GGA method. This can be explained by the fact that the values of the lattice parameters and the interatomic distances calculated by the GGA are relatively greater than those calculated by LDA.

It is well-known, that the elastic constants C_{ij}, allow us to calculate the macroscopic elastic parameters, for instance, the bulk B and the shear G modulus. The bulk modulus B, and shear G, can be determined by applying the Voigt-Reuss-Hill relations (VRH) [54-56] (chapter I).

The Young's modulus E and the Poisson's ratio ν can be evaluated employing the equations[57].

The calculated values of these aforementioned parameters are listed in ***Table III.3***. The bulk B and the shear G modulus represent the volume change of crystals under pressure and the shape deformation under shear forces, respectively. The larger value of B and G corresponding to the most incompressible and least shape change, respectively[58, 59].

Table III.3: *bulk modulus (B, in GPa), shear modulus (G, in GPa), Young's modulus (E, in GPa), Poisson's ratio (ν, dimensionless), and B/G ratio, using GGA and LDA.*

		B_R	B_V	B_H	G_R	G_V	G_H	E	ν	B/G
$KScS_2$	**GGA**	48.76	48.66	48.71	32.24	29.56	30.90	76.51	0.238	1.57
	LDA	55.85	55.81	55.82	36.82	32.63	34.72	86.28	0.242	1.61
KYS_2	**GGA**	48.21	47.65	47.93	34.85	31.59	33.22	80.96	0.22	1.44
	LDA	53.81	53.52	53.66	36.49	32.25	34.375	84.979	0.236	1.56
$KLaS_2$	**GGA**	42.77	41.35	42.06	30.74	27.53	29.136	71.01	0.22	1.44
	LDA	47.99	46.77	47.38	31.64	28.33	29.98	74.28	0.238	1.60
$KLuS_2$	**GGA**	43.15	42.63	43.87	30.07	27.39	28.51	70.30	0.233	1.54
	LDA	54.06	53.80	53.93	36.31	31.18	33.75	83.76	0.241	1.60
$RbScS_2$	**GGA**	46.67	46.67	46.67	30.81	28.14	29.48	73.05	0.239	1.58
	LDA	55.41	55.21	55.31	36.23	31.70	33.95	84.56	0.245	1.63
$RbLuS_2$	**GGA**	42.34	42.31	42.33	28.17	25.49	26.83	66.46	0.238	1.58
	LDA	52.392	52.37	52.38	35.46	30.26	32.86	81.53	0.240	1.59

The computed bulk modulus B, shear modulus G, and Young's modulus E of $KScS_2$, KYS_2 and $RbScS_2$ are slightly larger than those of the other compounds, indicating that $KScS_2$, KYS_2 and $RbScS_2$ are having more resistance to volume change under applied pressure, and for reversible deformation upon shear and uniaxial stress. However, for all the studied materials, the calculated Poisson's ratio υ is about 0.22, explaining the ionic character of the these compounds[60]. Besides, Pugh ratio is the measure of material ductility based on the calculated parameters (bulk B, and shear G modulus)[61]. According to the empirical criterion of Pugh[62], a solid is brittle if the B/G ratio is less than 1.75, otherwise the material behaves in a ductile manner. From the table the B/G ratio of $KScS_2$, KYS_2, $KLaS_2$, $KLuS_2$, $RbScS_2$ and $RbLuS_2$ are less than 1.75, which confirms that these materials are brittle in nature.

Elastic anisotropy is one of the most important materials properties, which reflects the interatomic bonding character in the different crystallographic directions. However, an appropriate description of the elastic anisotropy, allow for exploring micro-cracks and assess mechanical durability of material as well as helping to improve the mechanical properties of solids [63, 64]. In the present work, to investigate the elastic anisotropy of $KScS_2$, KYS_2, $KLaS_2$, $KLuS_2$, $RbScS_2$ and $RbLuS_2$, we have used the following approaches;

1. The universal anisotropy index A^U. For a completely isotropic crystal, A^U is equal to 0, while any deviation from 0 shows the degree of elastic anisotropy possessed by a crystal. The universal anisotropy index A^U can be evaluated using the following equation[65]:

$$A^U = \frac{5G_V}{GR} + \frac{B_V}{B_R} - 6 \qquad \text{(III.2)}$$

The calculated values of the universal anisotropy index A^U at 0 GPa for $KScS_2$, KYS_2, $KLaS_2$, $KLuS_2$, $RbScS_2$ and $RbLuS_2$ are presented in ***Table III.4***. Our calculated results reveal that the studied materials are having certain degree of elastic anisotropy. The elastic anisotropy is increasing from $KScS_2 \rightarrow RbScS_2 \rightarrow KLuS_2 \rightarrow RbLuS_2 \rightarrow KYS_2 \rightarrow KLaS_2$ with increasing the atomic size of the constituent atoms for each compound.

Table III.4: *Calculated Elastic anisotropic indexes (universal anisotropy index A^U, elastic anisotropy in compressibility (A_B) and shear (A_G) of $KScS_2$, KYS_2, $KLaS_2$, $KLuS_2$, $RbScS_2$ and $RbLuS_2$ materials, using GGA and LDA.*

Compound	method	A^U	A_B(%)	A_G(%)
$KScS_2$	**GGA**	0.455	1.026	4.34
	LDA	0.642	0.036	6.03
KYS_2	**GGA**	0.527	0.58	4.91
	LDA	0.662	0.27	6.17
$KLaS_2$	**GGA**	0.617	1.69	5.51
	LDA	0.612	1.29	5.52
$KLuS_2$	**GGA**	0.517	0.61	4.662
	LDA	0.826	0.24	7.602
$RbScS_2$	**GGA**	0.475	0	4.53
	LDA	0.722	0.18	6.67
$RbLuS_2$	**GGA**	0.525	0.035	4.99
	LDA	0.861	0.021	7.91

2. Compressible (A_B) and shear (A_G) anisotropies[66, 67]:

$$A_B = \frac{B_v - B_R}{B_v + B_R} \quad \text{(III.3)}$$

$$A_G = \frac{G_v - G_R}{G_v + G_R} \quad \text{(III.4)}$$

$A_B = 0\ \%$ and $A_G = 0\ \%$ means isotropic material, any deviation from 0 % indicating the degree of anisotropy. Firstly, from **table III.4**, the calculated anisotropy indexes (A_B) and (A_G) show that the studied materials are anisotropic in shear much more than in compressibility.

III.5 Electronic properties

As we have seen previously, in periodic systems, the energy of a band varies as a function of k. The energy maximum of the valence band (VBM) and the minimum of the conduction band (CBM) of each band are generally found on the points and axes of high symmetry of the reciprocal lattice. The electronic band structures of $KScS_2$, KYS_2, $KLaS_2$, $KLuS_2$, $RbScS_2$ and $RbLuS_2$ materials have been determined using three different functionals, LDA (CA-PZ), GGA (PBE) and B3LYP. Due to the similarity, in ***figure III.3***, only the computed band structures of $KScS_2$ using the three different functionals, LDA (CA-PZ), GGA (PBE) and B3LYP along the high symmetric lines in the first Brillouin zone (***Figure III.2***) are presented.

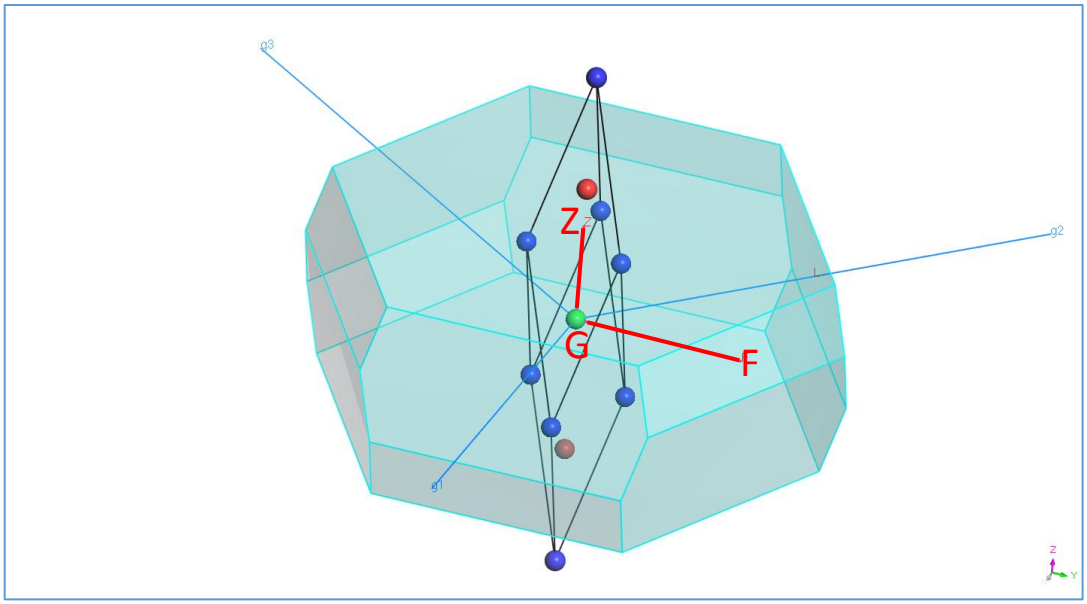

Figure III.2: *Brillouin Zone of primitive cell of ABS_2 with rhombohedral structure (space group R-3m number; 166)*

It is apparent that no overlap between the valence and conduction bands around Fermi level, which is taken as zero-energy. The valence band maximum is situated at the *Γ* point, center of the Brillouin zone, while the conduction band minimum is located at the *F* point, this allows us to classify the considered compounds as indirect band gap semiconductors. From **figure III.3** we can observed that the calculated band structures using LDA, GGA-PBE and B3LYP are very similar in general shape, except the width of the band gap.

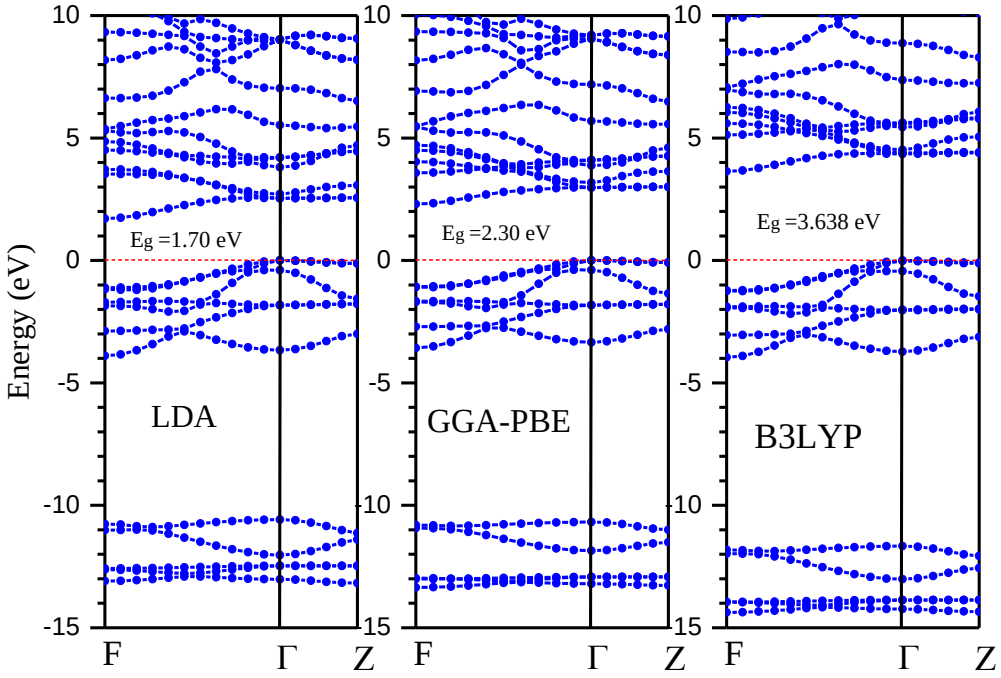

Figure III.3: *The calculated band structures of $KScS_2$ using LDA, GGA-PBE and B3LYP functionals.*

The calculated band gap values of $KScS_2$, KYS_2, $KLaS_2$, $KLuS_2$, $RbScS_2$ and $RbLuS_2$ materials using three different functionals along with the available theoretical and experimental data are illustrates in **table III.5**. As a result, both LDA (GGA) considerably underestimate the electronic band gap energy as 50-56 % (40-45 %), respectively. While the band gap values calculated by B3LYP functional are in good agreement with experimental results, Except for $RbLuS_2$, it seems that B3LYP did not give good results where the underestimation is 31 %. Furthermore, from **table III.5** we can see that our B3LYP results is much better than the other available theoretical one.

Table III.5: *the calculate band gap of $KScS_2$, KYS_2, $KLaS_2$, $KLuS_2$, $RbScS_2$ and $RbLuS_2$ using LDA, GAA-PBE AND B3LYP together with the available theoretical and experimental.*

	LDA	GGA(PBE)	B3LYP	Theoretical	Expérimental
KYS_2	1.859	2.276	3.848	3.37[a]	4.01[c]
$KLaS_2$	1.86	2.186	3.815	-	3.82[c]
$KScS_2$	1.710	2.30	3.638	2.89[a]	-
$KLuS_2$	2.001	2.415	3.323	2.39[b]	4.03[c]
$RbScS_2$	1.632	2.214	3.520	2.88[a]	-
$RbLuS_2$	1.899	2.334	2.725	-	4.00[c]

[a]:[31] [b]:[32] [c]:[30]

Due to the similarity between the calculated total density of states (TDOS) and partial density of states (PDOS) of the studied materials, only the results of $KScS_2$ is presented in **Figure III. (4):** in the energy interval between -15 and 15 eV employing LDA, GGA-PBE and B3LYP functional. One can clearly see that the K and Rb states for these compounds make almost no contribution around the Fermi level. Therefore, the electronic properties of $KScS_2$, KYS_2, $KLaS_2$, $KLuS_2$, $RbScS_2$ and $RbLuS_2$ are mainly determined by the $[BS_6]$ layers. The DOS diagrams are relatively similar, indicating the resemblance in chemical bonding.

The valance band of the considered compounds can be mainly divided into three main regions, the lower region (a), which is centered almost at -14 eV, -13.7 eV, -13.4eV, -13.7 eV, -12.3, and -12 eV for $KScS_2$, KYS_2, $KLaS_2$, $KLuS_2$, $RbScS_2$ and $RbLuS_2$, respectively (using B3LYP), is mainly originated from K-*p* (Rb-*p*) states. The second region (b) of $KScS_2$, KYS_2, $KLaS_2$, $KLuS_2$, $RbScS_2$ and $RbLuS_2$, which is centered at nearly -11.9 eV, -11.6 eV, -11.27 eV, -11.8 eV, -11.1 eV, and -10.5 eV, respectively, is composed of the *S-3s* states. Finally, the region (c) which below the fermi level E_F of ABS_2 consists *S-3p* with small contribution from *B-d* states. As for the bottom of the conduction band is mainly composed of *B-d* states with a weak contribution of *S-p*.

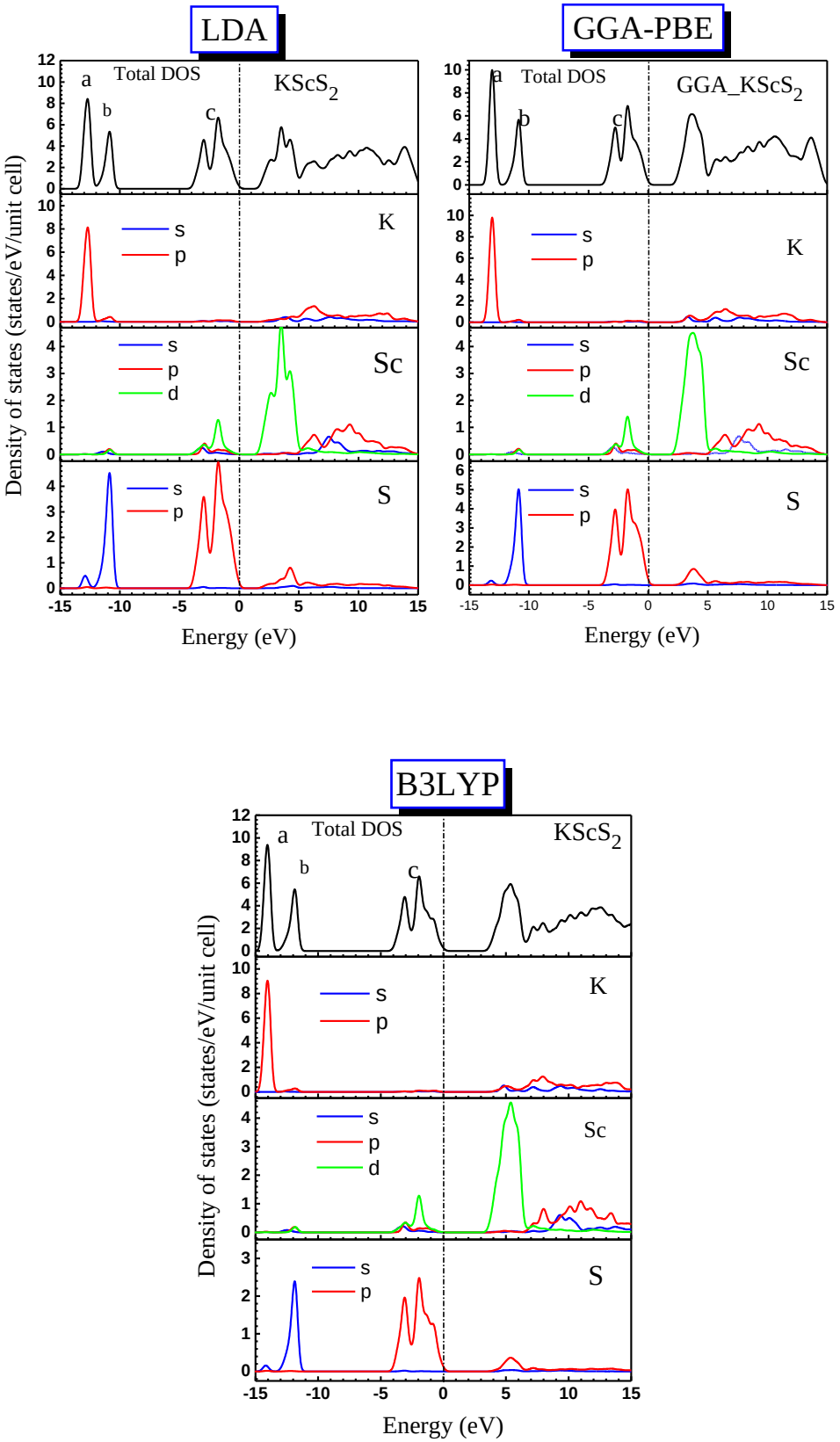

Figure III.4: *Total density of states (TDOS) and partial density of states (PDOS) of the $KScS_2$ compounds using LDA, GGA-PBE and B3LYP functionals.*

III.5.1 Mulliken charge population analysis:

Mulliken population analysis method [68] is an essential aspect to understand the bonding behavior of the crystal. Thus, we have calculated the charge transfers and bond populations via Mulliken population analysis of $KScS_2$, KYS_2, $KLaS_2$, $KLuS_2$, $RbScS_2$ and $RbLuS_2$ crystals using two different functional GGA-PBE and LDA. The obtained results are summarized in **table III.6**. The charge transfers are from $A = K$ or Rb and $B = Sc, Y, La$ or Lu atoms to S atom for all considered compounds. Based on the results in **table III.6** the effective valence state of $KScS_2$, KYS_2, $KLaS_2$, $KLuS_2$, $RbScS_2$ and $RbLuS_2$ materials using GGA-PBE (LDA) are $K^{0.70}Sc^{0.59}(S^{-0.64})_2$, $K^{0.74}Y^{0.58}(S^{-0.66})_2$,$K^{0.66}La^{0.81}(S^{-0.74})_2$, $K^{0.70}Lu^{0.44}(S^{-0.57})_2$, $Rb^{0.74}Sc^{0.57}(S^{-0.65})_2$, and $Rb^{0.77}Lu^{0.38}(S^{-0.57})_2$. While, LDA suggest the following effective valence state; $K^{0.73}Sc^{0.55}(S^{-0.64})_2$, $K^{0.73}Y^{0.54}(S^{-0.64})_2$, $K^{0.66}La^{0.75}(S^{-0.70})_2$, $K^{0.71}Lu^{0.40}(S^{-0.56})_2$, $Rb^{0.78}Sc^{0.51}(S^{-0.65})_2$, and $Rb^{0.78}Lu^{0.33}(S^{-0.56})_2$.

Table III.6: *Calculated Mullikan charges (in electrons), bond lengths (in Å) and bond populations for the $KScS_2$, KYS_2, $KLaS_2$, $KLuS_2$, $RbScS_2$ and $RbLuS_2$ compounds, using GGA-PBE and LDA functionals.*

Compound	Atom	Charge(e)		Bond	population	
		GGA	LDA		GGA	LDA
$KScS_2$	K	0.70	0.73	K–S	0.15	0.10
	Sc	0.59	0.55	Sc–S	1.30	1.34
	S	-0.64	-0.64	–	–	–
KYS_2	K	0.74	0.73	K–S	0.12	0.08
	Y	0.58	0.54	Y–S	1.38	1.42
	S	-0.66	-0.64	–	–	–
$KLaS_2$	K	0.66	0.66	K–S	0.21	0.18
	La	0.81	0.75	La–S	1.17	1.20
	S	-0.74	-0.70	–	–	–
$KLuS_2$	K	0.70	0.71	K–S	0.15	0.11
	Lu	0.44	0.40	Lu–S	1.35	1.137
	S	-0.57	-0.56		–	–
$RbScS_2$	Rb	0.74	0.78	Rb–S	0.08	0.01
	Sc	0.57	0.51	Sc–S	1.33	1.37
	S	-0.65	-0.65	–	–	–
$RbLuS_2$	Rb	0.77	0.78	Rb–S	0.07	0.01
	Lu	0.38	0.33	Lu–S	1.40	1.43
	S	-0.57	-0.56	–	–	–

The overlap population may be used to assess to identify the nature of bond character (covalent or ionic). Generally, the zero value of the bond population indicates an ideal ionic

bond while the high positive value implies a high degree of covalency of the bond [69]. The obtained values of the bond population demonstrated in **table III.6** corroborates the ionic-covalent mixed bond of *K–S* and *Rb–S* bonds for all compounds, whereas *B–S* bonds are having more covalent character. This results are similar to that fond in the isostructural materials $RbXSe_2$[70].

III.6 Optical properties

The complex dielectric function: $\varepsilon(\omega) = \varepsilon_1(\omega) + i\varepsilon_2(\omega)$ describes the optical properties of materials, it represents the response of material to an electromagnetic wave. In order to correct the underestimated band gap using LDA and GGA functionals, we have applied the hybrid functional B3LYP to calculate the optical properties. The real $\varepsilon_1(\omega)$, and the imaginary $\varepsilon_2(\omega)$ parts of the dielectric function $\varepsilon(\omega)$ for incident light polarized along the main crystallographic directions [100], and [001] are plotted in **Figure III.5**. Due to the absence of experimental results and no other theoretical work have been reported till now, to the best of our knowledge, our findings may serve for a reference for future works on these materials.

One of the observations is that the $KScS_2$ and $RbScS_2$ are having similar behavior of the dielectric function with small shift as result of the difference between their band gaps Eg (**Table III.5**). Furthermore, $KLuS_2$ and $RbLuS_2$ also have similar appearance of the dielectric function. Thus, here the alkali metal has no effect on the optical spectrum shape. However, we can observe remarkable differences between the real part $\varepsilon_1(\omega)$ and the imaginary part $\varepsilon_2(\omega)$ of the dielectric function $\varepsilon(\omega)$ corresponding to the main crystallographic directions [100] and [001], where both real and imaginary parts along z-direction shift to the high energy for all studied compounds. Leading to a significant optical anisotropy for these materials. We can see that the imaginary part spectrum of KYS_2, $KLaS_2$, $KLuS_2$ and $RbLuS_2$ exhibits two main peaks of absorption in the energy range approximately from 3.8 to 10 eV. While only one large peak is observed for $KScS_2$ and $RbScS_2$. With the aid of the density of states diagrams **Figure III.4**, we can assign the origin peaks of the imaginary part $\varepsilon_2(\omega)$ of the dielectric function to the electronic transitions between occupied *S-p* and unoccupied *B-d*, *p* states.

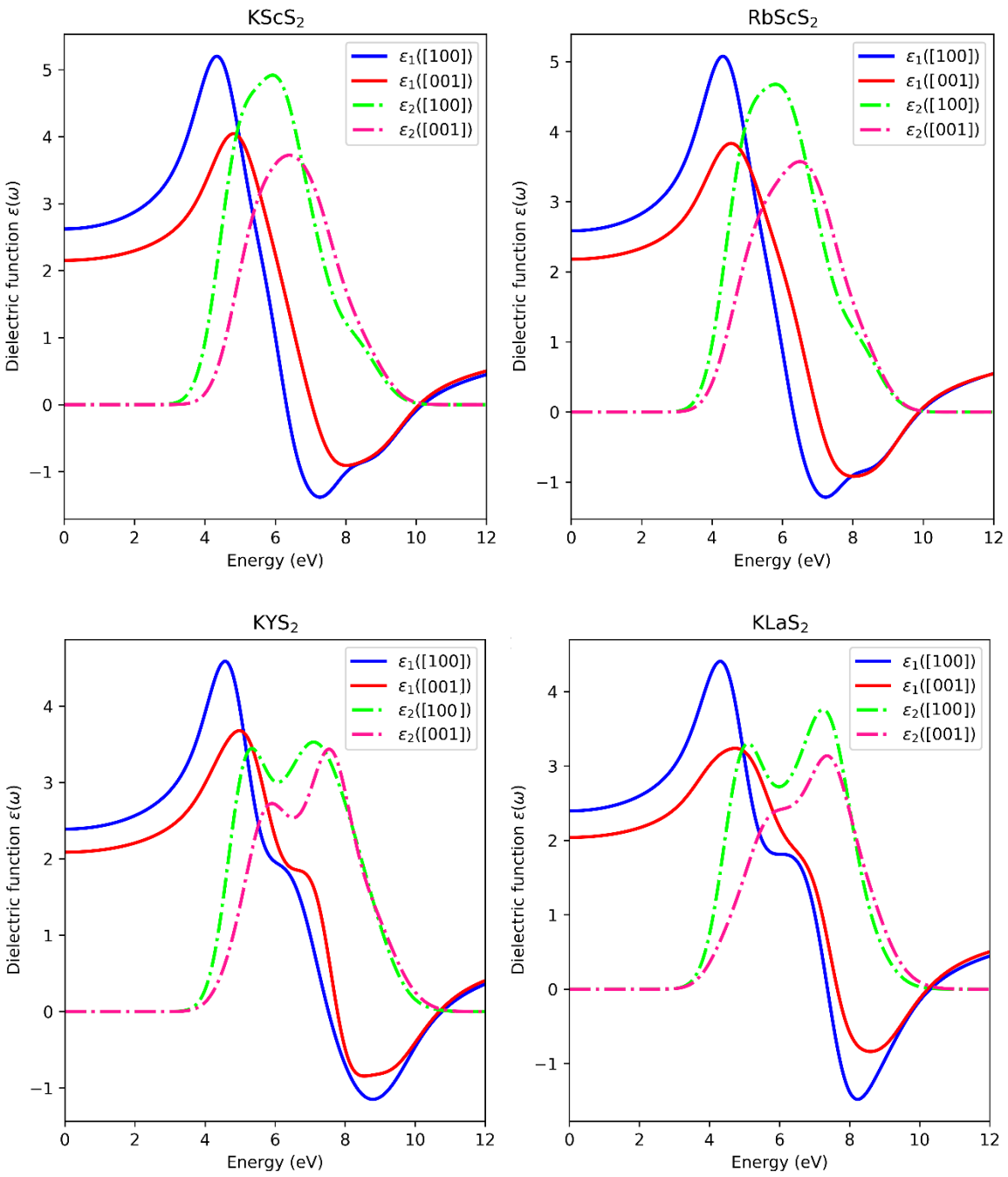
KScS2
RbScS2
KYS2
KLaS2
ε1([100])
ε1([001])
ε2([100])
ε2([001])
Dielectric function ε(ω)
Energy (eV)

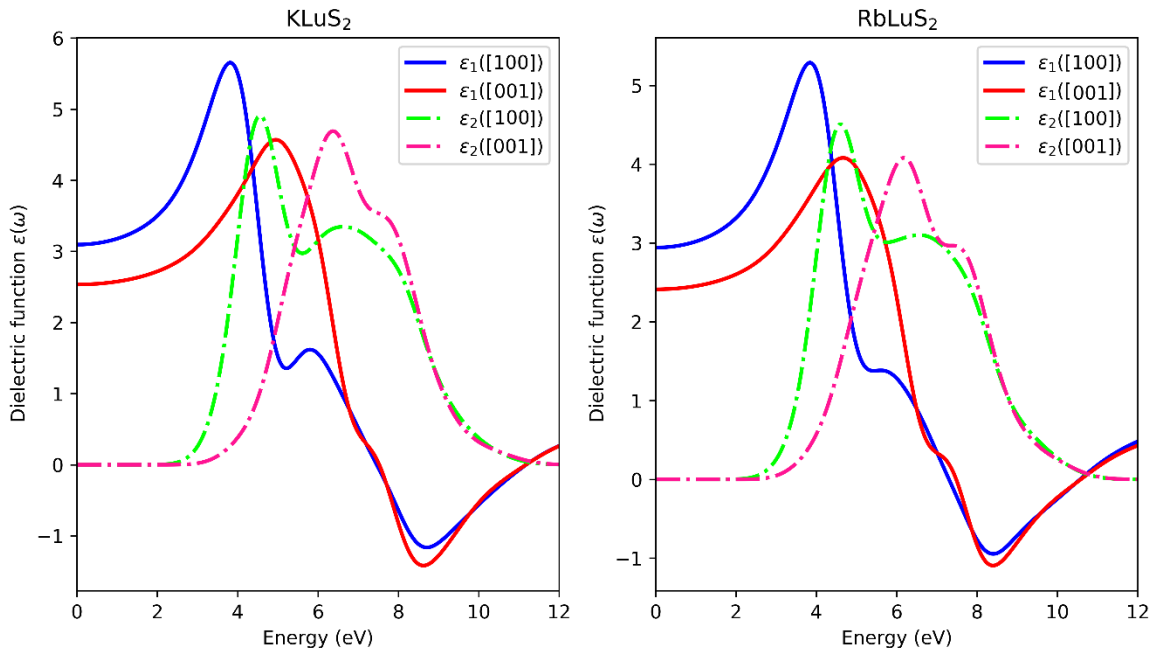

Figure III.5: *Real and imaginary parts of the dielectric function for incident radiation with electric field polarized parallel to the three different crystal directions, [100] (or [010] and [001]), for the ABS_2 compounds, using B3LYP functional.*

From **Figure. III.5**, we can see that our compounds exhibit similar behavior as metallic refractance in the range energy $\varepsilon_1(\omega) < 0$. The most important quantity of the real part is the zero-frequency limit $\varepsilon_1(0)$, the so-called also the static dielectric constant, which can define the dielectric constant for the materials at 0 eV. Our numbered static dielectric constant $\varepsilon_1(0)$ for incident radiations polarized along the [100] (or [010] and [001]) directions are presented in **table III.7**.

The reflectivity spectrum of the studied materials, $R(\omega)$ is plotted as a function of wavelength in **Figure. III.6**. Firstly, for all compounds, $R(\omega)$ along the [100] direction remains dominant throughout the spectrum.

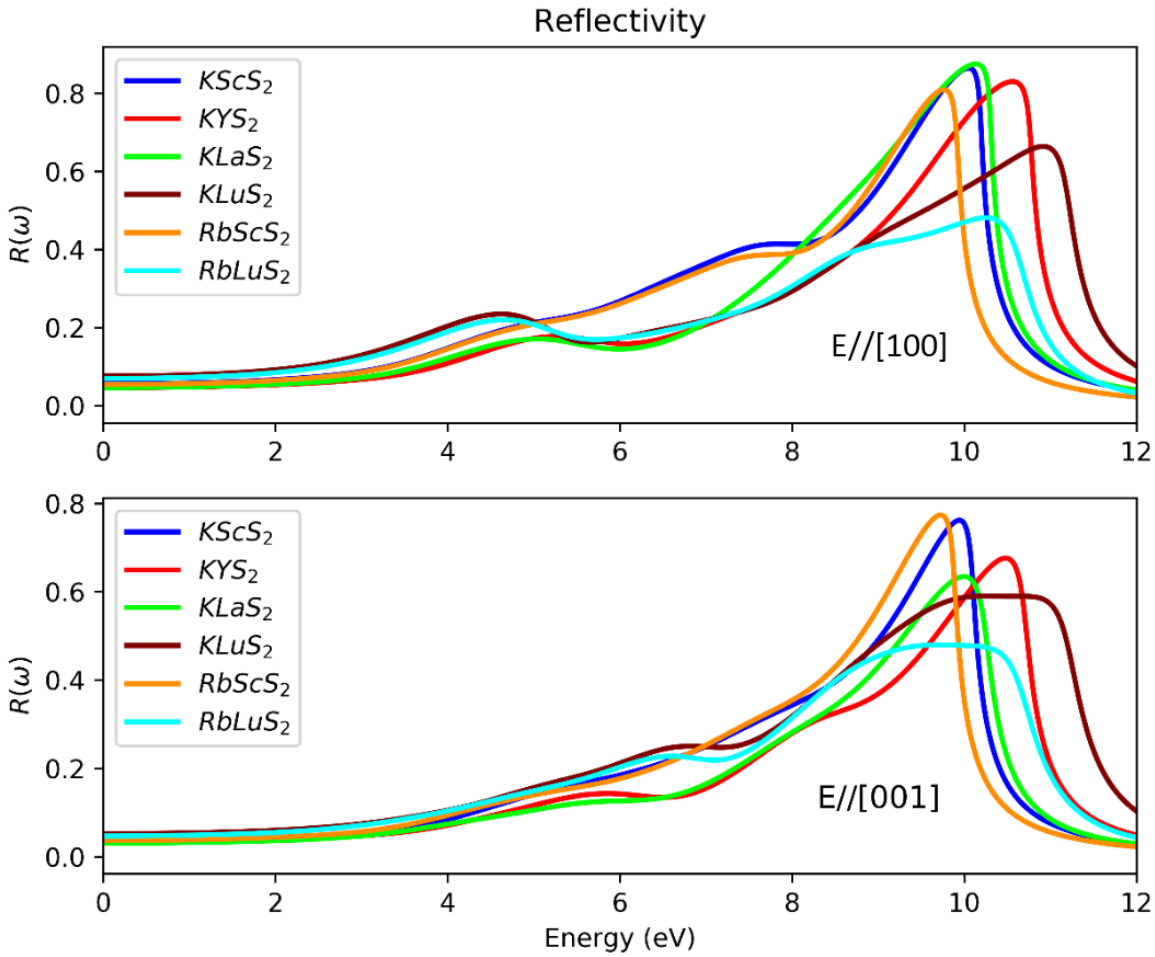

Figure III.6 *The calculated reflectivity $R(\omega)$ spectra for incident radiations polarized along the [100] or ([010] and [001]) crystallographic directions for ABS_2, using B3LYP functional.*

The reflectivity value at the zero frequency limits $R(0)$ of $KScS_2$, KYS_2, $KLaS_2$, $KLuS_2$, $RbScS_2$ and $RbLuS_2$ is equal to 5.59 % (3.59 %) 4.6 % (3.31 %) 4.62 % (3.11 %) 7.5 % (5.22 %) 5.43 % (03.7 %) 6.94 % (4.69 %) for $E_{[100]}$ ($E_{[001]}$), respectively. These materials, keep their static value almost in the infrared and visible region. Then, the reflectivity starts to increase from $R(0)$ with the increasing photon energy to attain its maximal value for $E_{[100]}$ ($E_{[001]}$) of about 86.5 % (76 %) at 10 eV (9.97 eV) for $KScS_2$, 83% (67%) at 10.55 eV (10.44eV) for KYS_2, 87.5% (63.47%) at 10.11 eV (9.99 eV) for $KLaS_2$, 66 % (55 %) at 11 eV (10 eV) for $KLuS_2$, 81% (77.4 %) at 9.75 eV (9.72 eV) for $RbScS_2$, and 48.1 % (48 %) at 10.3 eV (9.72 eV) for $RbLuS_2$. Thereafter, the reflectivity $R(\omega)$ decreases to reach its minimum level at about 12 eV. We can notice that in IR and visible regions the reflectivity increases along of $KLaS_2 \rightarrow KYS_2$, $KScS_2 \rightarrow RbScS_2 \rightarrow RbLuS_2 \rightarrow KLuS_2$.

The absorption coefficients $\alpha(\omega)$ of the two compounds are presented in **Figure III.7** It can be observed that for all compounds the absorption edge along [001] direction is larger than along [100] and more noticeable in $KLuS_2$ and $RbLuS_2$. Also, we can see that $KScS_2$ with $RbScS_2$ and $KLuS_2$ with $RbLuS_2$ have similar absorption spectrum with almost the same absorption edge. On the other hand, the studied compounds are having a wide absorption range and the larger absorption was observed for $KLuS_2$ along [100] direction in the energy range from 3.08 to 11.4 eV, which suggests that these compounds are strongly absorbent of light in the ultraviolet region.

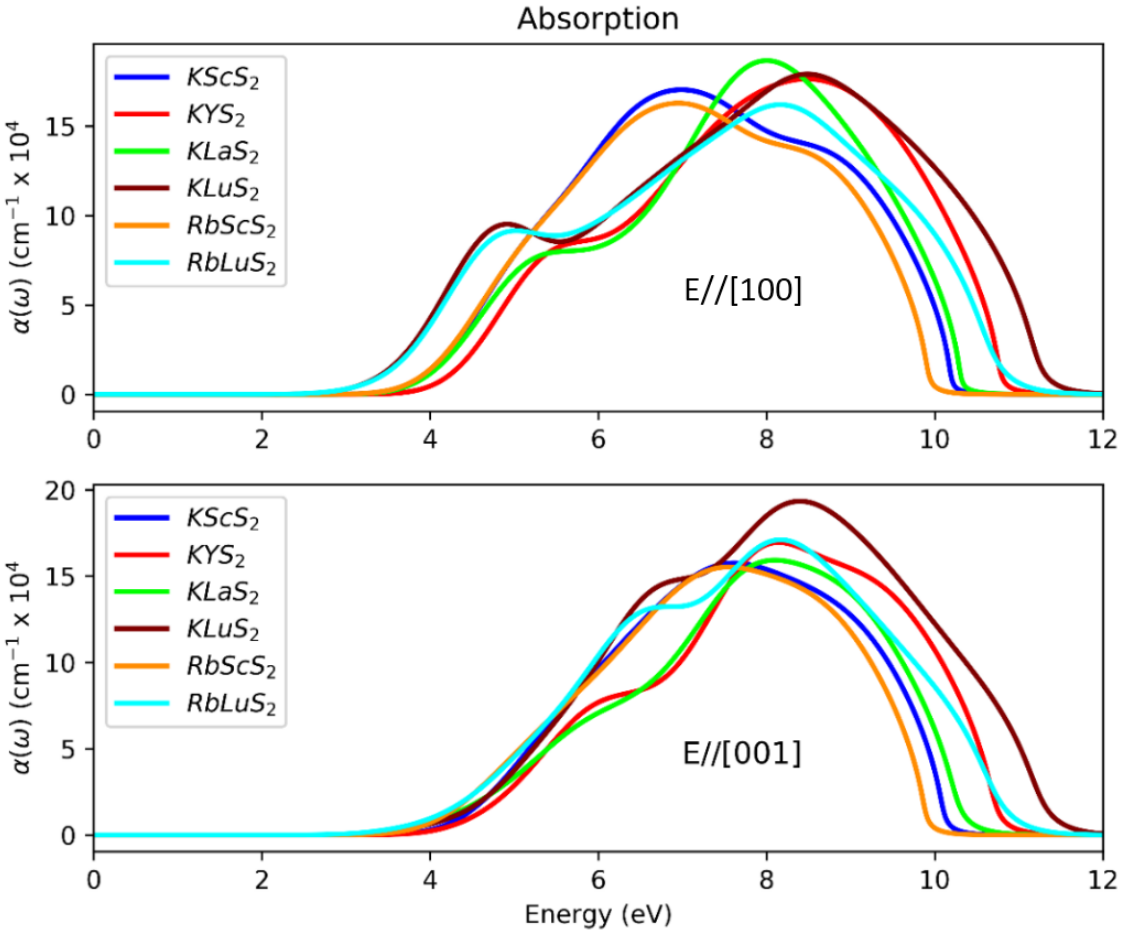

Figure III.7 *The calculated absorption coefficient $\alpha(\omega)$ for incident radiations polarized along the [100], or ([010]) and [100]) crystallographic directions for ABS_2, using B3LYP functional.*

From **Figures III (6,7),** we can observe that the reflectivity and absorption spectra of $KScS_2$, KYS_2, $KLaS_2$, $KLuS_2$, $RbScS_2$ and $RbLuS_2$ are very low in the infrared and visible regions. Consequently, these materials are transparent in these two regions.

Additionally, we can quantify the static optical anisotropy of $KScS_2$, KYS_2, $KLaS_2$, $KLuS_2$, $RbScS_2$ and $RbLuS_2$, by using anisotropy rate A_{OPT} [71-73]. Which is defined as follow:

$$A_{OPT} = \left[\frac{\varepsilon_1(0)_{dir}}{\varepsilon_1(0)_{poly}}, \frac{n(0)_{dir}}{n(0)_{poly}}\right] \quad \text{(III.5)}$$

$$n(0) = \sqrt{\varepsilon(0)} \quad \text{(III.6)}$$

Where, $\varepsilon_1(0)_{dir}$ and $n(0)_{dir}$ represent the directional value of $\varepsilon_1(0)$ and $n(0)$ in [100] and [001] directions. While, $\varepsilon_1(0)_{poly}$ and $n(0)_{poly}$ are the polycrystalline values of $\varepsilon_1(0)$ and $n(0)$, respectively. Calculated values of anisotropy rate A_{OPT} for all the studied materials are presented in **table 7**. We should note that for a completely isotropic material, anisotropy rate A_{OPT} must be equal to 1. Any deviation from 1 indicates a degree of optical anisotropy. As we can see from table 7, the A_{OPT} of all considered compounds deviate from 1.

Table III.7: *Calculated $\varepsilon_1(0)$ and $n(0)$ in polycrystalline and [100] (or [010] and [001] principal optical axes and anisotropy rate A_{OPT} of ABS_2*

		$\varepsilon_1(0)$	$n_1(0)$	A_{OPT}
$KScS_2$	**Poly**	2.46	1.57	
	100	2.62	1.62	[1.065, 1.032]
	001	2.15	1.47	[0.874, 0.936]
KYS_2	**Poly**	2.284	1.511	
	100	2.385	1.544	[1.044, 1.022]
	001	2.083	1.443	[0.912, 0.955]
$KLaS_2$	**Poly**	2.273	1.508	
	100	2.391	1.546	[1.052, 1.025]
	001	2.036	1.427	[0.896, 0.946]
$KLuS_2$	**Poly**	2.91	1.71	
	100	3.1	1.76	[1.065, 1.029]
	001	2.53	1.59	[0.869, 0.930]
$RbScS_2$	**Poly**	2.45	1.57	
	100	2.58	1.61	[1.053, 1.025]
	001	2.18	1.48	[0.890, 0.943]
$RbLuS_2$	**Poly**	2.77	1.66	
	100	2.94	1.72	[1.061, 1.036]
	001	2.41	1.55	[0.870, 0.934]

In addition, the studied materials have a wide band gap **table III.5**. And, they characterized by a very low reflectivity of less than 5 % along with all the main crystallography directions as well as they did not show any absorption of light in the entire

infrared and visible regions. Indicating the high transparency of $KScS_2$, KYS_2, $KLaS_2$, $KLuS_2$, $RbScS_2$ and $RbLuS_2$ in the infrared and visible regions, which makes them potential candidates for many of transparent application, as transparent window materials, transparent conductors, buffer layers for solar cells, liquid crystal displays, thin film-based coating application. On the other hand, the maximum reflectivity located in the ultraviolet region, which implies that it can be used as shield for ultraviolet radiation in optical devices.

III.7 Thermodynamic properties

In order to calculate the thermodynamic properties of the ABS_2 materials considered in this thesis, we have used GIBBS2 code [74], this code uses the quasi-harmonic Debye model. The starting point for the calculation of thermodynamic properties using GIBBS2 is a table of total energy data of the system as a function of the volume E (V). These data can be obtained by optimizing the crystal geometry for different pressure values (positive and negative), then we extracted the volume V and the corresponding total energy E_{tot}. This later can be done using any ab-initio computer software (CASTEP, VASP, CRYSTAL, QUANTUMESPRESSO ...ext.). Here in this thesis, we have used CASTEP code. Once the data (energy of a solid (E) as a function of molecular volume (V)) is available, GIBBS2 will be able to build the vibrational Helmholtz free energy at any temperature (F_{vib}) and thus to find the equilibrium volume at a given temperature T and pressure P by minimizing the non-equilibrium Gibbs free energy:

$$G^*(V;p,T) = E_{stat}(V) + pV + F^*_{vib}(V,T) \quad \text{(III.7)}$$

E_{sta} is the static energy which obtained directly from the ab initio calculation, F^*_{vib} is the non-equilibrium vibrational Helmholtz free energy.

It's worth to mention that, minimizing the G^* expression requires finding the volume derivative of the non-equilibrium Helmholtz free energy F^*:

$$F^*(V;p,T) = E_{stat}(V) + F^*_{vib}(V,T) \quad \text{(III.8)}$$

Indeed, expression (III. 1) is also in the Debye model with the only difference that F^*_{vib} depends on the geometry through Debye temperature Θ_D:

$$F^*_{vib}(\Theta_D,T) = E_{stat} + nKT\left[\frac{9\Theta_D}{8T} + 3ln\left(1 - e^{-\frac{\Theta_D}{T}}\right) - D(\frac{\Theta_D}{T})\right] \quad \text{(III.9)}$$

$$\Theta_D = \frac{\hbar}{K_B}\left(6\pi^2 n_r V_r^{\frac{1}{2}}\right)^{\frac{1}{3}}\sqrt{\frac{B_{stat}}{M_r}} \quad \text{(III.10)}$$

Where: B_{stat} is the adiabatic compressibility modulus; M_r is the molecular mass.

$$B_{stat}(V_r) = V_r\left(\frac{\partial^2 E_{stat}(V_r)}{\partial V_r^2}\right) \quad \text{(III.11)}$$

Once the equilibrium volumes V(p,T) are known, the other thermodynamic properties including Entropy (*S*), Constant volume heat capacity (C_v), Constant pressure heat capacity, (C_p), Volumetric thermal expansion coefficient (α), can be compute using the following equations:

$$S = -3nK_B \ln\left(1 - e^{\frac{\Theta_D}{T}}\right) - 4nK_B D\left(\frac{\Theta_D}{T}\right) \quad \text{(III.12)}$$

$$C_v = 12nK_B \mathrm{D}\left(\frac{\Theta_D}{T}\right) - \frac{9nK_B\Theta_D/T}{e^{\frac{\Theta_D}{T}} - 1} \quad \text{(III. 13)}$$

$$C_p = C_v(1 + \gamma_{th}\alpha T) \quad \text{(III.14)}$$

$$\gamma_{th} = -\frac{V}{C_v T}\left(\frac{\partial(-TS)}{\partial V}\right)_T \quad \text{(III.15)}$$

$$\alpha = \frac{\gamma_{th} C_v}{V B_T} \quad \text{(III. 16)}$$

$$B_T = V\left(\frac{\partial^2 F}{\partial V^2}\right)_T \quad \text{(III. 17)}$$

The calculated thermodynamic properties are plotted in a wide temperature range from 0 to 1000 K. **Figure III.8** displays, the isobaric volume variation (at zero pressure) plots of $KScS_2$, KYS_2 $KLaS_2$, $KLuS_2$, $RbScS_2$, and $RbLuS_2$. From the figure, the volumes of these materials are almost invariant (slight increase is observed) for temperatures lower than 100K, and then starts to increase quasi-linearly with the increase of temperature beyond that, which can be explained by the expansion of the bond-length under the temperature augmentation. Also, we can notice that volumes of KYS_2 and $KLuS_2$ less affected by the temperature compared to the others. However, in all considered temperature range, $KScS_2$, $KLaS_2$ have the lower and the largest volume, respectively.

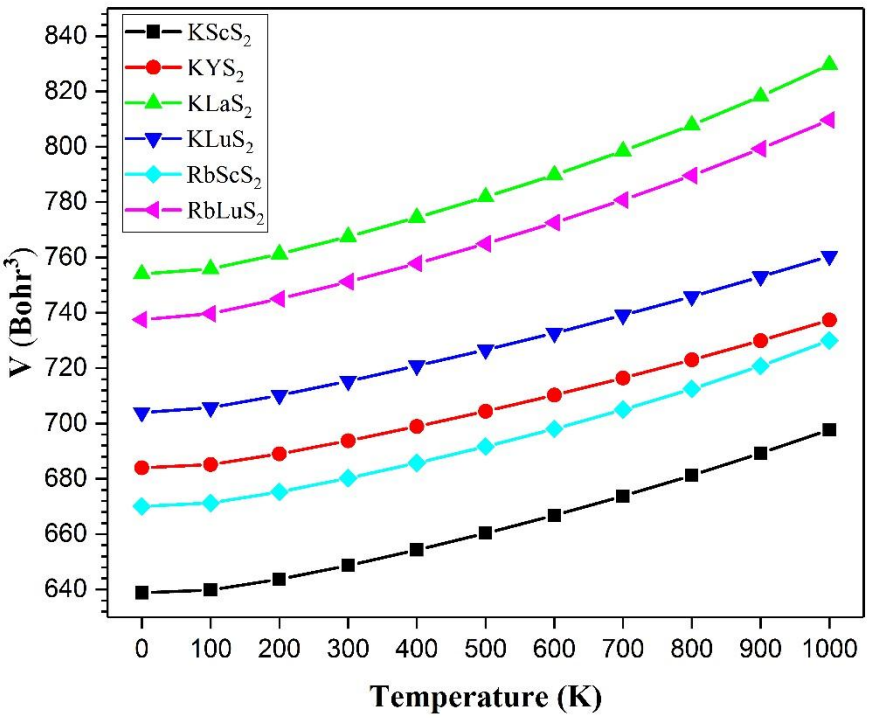

Figure III.8. *Volume versus pressure plots $KScS_2$, KYS_2 $KLaS_2$, $KLuS_2$, $RbScS_2$, and $RbLuS_2$.*

The determined bulk modulus of $KScS_2$, KYS_2 $KLaS_2$, $KLuS_2$, $RbScS_2$, and $RbLuS_2$ are plotted in **Figure III.9** as a function of temperature. Bulk modulus *B* is practically steady for low temperatures up to 100 K, then declines directly with increasing temperature up to 1000K. Again, the bulk modulus of KYS_2 and $KLuS_2$ show less affected by the temperature. The bulk modulus value of $KLuS_2$ become larger than $RbScS_2$ and $KScS_2$ in the temperatures beyond 795 K and 930 K, respectively. Additionally, from 0 to 1000 K (exception for $KLuS_2$, $RbScS_2$ and $KScS_2$ in the case of in the temperatures beyond 795 K and 930 K), the resistance against the pressure increases along $KLaS_2 < RbLuS_2 < KLuS_2 < RbScS_2 < KScS_2 < KYS_2$. At temperature 300 K and pressure 0 GPa, the bulk modulus value of $KScS_2$, KYS_2 $KLaS_2$, $KLuS_2$, $RbScS_2$, and $RbLuS_2$ are 42.30, 42.97, 36.25, 37.83, 41.38, and 36.76, respectively.

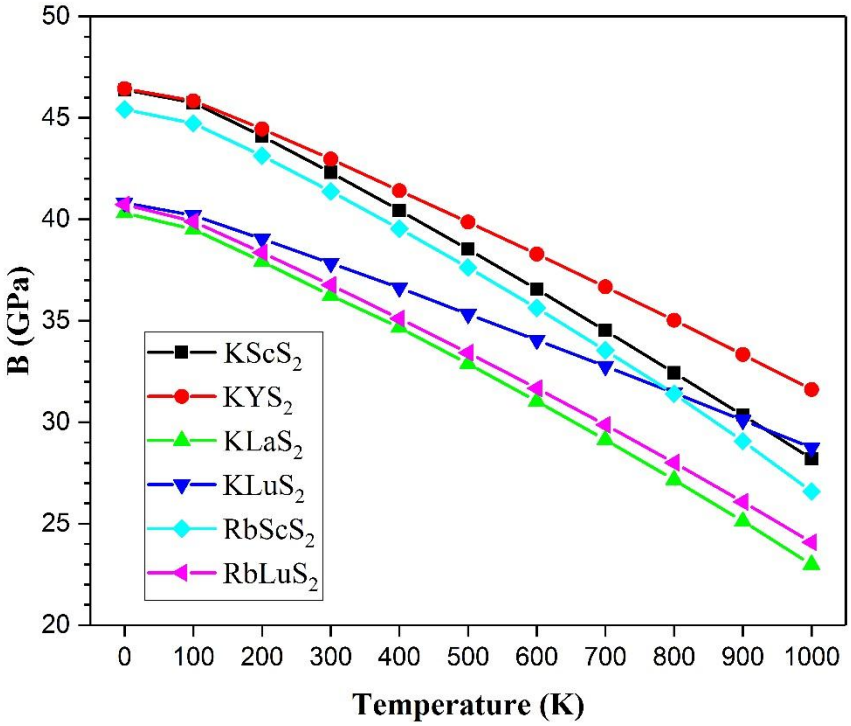

Figure III.9 *Temperature dependent computed bulk modulus of $KScS_2$, KYS_2 $KLaS_2$, $KLuS_2$, $RbScS_2$, and $RbLuS_2$.*

Figure III.10 and **Figure III.11** show the isochoric C_v and isobaric C_p heat capacities of $KScS_2$, KYS_2 $KLaS_2$, $KLuS_2$, $RbScS_2$, and $RbLuS_2$ as a function of temperature. As can be seen from the curves, in the temperature range of 0-300K, both C_v and C_p rise rapidly with temperature, after 300 K the increase rate becomes slower, where C_v of all compounds reaches its saturation value Dulong-Petit limit which is [3nR] [75], where *R* is the gas constant, and n is the number of atoms per unit cell (here n=4). Meanwhile, Cp is continuously increasing and does not amount to a constant value for all studied solids. The values of C_v (C_p) at pressure 0 GPa and temperature 300 K for $KScS_2$, KYS_2, $KLaS_2$, $KLuS_2$, $RbScS_2$, and $RbLuS_2$ are 92.93(97.85) 94.23(98.33), 95.88(101.38), 96.31(100.33), 94.45(98.92), and 96.82(102.19) J/mol.K, respectively.

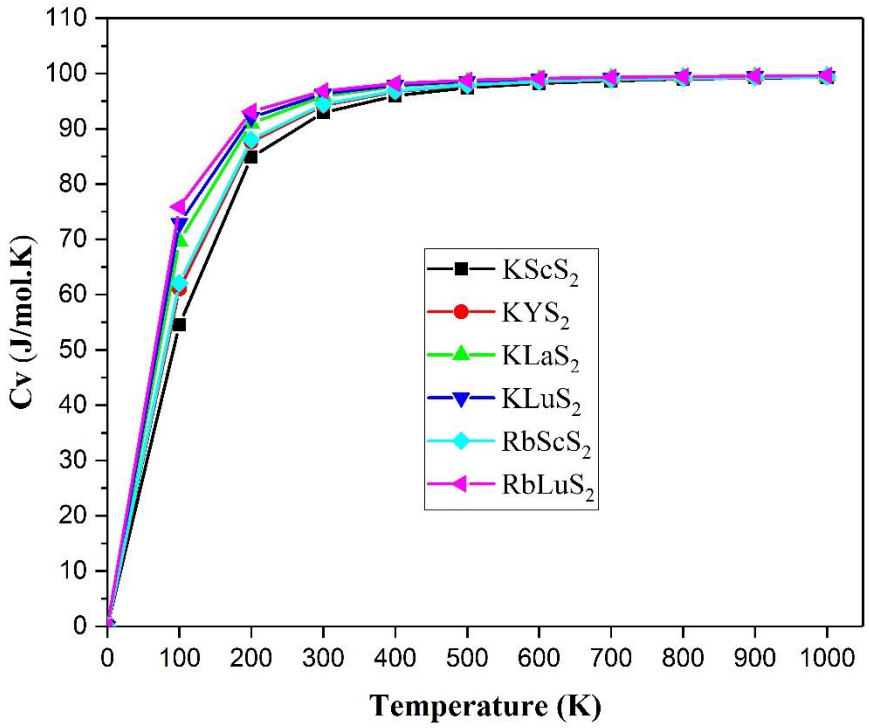

Figure III.10 *Isochoric heat capacity Cv of $KScS_2$, KYS_2 $KLaS_2$, $KLuS_2$, $RbScS_2$, and $RbLuS_2$ versus temperature T.*

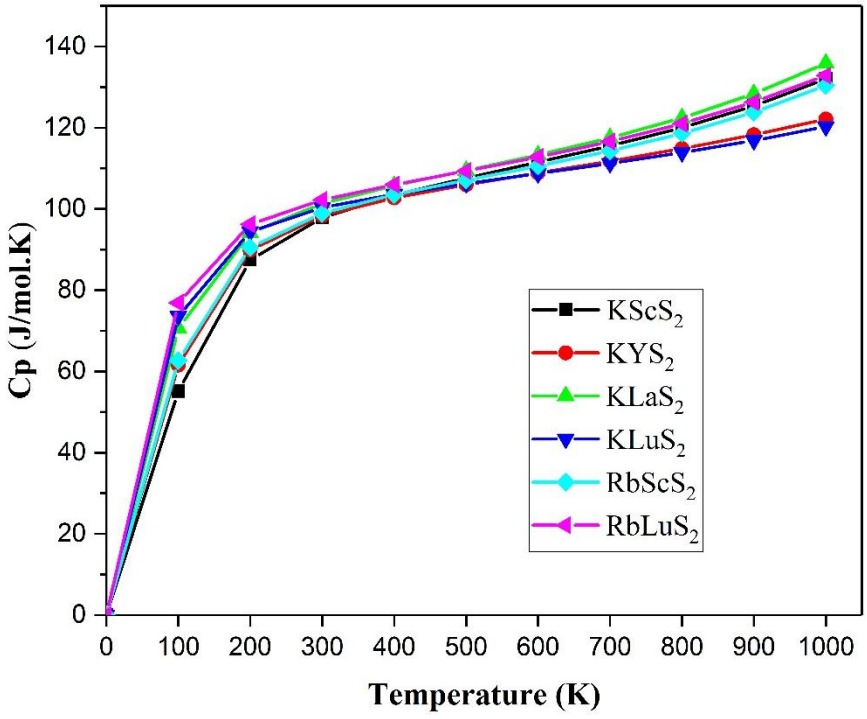

Figure III.11 Isobaric heat capacity Cp *of $KScS_2$, KYS_2 $KLaS_2$, $KLuS_2$, $RbScS_2$, and $RbLuS_2$ versus temperature T.*

The Debye temperature Θ is one of the most important parameters of thermodynamic properties, which gives important information corresponding to the chemical bond strength, thermal conductivity, and the hardness of materials. **Figure III.12** displays the Debye temperature of $KScS_2$, KYS_2 $KLaS_2$, $KLuS_2$, $RbScS_2$, and $RbLuS_2$ as a function of temperature. We can conclude that the temperature weakens the bonding strength in the case of the above-mentioned materials.

The Debye temperatures values increase along of $RbLuS_2 < KLuS_2 < KLaS_2 < RbScS_2 < KYS_2 < KScS_2$, therefore, better thermal conductivity, stronger chemical bonds and larger hardness increase in the same way $RbLuS_2 < KLuS_2 < KLaS_2 < RbScS_2 < KYS_2 < KScS_2$ [48.49,50]. The computed Debye temperature at 0 GPa and 300 K of KYS_2 and $KLaS_2$ are $KScS_2$, KYS_2 $KLaS_2$, $KLuS_2$, $RbScS_2$, and $RbLuS_2$ 360.45, 322.71, 269.27, 252.93, 316.06, and 233.22, respectively.

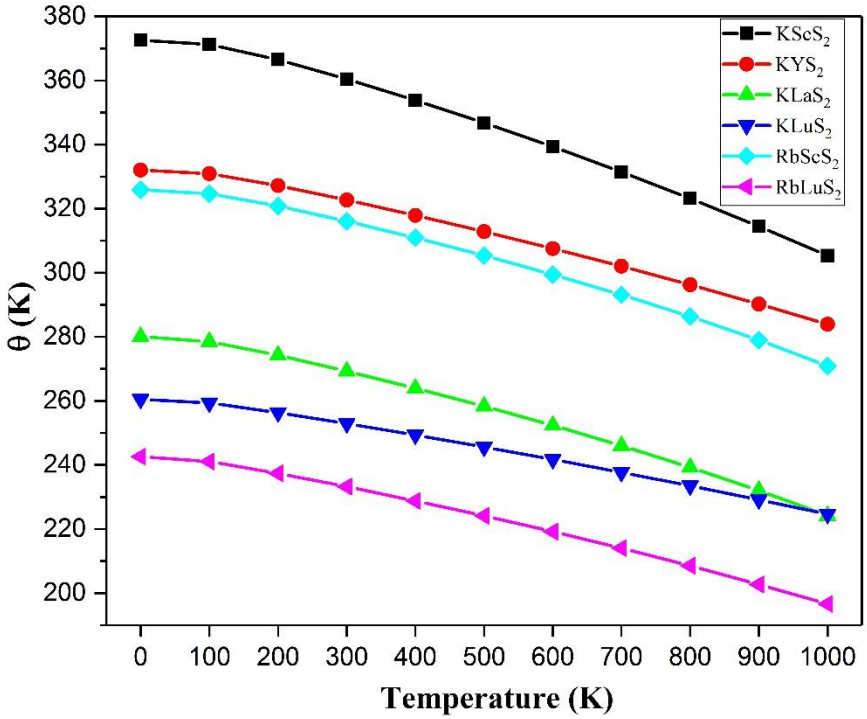

Figure III.12 *Variation of the Debye temperature of KYS_2 and $KLaS_2$ are $KScS_2$, KYS_2 $KLaS_2$, $KLuS_2$, $RbScS_2$, and $RbLuS_2$ as a function temperature.*

III.8 Conclusions

In this chapter, we have studied structural, elastic, electronic and optical properties of the ternary sulfides $KScS_2$, KYS_2, $KLaS_2$, $KLuS_2$, $RbLuS_2$, and $RbScS_2$ using first principles calculations based on density functional theory (DFT). First of all, we have found that GGA-PBE gives results better than LDA, for structural properties. The determined lattice parameters are in good agreement with the available experimental ones. The elastic constants and macroscopic elastic parameters confirm that the studied materials: mechanically stable, brittle in nature. All these solids are semiconductors with indirect band gap and B3LYP functional leads an excellent agreement compared to the experimental ones. The energy band gap E_g is found between the valence band formed by *S-3p* and B-d (B: rare earth) orbitals in the conduction band. The studied compounds demonstrate optical anisotropy, while the absorption and reflectivity spectra indicate the studied compounds are transparent in the infrared and visible regions. Therefore, these materials can be used in transparent technology. However, the calculated thermodynamic properties reveal that the considered materials less affected by temperatures lower than 100 K, while the influence is evident in temperatures greater than 100 K. The Debye temperatures values increase along of $RbLuS_2 < KLuS_2 < KLaS_2 < RbScS_2 < KYS_2 < KScS_2$, therefore, better thermal conductivity, stronger chemical bonds and larger hardness increase in the same way $RbLuS_2 < KLuS_2 < KLaS_2 < RbScS_2 < KYS_2 < KScS_2$. In absence of theoretical and experimental results, present findings can serve as predictions and guidance for future works on the considered compounds.

References:

[1] J. Tsao, S. Chowdhury, M. Hollis, D. Jena, N. Johnson, K. Jones, R. Kaplar, S. Rajan, C. Van de Walle, E. Bellotti, Ultrawide-Bandgap Semiconductors: Research Opportunities and Challenges, Advanced Electronic Materials 4(1) (2018) 1600501.

[2] C. Xie, X.T. Lu, X.W. Tong, Z.X. Zhang, F.X. Liang, L. Liang, L.B. Luo, Y.C. Wu, Recent progress in solar-blind deep-ultraviolet photodetectors based on inorganic ultrawide bandgap semiconductors, Advanced Functional Materials 29(9) (2019) 1806006.

[3] H. Xue, Q. He, G. Jian, S. Long, T. Pang, M. Liu, An overview of the ultrawide bandgap Ga 2 O 3 semiconductor-based Schottky barrier diode for power electronics application, Nanoscale research letters 13(1) (2018) 290.

[4] I. Lee, A. Kumar, K. Zeng, U. Singisetti, X. Yao, Modeling and power loss evaluation of ultra wide band gap Ga 2 O 3 device for high power applications, 2017 IEEE Energy Conversion Congress and Exposition (ECCE), IEEE, 2017, pp. 4377-4382.

[5] M. Shur, Wide band gap semiconductor technology: State-of-the-art, Solid-State Electronics 155 (2019) 65-75.

[6] D. Laks, C. Van de Walle, G. Neumark, S. Pantelides, Role of native defects in wide-band-gap semiconductors, Physical Review Letters 66(5) (1991) 648.

[7] K.A. Mengle, S. Chae, E. Kioupakis, Quasiparticle band structure and optical properties of rutile GeO2, an ultra-wide-band-gap semiconductor, Journal of Applied Physics 126(8) (2019) 085703.

[8] S. Hashimoto, K. Akita, Y. Yamamoto, M. Ueno, T. Nakamura, N. Yafune, K. Sakuno, H. Tokuda, M. Kuzuhara, K. Takeda, High carrier concentration in high Al-composition AlGaN-channnel HEMTs, physica status solidi c 9(2) (2012) 373-376.

[9] T. Razzak, H. Xue, Z. Xia, S. Hwang, A. Khan, W. Lu, S. Rajan, Ultra-wide band gap materials for high frequency applications, 2018 IEEE MTT-S International Microwave Workshop Series on Advanced Materials and Processes for RF and THz Applications (IMWS-AMP), IEEE, 2018, pp. 1-3.

[10] F. Roccaforte, P. Fiorenza, G. Greco, R.L. Nigro, F. Giannazzo, F. Iucolano, M. Saggio, Emerging trends in wide band gap semiconductors (SiC and GaN) technology for power devices, Microelectronic Engineering 187 (2018) 66-77.

[11] M. Aubert, P. Macaudiere, Rare-earth and alkali sulphide, method for preparing same and use thereof as a pigment, Google Patents, 2001.

[12] N. Matsuda, Light-emitting material, scintillator containing the light-emitting material, x-ray detector equipped with the scintillator, image display device using the light-emitting material, and light source using the light-emitting material, Google Patents, 2011.

[13] H. Lueken, W. Brüggemann, W. Bronger, J. Fleischhauer, Magnetic properties of NaCeS2 between 3.7 and 297 K, Journal of the Less Common Metals 65(1) (1979) 79-88.

[14] H. Masuda, T. Fujino, N. Sato, K. Yamada, Electrical properties of Na 2 US 3, NaGdS 2 and NaLaS 2, Materials research bulletin 34(8) (1999) 1291-1300.

[15] M. Sato, G. Adachi, J. Shiokawa, Preparation and structure of sodium rare-earth sulfides, NaLnS2 (Ln; rare earth elements), Materials Research Bulletin 19(9) (1984) 1215-1220.

[16] H. Li, W. Ding, Z. Gu, H. Li, J. Zhao, L. Fu, Preparation and infrared transmittance of NaLaS 2 ceramics, Materials Letters 156 (2015) 62-64.

[17] M. Baenitz, P. Schlender, J. Sichelschmidt, Y. Onykiienko, Z. Zangeneh, K. Ranjith, R. Sarkar, L. Hozoi, H. Walker, J.-C. Orain, NaYbS 2: A planar spin-1 2 triangular-lattice magnet and putative spin liquid, Physical review B 98(22) (2018) 220409.

[18] Z. Zangeneh, S. Avdoshenko, J. van den Brink, L. Hozoi, Single-site magnetic anisotropy governed by interlayer cation charge imbalance in triangular-lattice A Yb X 2, Physical review B 100(17) (2019) 174436.

[19] X. Zhang, Z. Zhang, S. Yao, A. Chen, X. Zhao, Z. Zhou, An effective method to screen sodium-based layered materials for sodium ion batteries, npj Computational Materials 4(1) (2018) 1-6.

[20] Z.-M. Xu, S.-H. Bo, H. Zhu, LiCrS2 and LiMnS2 Cathodes with Extraordinary Mixed Electron–Ion Conductivities and Favorable Interfacial Compatibilities with Sulfide Electrolyte, ACS applied materials & interfaces 10(43) (2018) 36941-36953.

[21] L. Havlák, V. Jarý, M. Nikl, P. Boháček, J. Bárta, Preparation, luminescence and structural properties of RE-doped RbLaS 2 compounds, Acta Materialia 59(16) (2011) 6219-6227.

[22] V. Jarý, L. Havlák, J. Bárta, M. Nikl, Preparation, luminescence and structural properties of rare-earth-doped RbLuS2 compounds, physica status solidi (RRL)-Rapid Research Letters 6(2) (2012) 95-97.

[23] V. Jarý, L. Havlák, J. Bárta, E. Mihóková, M. Nikl, Luminescence and structural properties of RbGdS 2 compounds doped by rare earth elements, Optical Materials 35(6) (2013) 1226-1229.

[24] V. Jarý, L. Havlák, J. Bárta, E. Mihóková, M. Nikl, Optical properties of Eu 2+-doped KLuS 2 phosphor, Chemical Physics Letters 574 (2013) 61-65.

[25] V. Jarý, L. Havlák, J. Bárta, E. Mihóková, P. Průša, M. Nikl, Optical properties of Ce 3+-doped KLuS 2 phosphor, Journal of Luminescence 147 (2014) 196-201.

[26] L. Havlák, V. Jarý, M. Rejman, E. Mihóková, J. Bárta, M. Nikl, Luminescence characteristics of doubly doped KLuS 2: Eu, RE (RE= Pr, Sm, Ce), Optical Materials 41 (2015) 94-97.

[27] V. Jarý, L. Havlák, J. Bárta, M. Buryi, M. Rejman, M. Pokorný, C. Dujardin, G. Ledoux, M. Nikl, Variability of Eu2+ Emission Features in Multicomponent Alkali-Metal-Rare-Earth Sulfides, ECS Journal of Solid State Science and Technology 9(1) (2019) 016007.

[28] J. Fábry, L. Havlák, M. Dušek, P. Vaněk, J. Drahokoupil, K. Jurek, Structure determination of KLaS2, KPrS2, KEuS2, KGdS2, KLuS2, KYS2, RbYS2, NaLaS2 and crystal-chemical analysis of the group 1 and thallium (I) rare-earth sulfide series, Acta Crystallographica Section B: Structural Science, Crystal Engineering and Materials 70(2) (2014) 360-371.

[29] L. Havlak, J. Fábry, M. Henriques, M. Dušek, Structure determination of KScS2, RbScS2 and KLnS2 (Ln= Nd, Sm, Tb, Dy, Ho, Er, Tm and Yb) and crystal–chemical discussion, Acta Crystallographica Section C: Structural Chemistry 71(7) (2015) 623-630.

[30] V. Jarý, L. Havlák, J. Bárta, M. Buryi, E. Mihóková, M. Rejman, V. Laguta, M. Nikl, Optical, Structural and Paramagnetic Properties of Eu-Doped Ternary Sulfides ALnS2 (A= Na, K, Rb; Ln= La, Gd, Lu, Y), Materials 8(10) (2015) 6978-6998.

[31] J. Shi, T.F. Cerqueira, W. Cui, F. Nogueira, S. Botti, M.A. Marques, High-throughput search of ternary chalcogenides for p-type transparent electrodes, Scientific reports 7 (2017) 43179.

[32] L. He, J. Meng, J. Feng, Z. Zhang, X. Liu, H. Zhang, Insight into the Characteristics of 4f-Related Electronic Transitions for Rare-Earth-Doped KLuS2 Luminescent Materials through First-Principles Calculation, The Journal of Physical Chemistry C 124(1) (2019) 932-938.

[33] V. Jary, L. Havlák, J. Bárta, E. Mihóková, M. Nikl, Optical and Structural Properties of ${\rm RE}^{3+} $-Doped ${\rm KLnS} _ {2} $ Compounds, IEEE Transactions on Nuclear Science 61(1) (2014) 385-389.

[34] V. Jarý, L. Havlák, J. Bárta, E. Mihóková, M. Buryi, M. Nikl, ALnS 2: RE (A= K, Rb; Ln= La, Gd, Lu, Y): New optical materials family, Journal of Luminescence 170 (2016) 718-735.

[35] S.J. Clark, M.D. Segall, C.J. Pickard, P.J. Hasnip, M.I. Probert, K. Refson, M.C. Payne, First principles methods using CASTEP, Zeitschrift für Kristallographie-Crystalline Materials 220(5-6) (2005) 567-570.

[36] J.P. Perdew, K. Burke, M. Ernzerhof, Generalized gradient approximation made simple, Physical Review Letters 77(18) (1996) 3865.

[37] D.M. Ceperley, B. Alder, Ground state of the electron gas by a stochastic method, Physical review letters 45(7) (1980) 566.

[38] J.P. Perdew, A. Zunger, Self-interaction correction to density-functional approximations for many-electron systems, Physical Review B 23(10) (1981) 5048.

[39] H. Xiao, J. Tahir-Kheli, W.A. Goddard III, Accurate band gaps for semiconductors from density functional theory, The Journal of Physical Chemistry Letters 2(3) (2011) 212-217.

[40] A. Becke, AD Becke, J. Chem. Phys. 98, 5648 (1993), J. Chem. Phys. 98 (1993) 5648.

[41] N. Troullier, J.L. Martins, Efficient pseudopotentials for plane-wave calculations, Physical review B 43(3) (1991) 1993.

[42] H.J. Monkhorst, J.D. Pack, Special points for Brillouin-zone integrations, Physical Review B 13(12) (1976) 5188.

[43] V. Milman, M. Warren, Elasticity of hexagonal BeO, Journal of Physics: Condensed Matter 13(2) (2001) 241.

[44] R. Ballestracci, E. Bertaut, Étude cristallographique de sulfures de terres rares et de sodium, BULLETIN DE LA SOCIETE FRANCAISE MINERALOGIE ET DE CRISTALLOGRAPHIE 87(4) (1964) 512-+.

[45] R. Ballestracci, E. Bertaut, ETUDE CRISTALLOGRAPHIQUE DE NOUVEAUX SELENIURES DE TERRES RARES ET DE SODIUM, BULLETIN DE LA SOCIETE FRANCAISE MINERALOGIE ET DE CRISTALLOGRAPHIE 88(1) (1965) 136-+.

[46] W. Bronger, J. Eyck, K. Kruse, D. Schmitz, Ternary rubidium rare-earth sulphides: synthesis and structure, European journal of solid state and inorganic chemistry 33(2-3) (1996) 213-226.

[47] T.H. Fischer, J. Almlof, General methods for geometry and wave function optimization, The Journal of Physical Chemistry 96(24) (1992) 9768-9774.

[48] W. Bronger, J. Eyck, K. Kruse, D. Schmitz, Ternary rubidium rare-earth sulphides; synthesis and structure, Eur. J. Solid State Inorg. Chem 33 (1996) 213-226.

[49] X. Zeng, R. Peng, Y. Yu, Z. Hu, Y. Wen, L. Song, Pressure Effect on Elastic Constants and Related Properties of Ti3Al Intermetallic Compound: A First-Principles Study, Materials 11(10) (2018) 2015.

[50] P. Ravindran, L. Fast, P.A. Korzhavyi, B. Johansson, J. Wills, O. Eriksson, Density functional theory for calculation of elastic properties of orthorhombic crystals: application to TiSi 2, Journal of Applied Physics 84(9) (1998) 4891-4904.

[51] F. Mouhat, F.-X. Coudert, Necessary and sufficient elastic stability conditions in various crystal systems, Physical Review B 90(22) (2014) 224104.

[52] S. Zhu, X. Zhang, J. Chen, C. Liu, D. Li, H. Yu, F. Wang, Insight into the elastic, electronic properties, anisotropy in elasticity of Manganese Borides, Vacuum 165 (2019) 118-126.

[53] D. Qu, C. Li, L. Bao, Z. Kong, Y. Duan, Structural, electronic, and elastic properties of orthorhombic, hexagonal, and cubic Cu3Sn intermetallic compounds in Sn–Cu lead-free solder, Journal of Physics and Chemistry of Solids (2019) 109253.

[54] W. Voigt, Lehrbuch der Kristallphysik (Teubner, Leipzig, 1928), MATH Google Scholar (1908) 716.

[55] A. Reuss, Berechnung der fließgrenze von mischkristallen auf grund der plastizitätsbedingun g für einkristalle, ZAMM-Journal of Applied Mathematics and Mechanics/Zeitschrift für Angewandte Mathematik und Mechanik 9(1) (1929) 49-58.

[56] R. Hill, The elastic behaviour of a crystalline aggregate, Proceedings of the Physical Society. Section A 65(5) (1952) 349.

[57] Z.-j. Wu, E.-j. Zhao, H.-p. Xiang, X.-f. Hao, X.-j. Liu, J. Meng, Crystal structures and elastic properties of superhard Ir N 2 and Ir N 3 from first principles, Physical review B 76(5) (2007) 054115.

[58] Y. Li, C. Liu, H. Yu, F. Wang, X. Zhang, Anisotropy of the elasticity, thermal conductivity and optical parameters of Cmcm and Pmcn BiMg2VO6 ceramics, Vacuum 159 (2019) 218-227.

[59] X. Zhang, J. Chen, F. Wang, X. Chen, H. Ma, D. Li, C. Liu, H. Guo, Insight into the elastic and anisotropic properties of BiMg2MO6 (M= P, As and V) ceramics from the first-principles calculations, Ceramics International 45(8) (2019) 11136-11140.

[60] J. Haines, J. Leger, G. Bocquillon, Synthesis and design of superhard materials, Annual Review of Materials Research 31(1) (2001) 1-23.

[61] M. Woodcox, J. Young, M. Smeu, Ab initio investigation of the elastic properties of bismuth-based alloys, Physical Review B 100(10) (2019) 104105.

[62] S. Pugh, XCII. Relations between the elastic moduli and the plastic properties of polycrystalline pure metals, The London, Edinburgh, and Dublin Philosophical Magazine and Journal of Science 45(367) (1954) 823-843.

[63] V. Tvergaard, J.W. Hutchinson, Microcracking in ceramics induced by thermal expansion or elastic anisotropy, Journal of the American Ceramic Society 71(3) (1988) 157-166.

[64] P. Lloveras, T. Castán, M. Porta, A. Planes, A. Saxena, Influence of elastic anisotropy on structural nanoscale textures, Physical review letters 100(16) (2008) 165707.

[65] S.I. Ranganathan, M. Ostoja-Starzewski, Universal elastic anisotropy index, Physical review letters 101(5) (2008) 055504.

[66] D. Chung, W. Buessem, The elastic anisotropy of crystals, Journal of Applied Physics 38(5) (1967) 2010-2012.

[67] D. Chung, W. Buessem, F. Vahldiek, S. Mersol, Anisotropy in single crystal refractory compounds, Plenum Press, New York, 1968 p. 217 (1968).

[68] R.S. Mulliken, Electronic population analysis on LCAO–MO molecular wave functions. I, The Journal of Chemical Physics 23(10) (1955) 1833-1840.

[69] M. Segall, R. Shah, C. Pickard, M. Payne, Population analysis of plane-wave electronic structure calculations of bulk materials, Physical Review B 54(23) (1996) 16317.

[70] B. Deng, D.E. Ellis, J.A. Ibers, New layered rubidium rare-earth selenides: Syntheses, structures, physical properties, and electronic structures for RbLnSe2, Inorganic chemistry 41(22) (2002) 5716-5720.

[71] D. Cherrad, D. Maouche, M. Boudissa, M. Reffas, L. Louail, M. Maamache, K. Haddadi, Y. Medkour, Ultra soft pseudo potential investigation of fundamental physical properties of CaXO3 (X= Sn and Hf) distorted perovskites: A reference study to the perfect perovskites, Physica B: Condensed Matter 429 (2013) 95-105.

[72] D. Liu, W. Bao, Y. Duan, Predictions of phase stabilities, electronic structures and optical properties of potential superhard WB3, Ceramics International 45(3) (2019) 3341-3349.

[73] D. Liu, Y. Duan, W. Bao, Structural properties, electronic structures and optical properties of WB2 with different structures: a theoretical investigation, Ceramics International 44(10) (2018) 11438-11447.

[74] A. Otero-de-la-Roza, D. Abbasi-Pérez, V. Luaña, Gibbs2: A new version of the quasiharmonic model code. II. Models for solid-state thermodynamics, features and implementation, Computer Physics Communications 182(10) (2011) 2232-2248.

[75] A.T. Petit, Dulong, Recherches Sur quelques points importans de la theorie de la chaleur, 1819.

CHAPTER IV

ABS_2: New p-type transparent conducting materials

IV.1 Introduction

The discovery of new materials is one of the most important to enable future technological developments. Historically, new materials have been discovered by either trial-and-error processes or serendipity. Where these methods require labour-intensive and challenging experiments, with very time-consuming and high costs. However, since the advent, the density functional theory (DFT), combined with modern computing power the situation became quite different. It became possible to predict the crystal structure of many new materials without the need for experiment. Additionally, accuracy of DFT in the determination of ground-state electronic properties sensitively depend on the adopted exchange-correlation (XC). Local density approximation (LDA) and generalized gradient approximation (GGA) are the oldest and the largely used functionals, as well as the cheap computational cost. Where, hybrid functionals (PBE0, B3LYP, HSE06) are very accurate but are much more time-consuming and need computer power as well.

Combining optical transparency to visible light, high conductivity, lead to very interesting materials so-called transparent conducting materials (TCMs). Those materials are needed in a wide range of applications such as solar cell, light-emitting diode (LED), smartphones, tablets, laptops and flat panel displays [1-6]. Among various TCMs the widely studied and used are oxides (TCMs), they offer suitable properties: wide band gap and low electron effective mass [5]. The most commonly known TCOs are In_2O_3 [7, 8], SnO_2 [9, 10], ZnO [11-13], $BaSnO_3$ [14, 15], and Ga_2O_3. [16, 17]. The commercially and widely used TCOs are n-type materials. Although some oxides (e.g., $CuAlO_2$,SnO, NiO, and $LaCrO_3$ [6, 18]) have been suggested as p-type TCOs, their materials properties are poor and stay lower

performance (especially the carrier mobility) compared to n-counterparts. Lack of high-performance p-type TCMs stands in the way of many critical technological developments. the combination of high-performance p-type TCO with known n-type TCOs could be used to develop p–n heterojunctions and opening new avenues in transparent materials technology and enable the development of many new devices. in addition, p-type TCMs with wide transparency and high mobility/conductivity can be reliably applied in many optoelectronic applications (in hole-transport layers in solar cell architectures, as efficient photocathodes in water-splitting solar cells [19], or thin-film transistors [4]). Which make the development of novel p-type TCMs a very challenging field. Two requirements for p-type TCMs: **(i)** high optical transparency to the visible light (wide band gap), which described by its transparency T (from first principles, transparency T determined by the absorption coefficient α and the reflectivity R), and **(ii)** high hole mobility (low hole effective mass $\boldsymbol{m_h^*}$). Here, our search strategy to find a new p-type transparent conductor (TCMs), is to find materials with low hole effective mass and a wide bandgap (WBG).

Recently, a new appropriately normed functional with very low computational cost compared to hybrid functionals, so-called (SCAN) [20], which belongs to the meta-GGA family of functionals, was suggested. Based on the previous researches, SCAN meta-GGA has shown excellent performance. Where it has been tested for different systems and properties with improved predictive accuracy over than LDA and GGA functionals including solids [21-23], molecules [24], surfaces [25], and liquids [26-28]. Further, previous studies have revealed that SCAN functional is a better choice than PBE, LDA+U, and PBE-based for the energetics and structural parameters [22]. Gives a more accurate predicting for transition pressures [29, 30], reactions energies, structure parameters, volume and bulk modulus [31-33]. Also, SCAN showed an efficient prediction regarding the structural, energetic and electric properties for conventional perovskite ferroelectric materials [23, 34], accurate descriptions for the intermediate-range Van der Waals (VdW) interaction [25, 35, 36]. It correctly predicts that ice is less dense than water [27], which that LDA and GGAs functionals have failed to do.

In this work, based on the largely used GGA-PBE functional, the new developed SCAN meta-GGA functional and the hybrid HSE06 functional, as well as the available data in the literature, ab initio calculations are performed to investigate the crystal structure stability and physical properties of the ternary semiconductors $CsScS_2$, $CsYS_2$, and $APmS_2$ (A= Li, Na, K, Rb, Cs) with α-$NaFeO_2$ structure-type. These compounds have not yet been

synthesized and do not already appear in the large materials database like; materials project, COD, AFLOWLIB, or OQMD.

These materials belong to the large family of alkali rare-earth sulphides ABS_2 (A= alkali metal, B= rare-earth elements. These ternary materials with α-$NaFeO_2$ structure-type have received a lot of attention and intensively studied, since they are promising materials for solid state light emitting diode (LED), lighting or X-ray phosphors [37-39], as they are potential candidates for many applications such as transparent materials, Na-ion batteries, nano-pigment, p-type transparent electrodes[31, 40-43].

IV.2 Computational details

All calculations in this chapter are performed within the Vienna Ab initio Simulation Package (VASP), with PAW pseudopotentials, and two different functionals; GGA-PBE and SCAN are adopted to describe the exchange-correlation effects (see chapter II). While, screened hybrid functional (HSE06) is employed to calculate the band structures, hole effective masses and the optical properties of selected compounds since this functional reproduces accurate results for semiconductors compared with the other traditional DFT method. The PAW Li_sv, Na_pv, K_sv, Rb_sv, Cs_sv, Pm_3, Y_sv and Sc_sv potentials are used from VASP database. An energy cut-off value of 600 eV is performed for PBE and SCAN calculations, 500 for hybrid functional (HSE06). We should mention that all calculations for hybrid functional (HSE06) were carried out on the top of SCAN structures. A k-point mesh of $9 \times 9 \times 2$ is used to sample the Brillouin zone of the unit cell. For the geometry optimization, we have used the conjugate gradient algorithm (IBRION = 2) and full Relaxation (ISIF = 3) with convergence criteria of forces less than 0.001 eV/Å and energy tolerance is less than 10^{-6} eV, respectively. The Phononpy software is adopted with $2 \times 2 \times 1$ (containing 48 atoms with $4 \times 4 \times 2$ k-mesh) supercell to calculate the phonon band structure of the titled materials.

IV.3 Results and discussion

IV.3.1 Structural properties

As we have mentioned above (Chapter I.4.2), from the available data in the literature about ABS_2 materials, J. Fabry et al [44], have reported that there is a relationships (linear association) between the atomic number Z and the structural parameters including; unit-cell parameters (a, c and c/a), fractional coordinate $z(S^{2-})$, interatomic distance, and thickness of cationic layers $h(AS_6)$ and $h(BS_6)$. Where, the unit-cell parameter a, and $z(S^{2-})$ decrease

almost linearly (curve *a* is Much more sloping than $z(S^{2-})$), with increasing atomic number *Z* of the trivalent cation B^{3+}(La-Lu). While the lattice parameter *c* remains rather constant with the change of atomic number *Z* of the rare earth elements. This later lead to a quasi-linear increasing for lattice parameter ratio *c*/*a* with increasing atomic number *Z* of B^{3+}(La-Lu), an exception for Li-based compounds (**Figures I.4(a-d)**, Chapter I). These relationships between the structural properties and the number atomic *Z* of rare earth elements gave a helpful information can be used to confirm the reliability of the structural parameters of any of these compounds and can help to investigate the others. On this basis, we have deduced and extracted the structural parameter of $APmS_2$ (A= Na, K, Rb, Cs) by the second-order fitting of structural curves for the available ABS_2 materials, for the sake of comparison with our calculated results. One used unit cell in the calculations is presented in ***figure IV.1***. Here, the Wyckoff positions in this structure-type are; the alkali atoms situated at 3a position (0,0,0), the rare earth located at the 3b position (0,0,1/2), and sulphur atoms occupy the 6c position (0, 0, *z*), where *z* is the fractional coordinate.

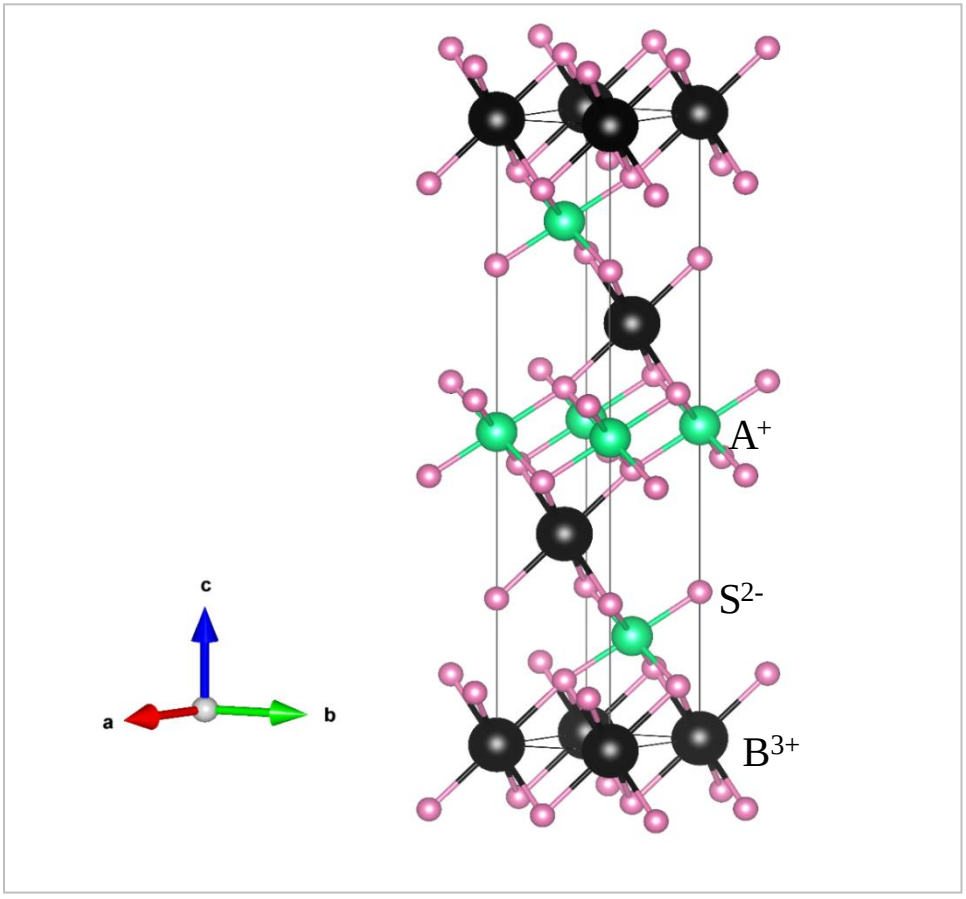

Figure IV.1. *schematic representation of one unit cell of ABS2 in the layered rhombohedral α-$NaFeO_2$-type structure contain 3 formula (3 × ABS_2)*

The obtained structural parameters of the considered materials using GGA and SCAN functional as well as the deduced one from the fitting are summarised in **table IV.1**. We can clearly see that the results obtained using SCAN functional are in excellent agreement with the expected based on the curves fitting (with deviation error between 0.019% and 0.79%), which is much better than GGA. We can conclude that SCAN functional is better than GGA to study the structural properties of these materials.

***Table IV.1**. The calculated unit-cell parameters (a and c, in Å), the lattice parameter ratio c/a, the internal parameter z(S) using GGA and SCAN functionals, along with the deduced one from the fitting [**].*

Compound	method	*a* (Å)	c (Å)	c/a	*z*(S)
LiPmS$_2$	**GGA**	4.028	18.634	4.626	0.2516
	SCAN	4.012	18.568	4.628	0.2518
NaPmS$_2$	**GGA**	4.101	20.067	4.893	0.2440
	SCAN	4.076	19.899	4.882	0.244
	[**]	4.074	20.017	4.913	-
KPmS$_2$	**GGA**	4.171	22.256	5.336	0.2349
	SCAN	4.149	21.986	5.299	0.2356
	[**]	4.143	21.900	5.288	0.2357
RbPmS$_2$	**GGA**	4.194	23.132	5.515	0.2318
	SCAN	4.168	22.951	5.506	0.2323
	[**]	4.171	22.898	5.490	0.2324
CsPmS$_2$	**GGA**	4.222	24.292	5.754	0.2282
	SCAN	4.186	24.232	5.789	0.2287
	[**]	4.182	24.042	5.749	0.2287
CsYS$_2$	**GGA**	4.107	24.16	5.882	0.227
	SCAN	4.081	24.133	5.913	0.2272
CsScS$_2$	**GGA**	3.902	23.881	6.120	0.2244
	SCAN	3.877	23.886	6.161	0.2242

[**]: *represent the deduced and extracted values of the structural parameter for APmS$_2$ (A= Na, K, Rb, Cs) by the second-order fitting of structural curves of the previous works (**figures I.4**) for the available ABS$_2$ compounds.*

***Table IV.2**. The calculated unit-cell volume (V in Å^3), interatomic distance (A^+–S and B^{3+}–S, in Å), and thickness of cationic layers ($h(A^+S_6)$ and $h(B^{3+}S_6)$, in Å).*

Compound	method	V (Å^3)	h(AS6) (Å)	h(BS6) (Å)	A-S (Å)	B-S (Å)	α (°)	β (°)
LiPmS$_2$	**GGA**	261.77	3.067	3.142	2.786	2.807	92.59	91.71
	SCAN	258.86	3.028	3.161	2.767	2.804	92.917	91.349
NaPmS$_2$	**GGA**	292.27	3.585	3.104	2.969	2.830	87.33	92.82
	SCAN	286.34	3.555	3.078	2.949	2.812	87.424	92.907
KPmS$_2$	**GGA**	335.07	4.375	3.040	3.253	2.847	79.71	94.14
	SCAN	327.86	4.298	3.030	3.218	2.834	80.272	94.093
RbPmS$_2$	**GGA**	351.67	4.733	2.976	3.384	2.840	76.49	95.06
	SCAN	345.41	4.638	3.013	3.342	2.839	77.161	94.457
CsPmS$_2$	**GGA**	374.61	5.117	2.979	3.533	2.855	73.34	95.27
	SCAN	367.73	5.071	3.006	3.503	2.846	73.384	94.678
CsYS$_2$	**GGA**	352.89	5.138	2.915	3.497	2.784	71.94	95.09
	SCAN	348.12	5.123	2.922	3.480	2.772	71.792	94.789
CsScS$_2$	**GGA**	314.55	5.221	2.738	3.447	2.635	68.89	95.46
	SCAN	310.88	5.213	2.748	3.436	2.626	68.687	95.125

The layered rhombohedral α-$NaFeO_2$ structure formed by alternative layers of AS_6 and BS_6 octahedra. However, all bond lengths in such octahedral are identical A-S_i in AS_6 and B-S_i in BS_6 (i= 1-6). Bond lengths between sulphur atoms of the same sheet (edge-sharing between AsS_6 and RES_6 octahedral) are equal to the lattice parameter *a*, we can write S_1–S_1= S_2–S_2 = S_3–S_3 = *a* see **figure IV.2**. While the distance between the sulphur atoms of two consecutive sheets (S_1–S_2 or S_2–S_3) is affected by the cation type (A, or B), which is between them. Also, both AS_6 and BS_6 distorted octahedra are characterized by two unequal angles differ from 90° (α = S_2–A–S_2 = S_3–A–S_3 and S_2–A–S_3 = $180° - \alpha$ in AS_6 octahedral, and β = S_1–B–S_1=S_2–B–S_2 and S_1–B–S_2=$180° - \beta$ in BS_6 octahedral) see **figure IV.2**.

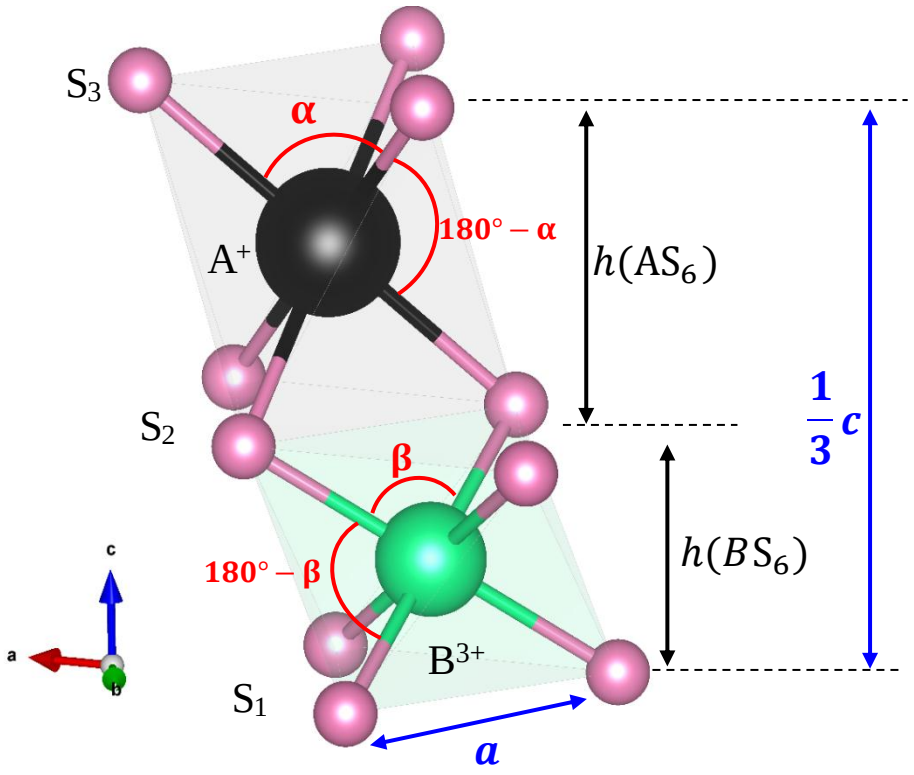

Figure IV.2. *Schematic representation AS_6 and BS_6 octahedral of ABS_2 in the layered rhombohedral α-$NaFeO_2$-type structure.*

From the data in **table IV.2**, one can see that with increase the atomic number *Z* of alkali metals from Li to Cs (in other words, increases ionic radii of six-coordinates of alkali metal Li-Cs (annexe **table S02**)), the interatomic distances A–S increased and the angle *α* decreased, which lead to more distortion for AS_6 octahedron. Therefore, unit-cell parameters *a* and *c*, and the monovalent layers' width *h*(AS_6) increased. Besides, a slight increase was observed for B–S, *h*(BS_6) and *β*. This explains the increase of unit-cell parameter *c*. On the other hand, with increasing the atomic number *Z* of trivalent cations Sc<Y<Pm, the interatomic distances B–S increased and the angle *β* decreased, and hence the trivalent layers' width *h*(BS_6) become more thickness along Sc<Y<Pm. whereas, a small decrease is observed for the monovalent layers *h*(AS_6). Finally, the augmentation of the ionic radii of the alkali metals have much influence on the unit-cell parameter *c* and a slight effect on *a* (the percentage rise of *c* for these materials is Li-Na (01.59%), Na→K (01.79%), K→Rb(0.46%), Rb→Cs (05.58%), and for *a* is Li→Na (7.17%), Na→K(10.49%), K→Rb(04.39%), Rb→Cs (0.46%)). Whilst, the increasing of the trivalent cation RE^{3+} has invers effect (*c* rising is Sc→Y (0.41%), Y→Pm (01.02%), and for *a* is Sc→Y (02.5%),

Y→Pm (05%)). These results are very similar to those presented in **figure I.4,** and reported in the reference [44].

IV.3.2 Formation energy and phase stability

The formation energy can describe the amount of energy that comes in or out when a chemical reaction occurs. Thus, it can be used as a scale for the thermodynamical stability. In definition, the formation energy is the total energy of the products minus the total energy of the reactants.

$$E_{formation} = E_{products} - E_{reactants}$$

Here, to understand the thermodynamic stabilities of the considered materials their formation energy was calculated by using both GGA and SCAN functionals. Here the Formation energies of ABS$_2$ compounds were predicted using the following relation:

$$E_{form}^{ABS_2} = E_{total}^{ABS_2} - \left[E_{Solid}^{A} + E_{Solid}^{B} + E_{Solid}^{S}\right]$$

Where $E_{total}^{ABS_2}$ is the total energy of ABS$_2$ compounds in the considered phase, and $E_{Solid}^{A} + E_{Solid}^{B} + E_{Solid}^{S}$ are the total of (A= Li, Na, K, Rb, Cs; B= Sc, Y, Pm; and S) in their standard structures.

Table IV.3: *The calculate formation energies of CsScS2, CsYS$_2$, and APmS$_2$ (A= Li, Na, K, Rb, Cs) in α-NaFeO$_2$ structure-type using both GGA and SCAN functionals.*

	Formation Energy (eV/formula unit)	
	GGA	**SCAN**
LiPmS$_2$	-7.214451777	-8.210765254
NaPmS$_2$	-7.256888795	-8.329740368
KPmS$_2$	-7.411258045	-8.491620299
RbPmS$_2$	-7.348817084	-8.452890409
CsPmS$_2$	-7.281984389	-8.399657671
CsScS$_2$	-6.717618839	-7.851889619
CsYS$_2$	-7.39967433	-8.569724201

The calculated results of the formation energy are set out in ***Table IV.3***. All the studied compounds have negative formation energy values; however, we can conclude that these materials are thermodynamically stable and feasible to synthesize experimentally with α-NaFeO$_2$ phase.

IV.3.3 Phonon dispersion

One of the powerful methods can reveal information on the stability or instability of crystal structure and the possible phase transitions, which is calculations of vibrational frequencies for the considered material. Where if all phonon frequencies are positive indicating that the system is stable, otherwise, the crystal is unstable. In order to confirm the dynamical stability of the studied materials, we have calculated their phonon dispersion. ***Figure IV.3*** shows the obtained phonon dispersion curves.

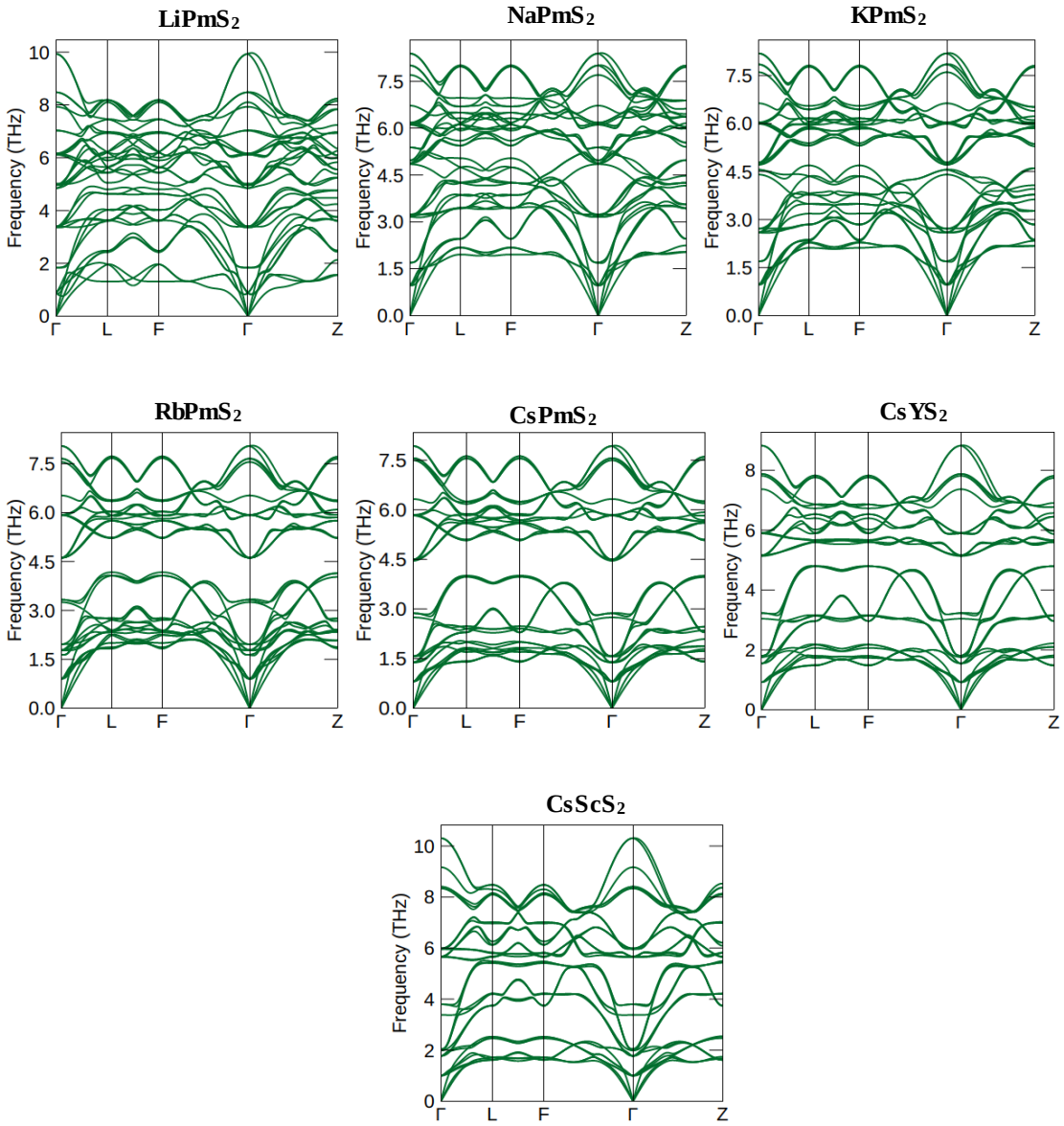

Figure IV.3 *The calculated phonon spectra of $CsScS_2$, $CsYS_2$, and $APmS_2$ (A= Li, Na, K, Rb, Cs) using GGA.*

As can be seen from ***Figure IV.3***, there are no imaginary phonons, indicating that these materials are dynamically stable. Also, one notable feature from the figure is band gap between the acoustic and optical modes, we can clearly see that this band gap was observed for $RbPmS_2$, $CsPmS_2$, $CsYS_2$ and very small for $KPmS_2$. while is not observed for $LiPmS_2$, $NaPmS_2$ and $CsScS_2$ compounds.

It has been shown that the gap between acoustic and optic phonons related with the thermal conductivity, where larger gap value often means higher thermal conductivity. Which in fact, is describing the weak coupling of heat-carrying acoustic phonons with optic phonons [45-47]. Therefore, we can conclude that $RbPmS_2$, $CsPmS_2$, $CsYS_2$ and have high thermal conductivity compared to the other compounds.

IV.3.4 Electronic properties

IV.3.4.1 Band structure and density of states

Due to the similarity in the obtained figures using GGA, SCAN and HSE06 for $CsScS_2$, $CsYS_2$, and $APmS_2$ (A= Li, Na, K, Rb, Cs), only those calculated by HSE06 have been taken as an example for plotting; band structure along with the high symmetry direction in the first Brillouin zone ***(figures IV.4)***, the total (TDOS) and partial (PDOS) density of state ***(figures IV.5).***

From a general point of view, all considered materials have almost a similar band structure, except for LiPmS2, which does not show any bands degenerate at the valence band maximum. Furthermore, we can see that all ABS_2 compounds are semiconductors with an indirect band gap. Where the valence band maximum (VBM) located at Γ high symmetry point and the conduction band minimum situated at M point. It is clearly seen from ***figure IV.5*** that the upper of the valence band for the considered materials is composed of the occupied *S-3p* orbitals mixed with a small contribution of *B-d* (*B*: rare earth atoms). On the other hand, the lower of the conduction band is mainly formed by the *B-d* orbitals.

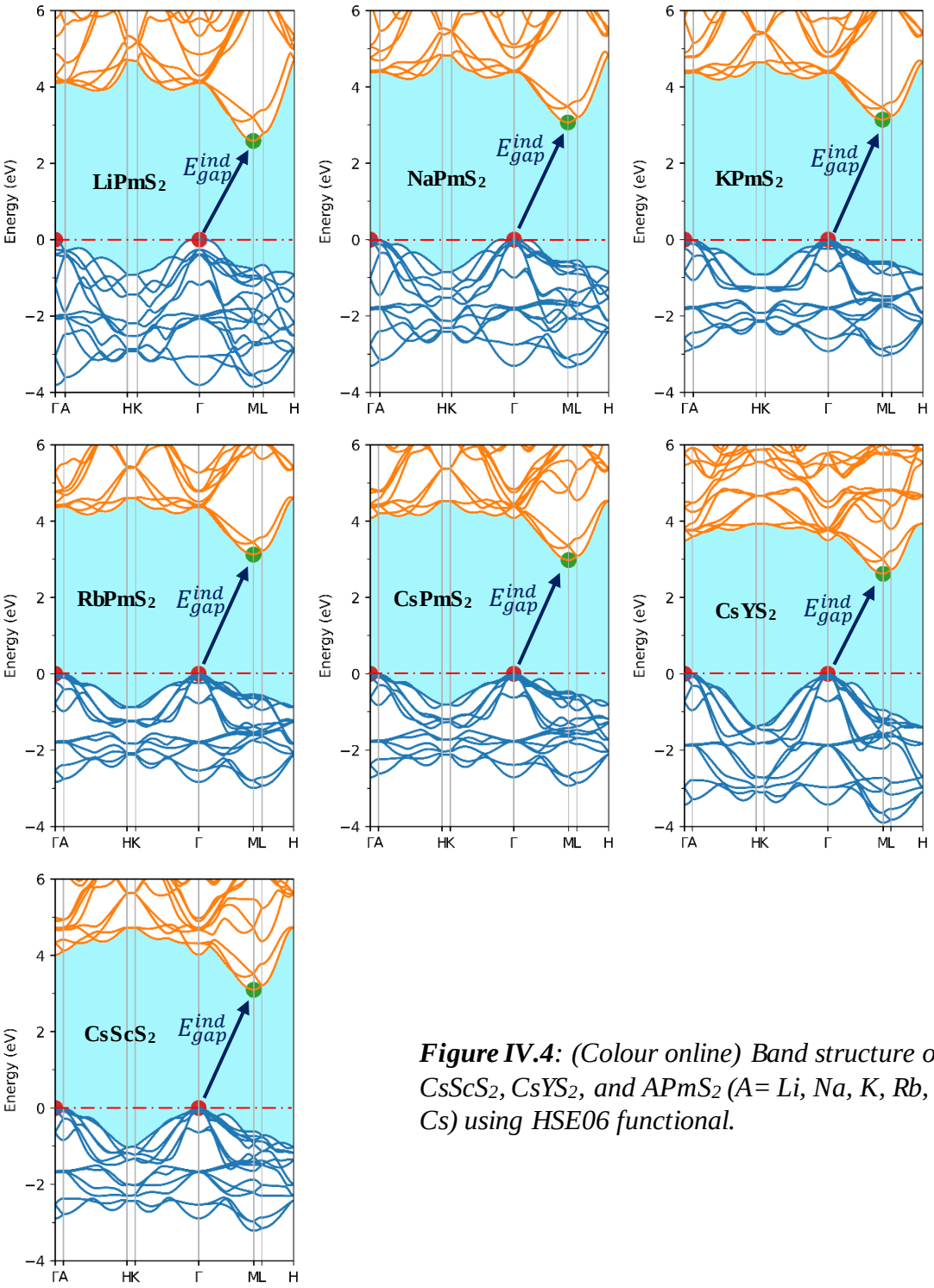

***Figure IV.4**: (Colour online) Band structure of $CsScS_2$, $CsYS_2$, and $APmS_2$ (A= Li, Na, K, Rb, Cs) using HSE06 functional.*

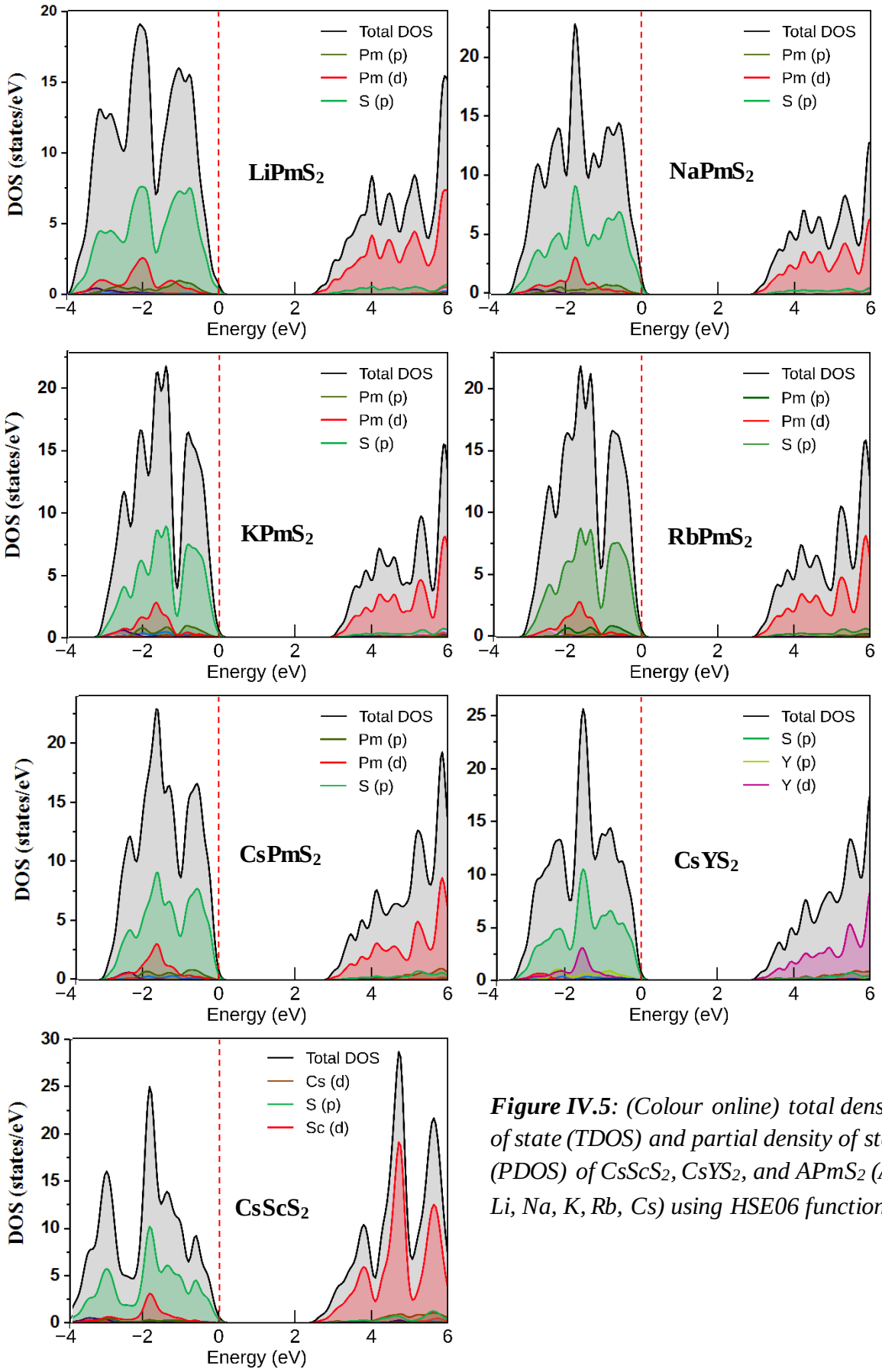

***Figure IV.5**: (Colour online) total density of state (TDOS) and partial density of state (PDOS) of $CsScS_2$, $CsYS_2$, and $APmS_2$ (A= Li, Na, K, Rb, Cs) using HSE06 functional.*

The calculated indirect and direct (optical) band gaps using GGA, SCAN and HSE06 are illustrated in **table IV.4**. As it's known, for most semiconductors, hybrid functional usually predict the accurate fundamental band gaps.

Table IV.4: *The calculated indirect and direct (optical) band gaps using GGA, SCAN and HSE06 functionals.*

		$LiPmS_2$	$NaPmS_2$	$KPmS_2$	$RbPmS_2$	$CsPmS_2$	$CsYS_2$	$CsScS_2$
GGA	E_{Gap}^{ind}	1.7913	2.2187	2.284	2.2736	2.1473	2.1748	1.655
	E_{Gap}^{dir}	2.44	2.716	2.780	2.746	2.537	2.700	2.363
SCAN	E_{Gap}^{ind}	2.093	2.549	2.596	2.578	2.430	2.503	1.969
	E_{Gap}^{dir}	2.785	3.069	3.108	3.062	2.841	3.057	2.733
HSE	E_{Gap}^{ind}	2.587	3.067	3.142	3.126	2.978	3.098	2.620
	E_{Gap}^{dir}	3.329	3.645	3.716	3.669	3.442	3.712	3.486

From **table IV.4**, the calculated band gaps values using SCAN functional are closer to those HSE06, indicating that SCAN improves the GGA band gap in our case. These semiconductors characterized by wide band gap. Where the smaller gaps is $LiPmS_2$ with direct and indirect band gaps of 2.587 eV and 3.329 eV, respectively (using HSE06). The largest band gaps is $KPmS_2$ direct (3.142 eV) and indirect band gap (3. 716 eV). We can see there is a large difference between the indirect and direct band gap in these materials. However, what we are interested in for TCMs is the direct band gap, because at room temperature the indirect optical transitions are very weak, in fact, they require both photon and phonon processes as well. So, materials with small direct band gap is transparent as long as it has a large fundamental direct (optical) band gap (> 3.1 eV), which in fact represent the first optical transition. Based on our calculated results in **table IV.4,** all the considered materials have suitable band gap for TCMs. Also, this makes them very important materials for the wide and ultra wide-bandgap semiconductors applications.

One can get insight into the chemical bonding nature of materials by considering the charge density distributions. The 2D charge density distribution of the studied materials in the plan (110), is plotted in ***Figure IV.6***. From the map in this figure, we can distinguish two different types of chemical bond; A–S (A= Li, Na, K, Rb, Cs) and B–S (B= Sc, Y, Pm). The charge distribution around A atoms is more spherical, and almost the is no overlapping between A atom and S, indicating that the bonding between A and S (A–S) is mainly ionic with

somewhat covalent features. The deformation and the overlapping of charge distribution between B and S atoms reveal the presence of the covalent bond between B and S (B–S).

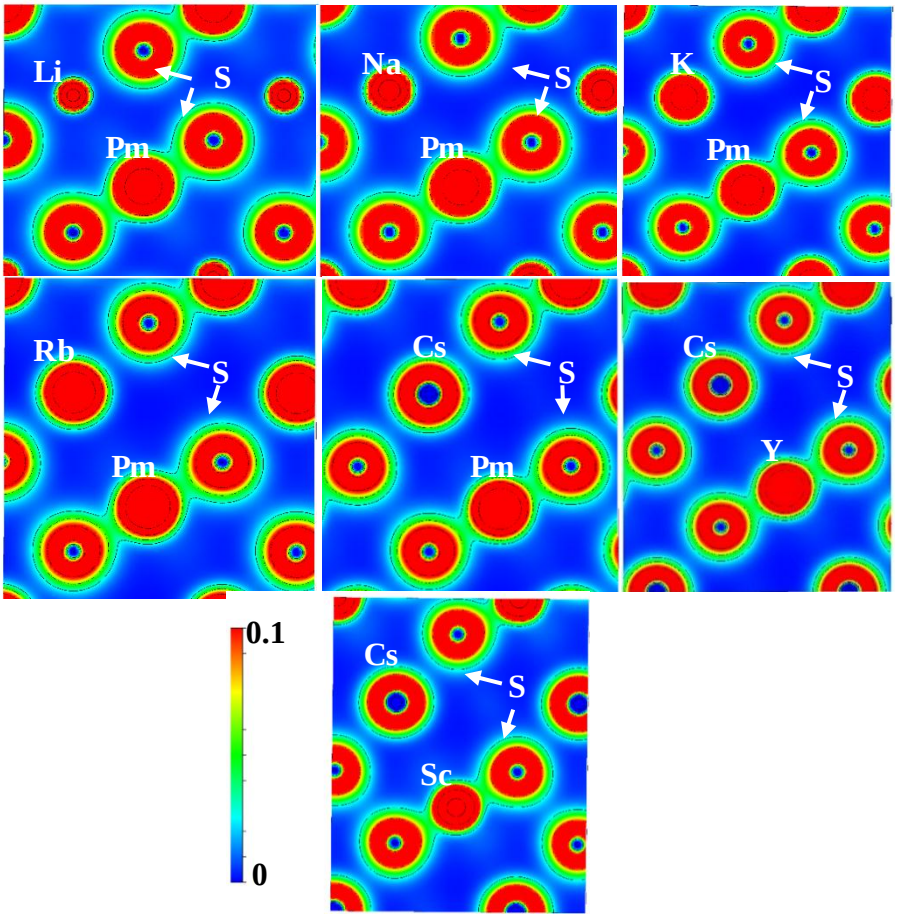

Figure IV.6: *Charge density distribution maps in (110) plane for $CsScS_2$, $CsYS_2$, and $APmS_2$ (A= Li, Na, K, Rb, Cs) in α-$NaFeO_2$ structure-type.*

IV.3.4.2 Effective mass

Except for LiPmS2 compound, there are two bands that degenerate at the valence band maximum at the Brillouin zone centre, Γ. which means that these materials have a heavy-hole band (HH) and the light hole band (LH), producing respectively, light and heavier effective masses. The calculated heavy-hole effective masses and the light-hole effective masses in the Γ→K and Γ→M directions, electron effective masses in the M→Γ and M→L directions of the studied materials are summarized in **table IV.5**.

Table IV.5: *The calculated effective masses (m_h^* and m_e^*) using GGA, SCAN and HSE06 functionals. The effective masses are in units of the free electron effective mass.*

Compound	Method	m_h^*				m_e^*	
		Light		Heavy			
		Γ → K	Γ → *M*	Γ → K	Γ → *M*	*M* → Γ	*M* → *L*
LiPmS$_2$	**GGA**	-	-	10.262	9.968	0.716	0.554
	SCAN	-	-	9.110	9.555	0.696	0.492
	HSE	-	-	9.964	10.85	0.677	0.418
NaPmS$_2$	**GGA**	0.264	0.264	1.056	1.039	0.873	0.716
	SCAN	0.276	0.277	1.069	1.052	0.821	0.728
	HSE	0.259	0.259	1.009	0.998	0.815	0.728
KPmS$_2$	**GGA**	0.273	0.272	0.970	0.961	0.982	0.651
	SCAN	0.282	0.283	0.965	0.971	0.923	0.597
	HSE	0.266	0.266	0.914	0.923	0.904	0. 582
RbPmS$_2$	**GGA**	0.273	0.272	0.975	0.971	0.971	0.602
	SCAN	0.281	0.281	0.965	0.975	0.914	0.548
	HSE	0.268	0.267	0.912	0.914	0.856	0.548
CsPmS$_2$	**GGA**	0.278	0.277	0.963	0.959	0.880	0.546
	SCAN	0.286	0.287	0.980	0.975	0.822	0.491
	HSE	0.271	0.271	0.913	0.907	0.822	0.491
CsYS$_2$	**GGA**	0.269	0.268	0.953	0.949	0.88	0.706
	SCAN	0.283	0.281	0.961	0.964	0.833	0.513
	HSE	0.264	0.263	0.931	0.935	0.804	0.495
CsScS$_2$	**GGA**	0.241	0.240	0.762	0.763	1.065	0.506
	SCAN	0.246	0.246	0.773	0.762	0.977	0.505
	HSE	0.233	0.233	0.747	0.746	0.907	0.522

Firstly, the band structure of LiPmS2 did not show any degenerate bands and the band curvature flatter at the Brillouin zone centre, Γ. This leads to a much higher value of hole effective mass ~ 10 m$_e$. While it characterized by lower electron effective masses about 0.677 m_e and 0.418 me along M →Γ and M→L, respectively. As can be seen from the table, the lighter masses increase down the group in the periodic table (Na → K → Rb → Cs) from NaPmS$_2$ (0.264 m_e) to CsPmS$_2$ (0.271 m_e), with increasing the atomic number Z (and hence the atomic radii) of the alkali metals in APmS$_2$. Also, the lighter hole effective masses decrease with increasing the atomic number *Z* of rare earth element with 0.233 m_e → 0.264 m_e → 0.286 m$_e$ for CsScS$_2$ → CsYS$_2$ → CsPmS$_2$. We can say that these values are competitive with the industry standard n-type electron effective masses In$_2$O$_3$(0.3 m_e)[48], ZnO (0.29 m_e) [49], SnO$_2$ (~ 0.28 m_e) [50] and BaSnO$_3$ (0.22 m_e) [15].

For the heavier hole effective masses, no particular trend is observed with substitution of either alkali metal or rare earth elements, whereas the values are ranged between the lower which belong to $CsScS_2$ (~0.74 m_e) and $NaPmS_2$ (~1.009 m_e). These heavy hole effective masses of the studied materials except for $LiPmS_2$ are superior to some of the top performing p-type TCMs such as $(Cu_2S_2)(Sr_3Sc_2O_5)$ (0.9 m_e)[51] and LaCuOSe:Mg (1.06 m_e) [52].

IV.3.5 Optical properties

Figure IV.7 Shows the real $\varepsilon_1(\omega)$ and imaginary $\varepsilon_2(\omega)$ parts of the dielectric function for ABS$_2$, versus incident photon energy obtained using HSE06 functional. According to ***Figure IV.7*** For all the studied materials, the real $\varepsilon_1(\omega)$ and imaginary $\varepsilon_2(\omega)$ of the dielectric function show a considerable shifting to the high energy along [100] direction compared to [001] direction implies that their optical properties have an anisotropic behaviour in [100] and [001] directions. The computed static dielectric constant $\varepsilon_1(0)$ of the considered materials are presented in **table IV.6.**

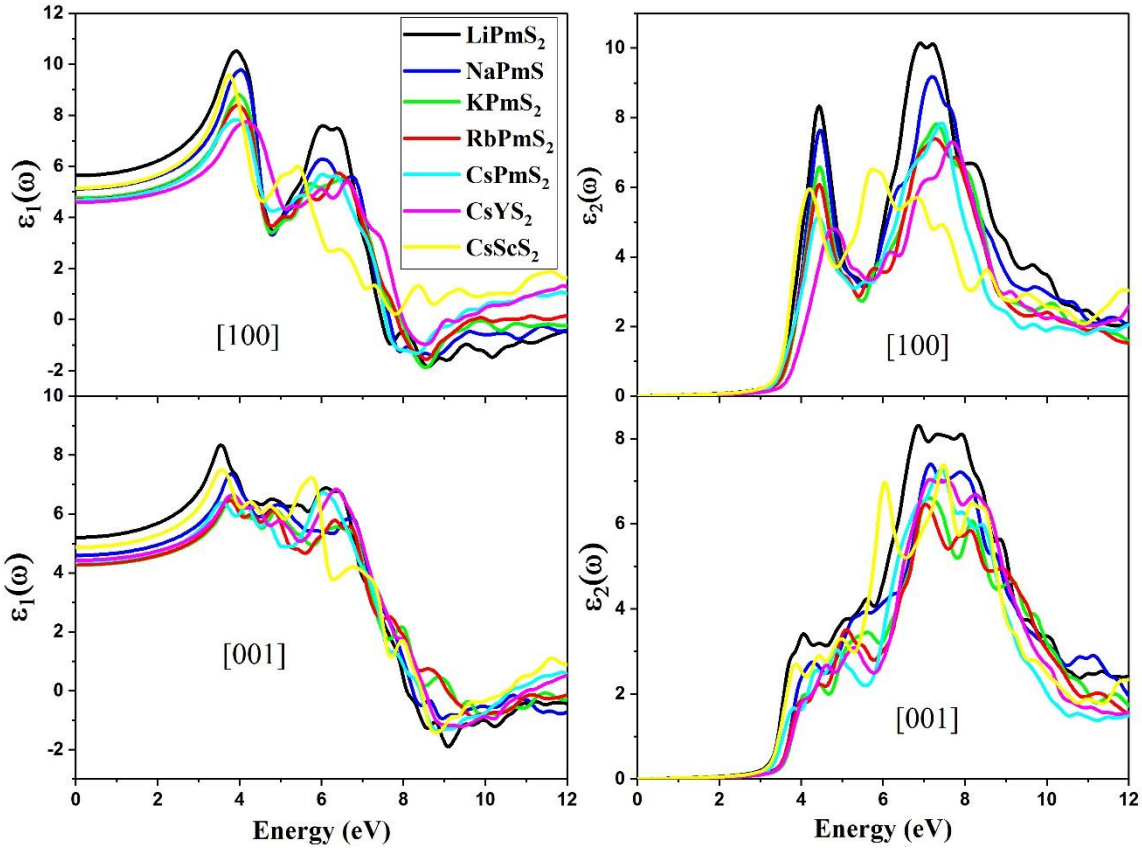

Figure IV.7: *Real and imaginary parts of the dielectric function for incident radiation with electric field polarized parallel to the three different crystal directions, [100] (or [010]) and [001], for the $CsScS_2$, $CsYS_2$, and $APmS_2$ (A= Li, Na, K, Rb, Cs) compounds, using HSE06 functional.*

The calculated refractive index $n(\omega)$ of CsScS$_2$, CsYS$_2$, and APmS$_2$ (A= Li, Na, K, Rb, Cs) along the main crystallography directions [100] and [001], is presented in ***Figure IV.8.*** The obtained static refractive index $n(0)$ for both directions [100] and [001] are summarized in **table IV.6,** together with the refractive index values at 3.1 eV (limit of the visible region). Firstly, form the figure **Figure IV.8**, we can see that along [100] direction, the refractive index decreases with increasing the atomic number *Z* of the alkali metal in APmS$_2$ from Li to Cs. This not the case for [001] direction. However, from **table IV.6,** our calculated refractive index in the IR and visible region of these materials is quite large, which are closer to other well-known visible transparent semiconductors (1.46–1.51 from 2.3 eV to 5.2 eV for SiO2 glass [53] and 2.36–2.78 from 1.2 eV to 3.4 eV for w-GaN [54]).

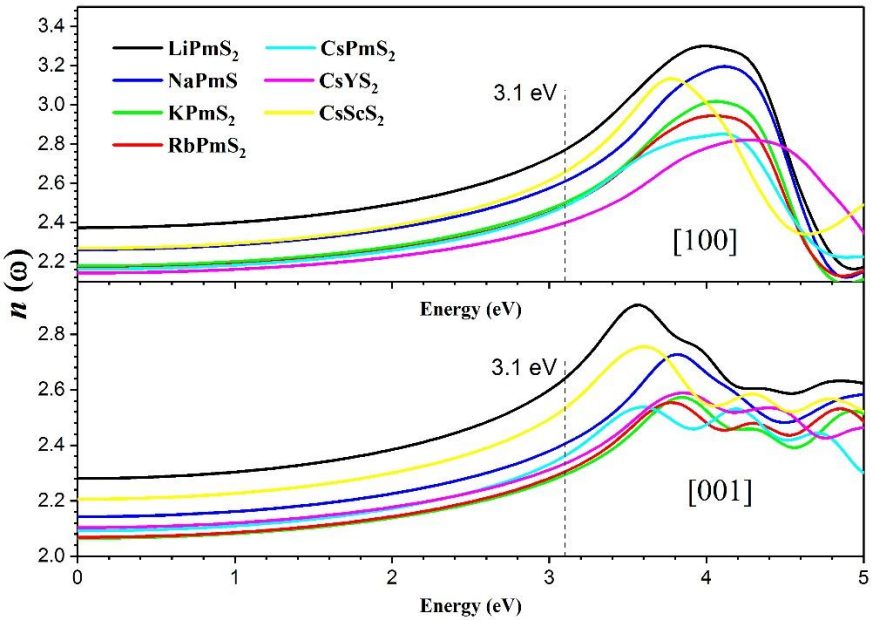

Figure IV.8 *The calculated refractive index $n(\omega)$ spectra of CsScS$_2$, CsYS$_2$, and APmS$_2$ (A= Li, Na, K, Rb, Cs), using HSE06 functional.*

The calculated frequency-dependent absorption spectrum $\alpha(\omega)$ for CsScS$_2$, CsYS$_2$, and APmS$_2$ (A= Li, Na, K, Rb, Cs) compounds are presented in 16 ***Figure IV.9***. From the figure, we can clearly see that all the considered material has no absorption in the whole IR and visible regions. Besides, the reflected light from the material's surface can be described by the reflection coefficient $R(\omega)$. ***Figure IV.10*** presents the calculated optical reflectivity spectrum of the considered materials for both main optical directions. Moreover, the obtained static reflectivity along [100] and [001] direction are presented in **table IV.6**.

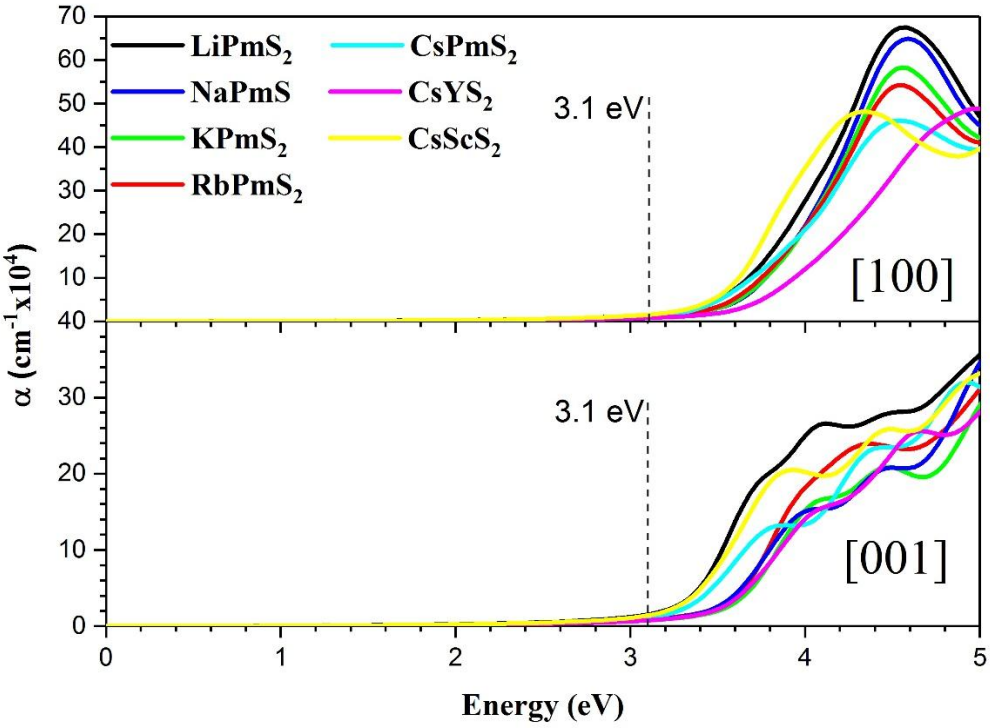

Figure IV.9 *calculated absorption coefficient $\alpha(\omega)$ spectra of $CsScS_2$, $CsYS_2$, and $APmS_2$ (A= Li, Na, K, Rb, Cs), using HSE06 functional.*

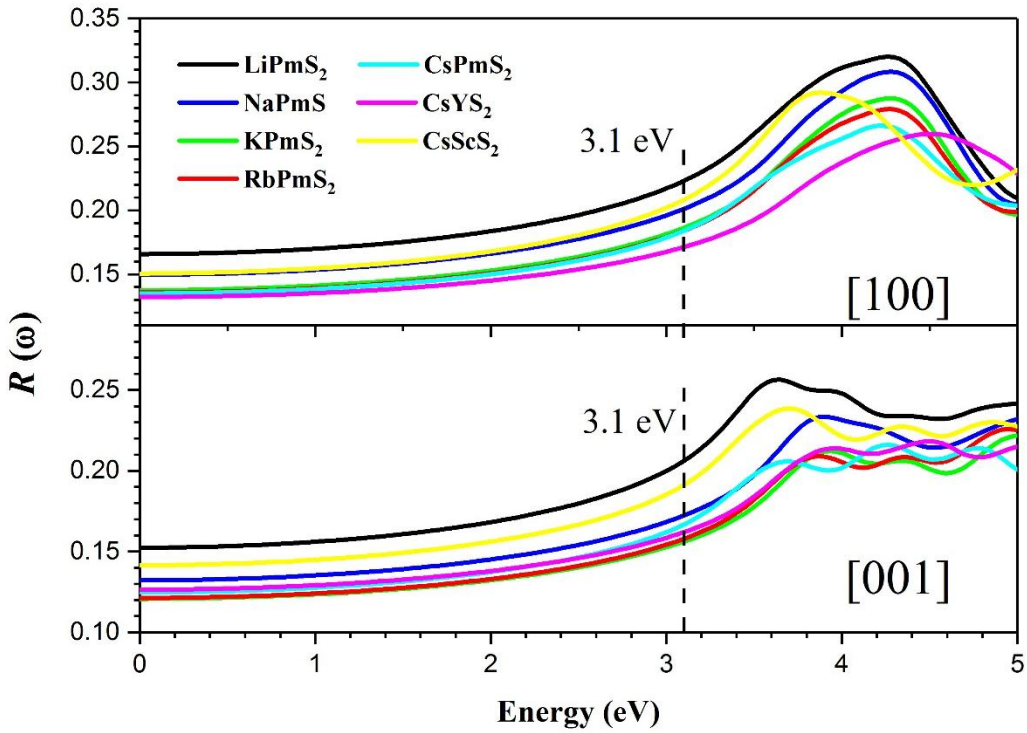

Figure IV.10 *The calculated reflectivity $R(\omega)$ spectra of $CsScS_2$, $CsYS_2$, and $APmS_2$ (A= Li, Na, K, Rb, Cs), using HSE06 functional.*

All the studied compounds are slightly more reflect to the incident light along [100] than [001]. LiPmS$_2$ have high reflectivity than the other materials in both main optical directions [100] and [001]. While, CsYS$_2$ have lower reflectivity along [100], whereas KPmS$_2$ represent the lower reflectivity along [001]. Furthermore, the reflectivity in the whole visible region does not exceed 21.82 %, 19.13%, 17.6 %, 17.52 %, 17.5 %, 16.821 %, and 20.21 % for LiPmS$_2$, NaPmS$_2$, KPmS$_2$, RbPmS$_2$, CsPmS$_2$, CsYS$_2$, and CsScS$_2$ compounds, respectively.

Table IV.6: *Calculated $\varepsilon(0), n(0), n(3.1)$ and $R(0)$ for [100] and [001] principal optical directions for CsScS$_2$, CsYS$_2$, and APmS$_2$ (A= Li, Na, K, Rb, Cs) materials.*

Compound	Direction	$\varepsilon(0)$	$n(\omega)$		$R(0)$
			$n(0)$	$n(3.1)$	
LiPmS$_2$	[100]	5.63	2.37	2.77	16.58
	[001]	5.20	2.28	2.64	15.23
NaPmS$_2$	[100]	5.12	2.26	2.61	14.97
	[001]	4.59	2.14	2.40	13.22
KPmS$_2$	[100]	4.75	2.18	2.50	13.75
	[001]	4.26	2.06	2.29	12.077
RbPmS$_2$	[100]	4.69	2.17	2.48	13.57
	[001]	4.27	2.07	2.30	12.13
CsPmS$_2$	[100]	4.67	2.61	2.48	13.50
	[001]	4.37	2.09	2.35	12.47
CsYS$_2$	[100]	4.59	2.14	2.40	13.225
	[001]	4.42	2.10	2.33	12.64
CsScS$_2$	[100]	5.15	2.26	2.64	15.06
	[001]	4.86	2.20	2.53	14.15

IV.4 Conclusion

In this chapter, three different functionals have been used, largely used GGA functional, the new developed SCAN meta-GGA functional and the more accurate HSE06 functional, to investigate the crystal structure stability and physical properties of the ternary semiconductors CsScS$_2$, CsYS$_2$, and APmS$_2$ (A= Li, Na, K, Rb, Cs). These compounds have not been synthesized yet, and are not found in the large materials database like materials project, COD, AFLOWLIB, or OQMD. We found that these materials are thermodynamically stable and feasible to synthesize experimentally with α-NaFeO$_2$ structure-type. These compounds (except for LiPmS$_2$ which have large hole effective mass) have even larger optical band gaps (more than 3.4 eV) and light effective masses of only about 0.22 m$_e$, heavy effective masses between 0.74 and 1 m$_e$. Based on the obtained results these materials could be better p-type transparent conducting materials than those already known.

References

[1] F. Odobel, L. Le Pleux, Y. Pellegrin, E. Blart, New photovoltaic devices based on the sensitization of p-type semiconductors: challenges and opportunities, Accounts of chemical research 43(8) (2010) 1063-1071.

[2] J.P. Allen, D.O. Scanlon, S.C. Parker, G.W. Watson, Tin monoxide: structural prediction from first principles calculations with van der Waals corrections, The Journal of Physical Chemistry C 115(40) (2011) 19916-19924.

[3] H.-J. Kim, J.-H. Lee, Highly sensitive and selective gas sensors using p-type oxide semiconductors: Overview, Sensors and Actuators B: Chemical 192 (2014) 607-627.

[4] E. Fortunato, P. Barquinha, R. Martins, Oxide semiconductor thin-film transistors: a review of recent advances, Advanced materials 24(22) (2012) 2945-2986.

[5] R.G. Gordon, Criteria for choosing transparent conductors, Mrs Bulletin 25(8) (2000) 52-57.

[6] K.H. Zhang, K. Xi, M.G. Blamire, R.G. Egdell, P-type transparent conducting oxides, Journal of physics: Condensed matter 28(38) (2016) 383002.

[7] J.C. Fan, F.J. Bachner, G.H. Foley, Effect of O_2 pressure during deposition on properties of rf-sputtered Sn-doped In2O3 films, Applied Physics Letters 31(11) (1977) 773-775.

[8] D.S. Bhachu, D.O. Scanlon, G. Sankar, T. Veal, R.G. Egdell, G. Cibin, A.J. Dent, C.E. Knapp, C.J. Carmalt, I.P. Parkin, Origin of high mobility in molybdenum-doped indium oxide, Chemistry of Materials 27(8) (2015) 2788-2796.

[9] J.E. Swallow, B.A. Williamson, T.J. Whittles, M. Birkett, T.J. Featherstone, N. Peng, A. Abbott, M. Farnworth, K.J. Cheetham, P. Warren, Self-compensation in transparent conducting F-doped SnO2, Advanced Functional Materials 28(4) (2018) 1701900.

[10] M.J. Powell, B.A. Williamson, S.-Y. Baek, J. Manzi, D.B. Potter, D.O. Scanlon, C.J. Carmalt, Phosphorus doped SnO_2 thin films for transparent conducting oxide applications: synthesis, optoelectronic properties and computational models, Chemical science 9(41) (2018) 7968-7980.

[11] A. Suzuki, T. Matsushita, N. Wada, Y. Sakamoto, M. Okuda, Transparent conducting Al-doped ZnO thin films prepared by pulsed laser deposition, Japanese journal of applied physics 35(1A) (1996) L56.

[12] H. Agura, A. Suzuki, T. Matsushita, T. Aoki, M. Okuda, Low resistivity transparent conducting Al-doped ZnO films prepared by pulsed laser deposition, Thin solid films 445(2) (2003) 263-267.

[13] S.C. Dixon, S. Sathasivam, B.A. Williamson, D.O. Scanlon, C.J. Carmalt, I.P. Parkin, Transparent conducting n-type ZnO: Sc–synthesis, optoelectronic properties and theoretical insight, Journal of Materials Chemistry C 5(30) (2017) 7585-7597.

[14] S. Sallis, D. Scanlon, S. Chae, N. Quackenbush, D. Fischer, J. Woicik, J.-H. Guo, S.-W. Cheong, L. Piper, La-doped BaSnO3—Degenerate perovskite transparent conducting oxide: Evidence from synchrotron x-ray spectroscopy, Applied Physics Letters 103(4) (2013) 042105.

[15] D.O. Scanlon, Defect engineering of $BaSnO_3$ for high-performance transparent conducting oxide applications, Physical review B 87(16) (2013) 161201.

[16] J. Kim, T. Sekiya, N. Miyokawa, N. Watanabe, K. Kimoto, K. Ide, Y. Toda, S. Ueda, N. Ohashi, H. Hiramatsu, Conversion of an ultra-wide bandgap amorphous oxide insulator to a semiconductor, NPG Asia Materials 9(3) (2017) e359-e359.

[17] S. Pearton, J. Yang, P.H. Cary IV, F. Ren, J. Kim, M.J. Tadjer, M.A. Mastro, A review of Ga2O3 materials, processing, and devices, Applied Physics Reviews 5(1) (2018) 011301.

[18] Z. Wang, P.K. Nayak, J.A. Caraveo-Frescas, H.N. Alshareef, Recent developments in p-Type oxide semiconductor materials and devices, Advanced materials 28(20) (2016) 3831-3892.

[19] L. Chen, J. Yang, S. Klaus, L.J. Lee, R. Woods-Robinson, J. Ma, Y. Lum, J.K. Cooper, F.M. Toma, L.-W. Wang, p-Type transparent conducting oxide/n-type semiconductor heterojunctions for efficient and stable solar water oxidation, Journal of the American Chemical Society 137(30) (2015) 9595-9603.

[20] J. Sun, A. Ruzsinszky, J.P. Perdew, Strongly constrained and appropriately normed semilocal density functional, Physical Review Letters 115(3) (2015) 036402.

[21] F. Tran, J. Stelzl, P. Blaha, Rungs 1 to 4 of DFT Jacob's ladder: Extensive test on the lattice constant, bulk modulus, and cohesive energy of solids, The Journal of chemical physics 144(20) (2016) 204120.

[22] Y. Hinuma, H. Hayashi, Y. Kumagai, I. Tanaka, F. Oba, Comparison of approximations in density functional theory calculations: Energetics and structure of binary oxides, Physical review B 96(9) (2017) 094102.

[23] Y. Zhang, J. Sun, J.P. Perdew, X. Wu, Comparative first-principles studies of prototypical ferroelectric materials by LDA, GGA, and SCAN meta-GGA, Physical review B 96(3) (2017) 035143.

[24] L. Goerigk, A. Hansen, C. Bauer, S. Ehrlich, A. Najibi, S. Grimme, A look at the density functional theory zoo with the advanced GMTKN55 database for general main group

thermochemistry, kinetics and noncovalent interactions, Physical Chemistry Chemical Physics 19(48) (2017) 32184-32215.

[25] A. Patra, J.E. Bates, J. Sun, J.P. Perdew, Properties of real metallic surfaces: Effects of density functional semilocality and van der Waals nonlocality, Proceedings of the National Academy of Sciences 114(44) (2017) E9188-E9196.

[26] R.C. Remsing, M.L. Klein, J. Sun, Dependence of the structure and dynamics of liquid silicon on the choice of density functional approximation, Physical review B 96(2) (2017) 024203.

[27] M. Chen, H.-Y. Ko, R.C. Remsing, M.F.C. Andrade, B. Santra, Z. Sun, A. Selloni, R. Car, M.L. Klein, J.P. Perdew, Ab initio theory and modeling of water, Proceedings of the National Academy of Sciences 114(41) (2017) 10846-10851.

[28] G. Zhao, S. Shi, H. Xie, Q. Xu, M. Ding, X. Zhao, J. Yan, D. Wang, Equation of state of water based on the SCAN meta-GGA density functional, Physical Chemistry Chemical Physics 22(8) (2020) 4626-4631.

[29] C. Shahi, J. Sun, J.P. Perdew, Accurate critical pressures for structural phase transitions of group IV, III-V, and II-VI compounds from the SCAN density functional, Physical review B 97(9) (2018) 094111.

[30] N. Sengupta, J.E. Bates, A. Ruzsinszky, From semilocal density functionals to random phase approximation renormalized perturbation theory: A methodological assessment of structural phase transitions, Physical review B 97(23) (2018) 235136.

[31] X. Zhang, Z. Zhang, S. Yao, A. Chen, X. Zhao, Z. Zhou, An effective method to screen sodium-based layered materials for sodium ion batteries, npj Computational Materials 4(1) (2018) 1-6.

[32] G.-X. Zhang, A.M. Reilly, A. Tkatchenko, M. Scheffler, Performance of various density-functional approximations for cohesive properties of 64 bulk solids, New Journal of Physics 20(6) (2018) 063020.

[33] C.J. Bartel, A.W. Weimer, S. Lany, C.B. Musgrave, A.M. Holder, The role of decomposition reactions in assessing first-principles predictions of solid stability, npj Computational Materials 5(1) (2019) 1-9.

[34] B.J. Kennedy, Q. Zhou, S. Zhao, F. Jia, W. Ren, K.S. Knight, Low-temperature structure and the ferroelectric phase transitions in the CdTi O 3 perovskite, Physical review B 96(21) (2017) 214105.

[35] J. Sun, R.C. Remsing, Y. Zhang, Z. Sun, A. Ruzsinszky, H. Peng, Z. Yang, A. Paul, U. Waghmare, X. Wu, Accurate first-principles structures and energies of diversely bonded systems from an efficient density functional, Nature chemistry 8(9) (2016) 831.

[36] J.H. Yang, D.A. Kitchaev, G. Ceder, Rationalizing accurate structure prediction in the meta-GGA SCAN functional, Physical review B 100(3) (2019) 035132.

[37] L. Havlák, V. Jarý, M. Nikl, P. Boháček, J. Bárta, Preparation, luminescence and structural properties of RE-doped RbLaS2 compounds, Acta materialia 59(16) (2011) 6219-6227.

[38] V. Jarý, L. Havlák, J. Bárta, M. Buryi, E. Mihóková, M. Rejman, V. Laguta, M. Nikl, Optical, Structural and Paramagnetic Properties of Eu-Doped Ternary Sulfides ALnS2 (A= Na, K, Rb; Ln= La, Gd, Lu, Y), Materials 8(10) (2015) 6978-6998.

[39] V. Jarý, L. Havlák, J. Bárta, E. Mihóková, M. Buryi, M. Nikl, ALnS2: RE (A= K, Rb; Ln= La, Gd, Lu, Y): New optical materials family, Journal of luminescence 170 (2016) 718-735.

[40] M. Aubert, P. Macaudiere, Rare-earth and alkali sulphide, method for preparing same and use thereof as a pigment, Google Patents, 2001.

[41] J. Shi, T.F. Cerqueira, W. Cui, F. Nogueira, S. Botti, M.A. Marques, High-throughput search of ternary chalcogenides for p-type transparent electrodes, Scientific reports 7 (2017) 43179.

[42] Y. Ding, J. Gu, T. Zhang, A.-X. Yin, L. Yang, Y.-W. Zhang, C.-H. Yan, Chemoaffinity-mediated synthesis of NaRES2-based nanocrystals as versatile nano-building blocks and durable nano-pigments, Journal of the American Chemical Society 134(6) (2012) 3255-3264.

[43] A. Allal, M. Halit, S. Saib, L. Azzouz, S. Maabed, M. Bouchenafa, R. Ahuja, A comparative theoretical investigation of optoelectronic and mechanical properties of KYS2 and KLaS2, Materials Science in Semiconductor Processing 113 (2020) 105048.

[44] J. Fábry, L. Havlak, M. Dušek, P. Vaněk, J. Drahokoupil, K. Jurek, Structure determination of $KLaS_2$, $KPrS_2$, $KEuS_2$, $KGdS_2$, $KLuS_2$, KYS_2, $RbYS_2$, $NaLaS_2$ and crystal-chemical analysis of the group 1 and thallium (I) rare-earth sulfide series, Acta Crystallographica Section B: Structural Science, Crystal Engineering and Materials 70(2) (2014) 360-371.

[45] L. Lindsay, D. Broido, T. Reinecke, Thermal conductivity and large isotope effect in GaN from first principles, Physical Review Letters 109(9) (2012) 095901.

[46] X. Gu, R. Yang, Phonon transport in single-layer transition metal dichalcogenides: A first-principles study, Applied Physics Letters 105(13) (2014) 131903.

[47] L. Lindsay, D. Broido, Three-phonon phase space and lattice thermal conductivity in semiconductors, Journal of physics: Condensed matter 20(16) (2008) 165209.

[48] N. Preissler, O. Bierwagen, A.T. Ramu, J.S. Speck, Electrical transport, electrothermal transport, and effective electron mass in single-crystalline In 2 O 3 films, Physical review B 88(8) (2013) 085305.

[49] K.J. Button, D.R. Cohn, M. von Ortenbert, B. Lax, E. Mollwo, R. Helbig, Zeeman splitting of anomalous shallow bound states in ZnO, Physical Review Letters 28(25) (1972) 1637.

[50] K.J. Button, C.G. Fonstad, W. Dreybrodt, Determination of the electron masses in stannic oxide by submillimeter cyclotron resonance, Physical review B 4(12) (1971) 4539.

[51] D.O. Scanlon, G.W. Watson, $(Cu_2S_2)(Sr_3Sc_2O_5)$− A Layered, Direct Band Gap, p-Type Transparent Conducting Oxychalcogenide: A Theoretical Analysis, Chemistry of Materials 21(22) (2009) 5435-5442.

[52] H. Hiramatsu, K. Ueda, H. Ohta, M. Hirano, M. Kikuchi, H. Yanagi, T. Kamiya, H. Hosono, Heavy hole doping of epitaxial thin films of a wide gap p-type semiconductor, LaCuOSe, and analysis of the effective mass, Applied Physics Letters 91(1) (2007) 012104.

[53] J. Matsuoka, N. Kitamura, S. Fujinaga, T. Kitaoka, H. Yamashita, Temperature dependence of refractive index of SiO2 glass, Journal of non-crystalline solids 135(1) (1991) 86-89.

[54] M. Lin, B. Sverdlov, S. Strite, H. Morkoc, A. Drakin, Refractive indices of wurtzite and zincblende GaN, Electronics Letters 29(20) (1993) 1759-1760.

Summary and conclusions

In this thesis we have used *ab-initio* methods based on density functional density (DFT) to study different isostructural semiconductors belong to ABS_2 family. The most notable results are summarized in the following.

Using CASTEP code we have studied structural, elastic, electronic and optical properties of the ternary sulfides $KScS_2$, KYS_2, $KLaS_2$, $KLuS_2$, $RbLuS_2$, and $RbScS_2$. For the structural properties, we found that GGA-PBE gives results better than LDA. The analysis of B3LYP, GGA-PBE and LDA band structures show that these compounds have indirect band gap`, and B3LYP functional leads an excellent agreement compared to the experimental ones. The studied compounds demonstrate the optical anisotropy, while the absorption and reflectivity spectra indicate that all compounds are transparent in the infrared and visible regions. However, the calculated elastic constants and macroscopic elastic parameters confirm that all the studied materials are mechanically stable, brittle in nature, and have certain degree of elastic anisotropy. Parallelly, the thermodynamic properties of these compounds as function of temperature are estimated using the quasi-harmonic Debye model embedded in GIBBS2 code. Our results reveal that thermodynamic properties of the considered materials are less affected by temperatures lower than 100 K. Also, we found that Debye temperatures values increase along of $RbLuS_2 < KLuS_2 < KLaS_2 < RbScS_2 < KYS_2 < KScS_2$, therefore, better thermal conductivity, stronger chemical bonds and larger hardness increase in the same way $RbLuS_2 < KLuS_2 < KLaS_2 < RbScS_2 < KYS_2 < KScS_2$.

Using VASP code we have studied $CsScS_2$, $CsYS_2$, and $APmS_2$ (A= Li, Na, K, Rb, Cs) compounds for p-type transparent conducting materials (TCMs). The calculated results of the formation energy and phonon dispersion curves confirm that these materials are thermodynamically stable and feasible to synthesize experimentally in the α-NaFeO2 phase. From the obtained electronic properties using the accurate hybrid HSE06 functional, (i) all the studied materials have suitable band gap for TCMs (wide optical band gap $E_g > 3.1\ eV$). (ii) Except for $LiPmS_2$ compound, the calculated light-hole effective masses are competitive with the industry standard n-type TCOs ($In2O_3$, ZnO, and $BaSnO_3$), while the obtained heavy-hole effective masses of the studied materials except for $LiPmS_2$ are superior to some of the top performing p-type TCMs. The computed optical properties reveal that these materials have no absorption in the entire visible region and their reflectivity is less than 20

%. This makes all considered compound except for $LiPmS_2$ promising candidates for p-type TCMs.

Annexe

Table (S01): Overview of known ABS_2 materials.

Compound	Crystal system	Space group	Lattice constants		$Z(S^{2-})$	interatomic distance		Layers width	
			a	*c*		$A^{+}–S^{2-}$	$B^{3+}–S^{2-}$	$h(AS_6)$	$h(BS_6)$
$LiLaS_2$	Cubic (Th_3P_4)	I-43d							
$LiCeS_2$	Cubic (Th_3P_4)	I-43d							
$LiPrS_2$	Cubic (NaCl)	Fm-3m	5.686[1]						
$LiNdS_2$	Cubic (NaCl)	Fm-3m	5.628[1] 5.635[2]						
$LiPmS_2$ This Work	Rhombohedral (α-$NaFeO_2$)	R-3m	4.012	18.568	0.2518	2.767	2.804	3.028	3.161
$LiSmS_2$	Cubic (NaCl)	Fm-3m	5.588[1] 5.563[2]						
$LiEuS_2$	Cubic (NaCl)	Fm-3m	5.606[1] 5.572[3] 5.57[4]						
$LiGdS_2$	Cubic (NaCl)	Fm-3m	5.530[1] 5.521[2]						
$LiTbS_2$	Cubic (NaCl)	Fm-3m	5.505[1] 5.489[2]						
	Rhombohedral (α-$NaFeO_2$)	R-3m	3.891[5]	19.066					
$LiDyS_2$	Cubic (NaCl)	Fm-3m	5.474[1] 5.468[2]	-					
	Rhombohedral (α-$NaFeO_2$)	R-3m	3.897[2]	18.47	0.246	2.76842	2.685	3.22609	2.93057
$LiHoS_2$	Cubic (NaCl)	Fm-3m	5.453[2]						
	Rhombohedral (α-$NaFeO_2$)	R-3m	3.898[1] 3.892[2]	18.68 18.55	0.247	2.75934	2.69627	3.20297	2.98037
$LiErS_2$	Cubic (NaCl)	Fm-3m	5.435[2]						
	Rhombohedral (α-$NaFeO_2$)	R-3m	3.875[1] 3.881[2]	18.63 18.65	0.248	2.74836	2.70585	3.18293	3.03373
$LiTmS_2$	Rhombohedral (α-$NaFeO_2$)	R-3m	3.829[6]	18.48					
$LiYbS_2$	Rhombohedral	R-3m	3.842[1]	18.54					

	(α-$NaFeO_2$)								
$LiLuS_2$	Rhombohedral (α-$NaFeO_2$)	R-3m	3.813[6]	18.41					
$LiScS_2$	Rhombohedral (α-$NaFeO_2$)	R-3m	3.687[7]	18.318	0.231	2.83641	2.43312	3.23618	2.87
$LiYS_2$	Cubic (NaCl)	Fm-3m	5.485[2]						
	Rhombohedral (α-$NaFeO_2$)	R-3m	3.898[2] 3.9033[8]	18.56 18.522					
$NaLaS_2$	Cubic (NaCl)	Fm-3m	5.8806[9] 5.881[10] 5.878[11]						
$NaCeS_2$	Cubic (NaCl)	Fm-3m	5.832[10] [10]5.825[11] [11]5.8286						
$NaPrS_2$	Cubic (NaCl)	Fm-3m	5.777[10] 5.798[11]						
$NaNdS_2$	Cubic (NaCl)	Fm-3m	[B65]5.803						
	Rhombohedral (α-$NaFeO_2$)	R-3m	4.089 4.100[6]	20.024 19.90					
$NaPmS_2$ This Work	Rhombohedral (α-$NaFeO_2$)	R-3m	4.012	18.568	0.2518	2.949	2.812	3.555	3.078
$NaSmS_2$	Cubic (NaCl)	Fm-3m	5.740[11]						
	Rhombohedral (α-$NaFeO_2$)		4.057 4.056 [10]	19.99 19.87					
$NaEuS_2$	Rhombohedral (α-$NaFeO_2$)	R-3m	4.042[10]	19.92					
$NaGdS_2$	Rhombohedral (α-$NaFeO_2$)	R-3m	4.019[11] 4.009[10]	19.958 19.87	0.2433	2.934	2.7793	3.58613	3.047
$NaTbS_2$	Rhombohedral (α-$NaFeO_2$)	R-3m	3.994[10]	19.919					
$NaDyS_2$	Rhombohedral (α-$NaFeO_2$)	R-3m	3.978[10] 3.979[11]	19.92 19.898					
$NaHoS_2$	Rhombohedral (α-$NaFeO_2$)	R-3m	3.949[10] 3.960[11] 3.9556[12]	19.86 19.885 19.848	0.24	2.945	2.711	3.605	3.011
$NaErS_2$	Rhombohedral (α-$NaFeO_2$)	R-3m	3.939[10] 3.9335[12]	19.98 19.808	0.242	2.903	2.717	3.65	3.01
$NaTmS_2$	Rhombohedral (α-$NaFeO_2$)	R-3m	3.9159[12] 3.915[6]	19.7674 19.88	0.2427	2.885	2.714	3.58357	3.005

$NaYbS_2$	Rhombohedral (α-$NaFeO_2$)	R-3m	3.9012[12] 3.895[13] 3.929 [11]	19.736 19.831 19.833	0.2427	2.875	2.707	3.57472	3.004
$NaLuS_2$	Rhombohedral (α-$NaFeO_2$)	R-3m	3.8873[12] 3.8909[14]	19.7058 19.85	0.2428	2.866	2.700	3.647	3.002
$NaScS_2$	Rhombohedral (α-$NaFeO_2$)	R-3m	3.751[7]	19.744	0.2426	2.962	2.510	3.686	2.896
$NaYS_2$	Rhombohedral (α-$NaFeO_2$)	R-3m	3.968[10] 3.966[6] 3.9635[8] 3.9609 [14]	19.89 19.93 19.893 19.867		2.918	2.744	3.605	3.017
$KLaS_2$	Rhombohedral (α-$NaFeO_2$)	R-3m	4.464[1] 4.2651[9]	21.89 21.929	0.2371	3.242	2.907	4.217	3.092
$KCeS_2$	Rhombohedral (α-$NaFeO_2$)	R-3m	4.228[15] 4.223[1]	21.83 21.80	0.236	3.226	2.877	4.220	3.046
$KPrS_2$	Rhombohedral (α-$NaFeO_2$)	R-3m	4.1925[9] 4.185 [1]	21.892 21.75	0.23618	3.222	2.85917	4.25376	3.0436
$KNdS_2$	Rhombohedral (α-$NaFeO_2$)	R-3m	4.161[1] 4.1626[16]	21.83 21.8996	0.2353	3.222	2.8346	4.2938	3.0061
$KPmS_2$ This Work	Rhombohedral (α-$NaFeO_2$)	R-3m	4.149	21.986	0.2356	3.218	2.834	4.298	3.030
$KSmS_2$	Rhombohedral (α-$NaFeO_2$)	R-3m	4.107[1] 4.1174[16]	21.76 21.888	0.2352	3.204	2.8109	4.2959	3.0001
$KEuS_2$	Rhombohedral (α-$NaFeO_2$)	R-3m	4.093[1] 4.0981[9]	21.85 21.8212	0.23536	3.189	2.8009	4.2758	2.998
$KGdS_2$	Rhombohedral (α-$NaFeO_2$)	R-3m	4.0715[9]	21.901	0.23501	3.188	2.7868	4.3068	2.99357
$KTbS_2$	Rhombohedral (α-$NaFeO_2$)	R-3m	4.051[1] 4.0523[16]	21.87 21.885	0.23463	3.184	2.7724	4.3202	2.9748
$KDyS_2$	Rhombohedral (α-$NaFeO_2$)	R-3m	4.030[1] 4.0315[16]	21.83 21.890	0.2345	3.178	2.7609	4.3269	2.9698
$KHoS_2$	Rhombohedral (α-$NaFeO_2$)	R-3m	4.009[1] 4.0098[16]	21.80 21.878	0.2343	3.171	2.7475	4.3333	2.9593
$KErS_2$	Rhombohedral (α-$NaFeO_2$)	R-3m	3.993[1] 3.9935[16]	21.77 21.866	0.23407	3.166	2.73646	4.34098	2.94768
$KTmS_2$	Rhombohedral (α-$NaFeO_2$)	R-3m	3.977[6] 3.9761[16]	21.84 21.841	0.23376	3.162	2.72344	4.34956	2.93077
$KYbS_2$	Rhombohedral (α-$NaFeO_2$)	R-3m	3.96[1] 3.9615[16]	21.82 21.810	0.23346	3.158	2.7117	4.3565	2.9135
$KLuS_2$	Rhombohedral (α-$NaFeO_2$)	R-3m	3.947[6] 3.949[9]	21.79 21.871	0.23369	3.154	2.7105	4.3586	2.931
$KScS_2$	Rhombohedral (α-$NaFeO_2$)	R-3m	3.8106[16]	21.719	0.23113	3.125	2.60777	4.43951	2.80016

KYS_2	Rhombohedral (α-$NaFeO_2$)	R-3m	4.0216[9] 4.022[1]	21.884 21.85	0.23444	3.174	2.75515	4.32836	2.9663
$RbLaS_2$	Rhombohedral (α-$NaFeO_2$)	R-3m	4.292[17] 4.296[18] 4.28 [19]	22.89 22.93 22.9	0.2337	3.372	2.9179	4.5692	3.0741
$RbCeS_2$	Rhombohedral (α-$NaFeO_2$)	R-3m	4.249[18] 4.246[17] 4.249[19]	22.852 22.80 22.843	0.2334	3.351	2.88853	4.56735	3.04998
$RbPrS_2$	Rhombohedral (α-$NaFeO_2$)	R-3m	4.221[18]	22.897	0.2329	3.351	2.87034	4.59924	3.03309
$RbNdS_2$	Rhombohedral (α-$NaFeO_2$)	R-3m	4.194 4.189[17]	22.894 22.89	0.2327	3.342	2.8546	4.6078	3.0235
$RbPmS_2$ This Work	Rhombohedral (α-$NaFeO_2$)	R-3m	4.168	22.951	0.2323	3.342	2.839	4.638	3.013
$RbSmS_2$	Rhombohedral (α-$NaFeO_2$)	R-3m	4.141[17] 4.143[18]	22.861 22.88	0.2321	3.32962	2.82185	4.632	2.994
$RbEuS_2$	Rhombohedral (α-$NaFeO_2$)	R-3m	4.119[17] 4.126[18]	22.84 22.89	0.2319	3.32647	2.81145	4.643	2.986
$RbGdS_2$	Rhombohedral (α-$NaFeO_2$)	R-3m	4.098 [17] 4.110[18]	22.88 22.9	0.232	3.31897	2.8052	4.641	2.992
$RbTbS_2$	Rhombohedral (α-$NaFeO_2$)	R-3m	4.070 [17] 4.080[18]	22.80 22.874	0.2315	3.3128	2.7835	4.658	2.966
$RbDyS_2$	Rhombohedral (α-$NaFeO_2$)	R-3m	4.060[18] 4.052[19]	22.885 22.826	0.2312	3.31023	2.77049	4.674	2.954
$RbHoS_2$	Rhombohedral (α-$NaFeO_2$)	R-3m	4.037[18] 4.023[19]	22.844 22.753	0.2309	3.303	2.754	4.680	2.935
$RbErS_2$	Rhombohedral (α-$NaFeO_2$)	R-3m	4.026[18] 4.017[19]	22.802 22.774	0.2311	3.292	2.750	4.662	2.938
$RbTmS_2$	Rhombohedral (α-$NaFeO_2$)	R-3m	4.020[18]	22.838	0.2305	3.302	2.741	4.697	2.915
$RbYbS_2$	Rhombohedral (α-$NaFeO_2$)	R-3m	3.991[18] 3.985[19]	22.717 22.801	0.2308	3.276	2.726	4.658	2.914
$RbLuS_2$	Rhombohedral (α-$NaFeO_2$)	R-3m	3.991[18] 3.973[19]	22.838 22.818	0.2303	3.293	2.724	4.706	2.906
$RbScS_2$	Rhombohedral (α-$NaFeO_2$)	R-3m	3.8299[9]	22.656	0.22811	3.251	2.613	4.768	2.784
$RbYS_2$	Rhombohedral (α-$NaFeO_2$)	R-3m	4.0444[9]	22.8267	0.2309	3.304	2.757	4.676	2.932
$CsLaS_2$	Rhombohedral (α-$NaFeO_2$)	R-3m	4.306[17] 4.303[19]	24.08 24.088	0.2302	3.513	2.918	4.968	3.061
$CsCeS_2$	Rhombohedral (α-$NaFeO_2$)	R-3m	4.262[17] 4.262[19]	23.99 24.025	0.2298	3.499	2.890	4.975	3.033

$CsPrS_2$	Rhombohedral (α-$NaFeO_2$)	R-3m	4.232[19]	24.054	0.2294	3.496	2.872	5.000	3.018
	Hexagonal (β-$RbScO_2$)	P63/mmc	4.237 [19]	16.020					
$CsNdS_2$	Rhombohedral (α-$NaFeO_2$)	R-3m	4.190[19]	23.926	0.2294	3.469	2.847	4.973	3.002
	Hexagonal (β-$RbScO_2$)	P63/mmc	4.205[19]	16.043					
$CsPmS_2$ This Work	Rhombohedral (α-$NaFeO_2$)	R-3m	4.186	24.232	0.2287	3.503	2.846	5.071	3.006
$CsSmS_2$	Rhombohedral (α-$NaFeO_2$)	R-3m	4.161[19]	24.072	0.2285	3.484	2.826	5.047	2.977
	Hexagonal	P63/mmc	4.156[19]	16.011					
$CsEuS_2$	Rhombohedral (α-$NaFeO_2$)	R-3m	4.137[19]	24.026	0.2281	3.478	2.808	5.057	2.952
	Hexagonal (β-$RbScO_2$)	P63/mmc	4.131[19]	15.991					
$CsGdS_2$	Rhombohedral (α-$NaFeO_2$)	R-3m	4.116[19]	24.043	0.2287	3.460	2.805	5.031	2.983
	Hexagonal (β-$RbScO_2$)	P63/mmc	4.111[19]	16.022					
$CsTbS_2$	Rhombohedral (α-$NaFeO_2$)	R-3m	4.102[19]	24.004	0.228	3.464	2.788	5.057	2.945.
	Hexagonal (β-$RbScO_2$)	P63/mmc	4.102 [19]	15.989					
$CsDyS_2$	Rhombohedral (α-$NaFeO_2$)	R-3m	4.058[19]	24.008	0.2276	3.454	2.762	5.077	2.926
	Hexagonal (β-$RbScO_2$)	P63/mmc	4.059[19]	15.980					
$CsHoS_2$	Rhombohedral (α-$NaFeO_2$)	R-3m	4.054[19]	24.001	0.2275	3.454	2.759	5.080	2.920
	Hexagonal (β-$RbScO_2$)	P63/mmc	4.052 [19]	15.995					
$CsErS_2$	Rhombohedral (α-$NaFeO_2$)	R-3m	4.039[19]	24.017	0.2271	3.456	2.747	5.103	2.903
	Hexagonal (β-$RbScO_2$)	P63/mmc	4.041[19]	16.001					
$CsTmS_2$	Rhombohedral (α-$NaFeO_2$)	R-3m	4.022[19]	23.941	0.227	3.446	2.735	5.091	2.889
	Hexagonal (β-$RbScO_2$)	P63/mmc	4.020[19]	15.959					
$CsYbS_2$	Rhombohedral (α-$NaFeO_2$)	R-3m	4.022[19]	23.914	0.2271	3.427	2.713	5.081	2.890
	Hexagonal	P63/mmc	4.022 [19]	15.925					

	(β-$RbScO_2$)								
$CsLuS_2$	Rhombohedral (α-$NaFeO_2$)	R-3m	3.980 [19]	23.91	0.227	3.442	2.735	5.085	2.885
	Hexagonal (β-$RbScO_2$)	P63/mmc	3.980 [19]	15.951					
$CsScS_2$ This Work	Rhombohedral (α-$NaFeO_2$)	R-3m	3.877	23.886	0.2242	3.436	2.626	5.213	2.748
$CsYS_2$ This Work	Rhombohedral (α-$NaFeO_2$)	R-3m	4.081	24.133	0.2272	3.480	2.772	5.123	2.922

Table (S02): Ionic Radii of A^{+} and B^{+3} for coordination number six [20]

atom	**Ionic Radii**
Li^{+1}	0.90
Na^{+1}	1.16
K^{+1}	1.52
Rb^{+1}	1.66
Cs^{+1}	1.81
La^{3+}	1.172
Ce^{3+}	1.15
Pr^{3+}	1.13
Nd^{3+}	1.123
Pm^{3+}	1.11
Sm^{3+}	1.098
Eu^{3+}	1.087
Gd^{3+}	1.078
Tb^{3+}	1.063
Dy^{3+}	1.052
Ho^{3+}	1.041
Er^{3+}	1.030
Tm^{3+}	1.020
Yb^{3+}	1.008
Lu^{3+}	1.001
Sc^{3+}	0.885
Y^{3+}	1.040

References

[1]R. Ballestracci, Étude cristallographique de nouveaux sulfures de terres rares et de métaux alcalins M= Li, K, Bulletin de Minéralogie, 88 (1965) 207-210.

[2]T. Ohtani, H. Honjo, H. Wada, Synthesis, order-disorder transition and magnetic properties of LiLnS2, LiLnSe2, NaLnS2 and NaLnSe2 (Ln= Lanthanides), Materials Research Bulletin, 22 (1987) 829-840.

[3]M. Palazzi, Etude du composé EuLiS2 et des phases non stœchiométriques dérivées contenant de l'europium à valence mixte, Comptes rendus de l'Académie des sciences. Série 2, Mécanique, Physique, Chimie, Sciences de l'univers, Sciences de la Terre, 303 (1986) 33-36.

[4]M. Guymont, A. Tomas, M. Palazzi, Short-range order in EuLiS2 by electron microscopy, physica status solidi (a), 118 (1990)40-29

[5]C. Plug, A. Prodan, Long-and short-range ordering in LiTbS2, Acta Crystallographica Section A: Crystal Physics, Diffraction, Theoretical and General Crystallography, 34 (1978) 250-253.

[6]M. TROMME, SYNTHESIS AND CRYSTALLOGRAPHIC STUDY ON NEW ABS2 COMPOUNDS WITH ALPHA NAFEO2 STRUCTURE, COMPTES RENDUS HEBDOMADAIRES DES SEANCES DE L ACADEMIE DES SCIENCES SERIE C, 273 (1971) 849-&.

[7]M. Van Dijk, C. Plug, The crystal structure of LiScS2 and NaScS2, Materials Research Bulletin, 1 106-103 (1980) 5.

[8]D. Kipp, T. Vanderah, Synthesis of α-NaFeO2-type LiYS2 by anion-exchange reaction, Materials Research Bulletin, 25 (1990) 933-937.

[9]J. Fábry, L. Havlák, M. Dušek, P. Vaněk, J. Drahokoupil, K. Jurek, Structure determination of KLaS2, KPrS2, KEuS2, KGdS2, KLuS2, KYS2, RbYS2, NaLaS2 and crystal-chemical analysis of the group 1 and thallium (I) rare-earth sulfide series, Acta Crystallographica Section B: Structural Science, Crystal Engineering and Materials, 70 (2014) 360-371.

[10]R. Ballestracci, E.F. Lewy-Bertaut, Étude cristallographique de sulfures de terres rares et de sodium, Bulletin de Minéralogie, 87 (1964) 512-517.

[11]M. Sato, G. Adachi, J. Shiokawa, Preparation and structure of sodium rare-earth sulfides ،NaLnS2 (Ln; rare earth elements), Materials Research Bulletin, 19 (1984) 1215-1220.

[12]T. Schleid, F. Lissner, Single crystals of NaMS2 (M= Ho-Lu) from reactions of the lanthanides with sulfur in the presence of NaCl, European journal of solid state and inorganic chemistry, 30 (1993) 829-836.

[13]K.-J. Range, W. Meister, U. Klement, Crystal structure of sodium ytterbium (III) disulfide, NaYbS2, Zeitschrift für Kristallographie-Crystalline Materials, 207 (1993) 145-146.

[14]J. Fábry, L. Havlák, M. Kučeráková, M. Dušek, Redetermination of nagds2, nalus2 and nays2, Acta Crystallographica Section C: Structural Chemistry, 70 (2014) 533-535.

[15]C. Plug, G. Verschoor, The crystal structure of KCeS2, Acta Crystallographica Section B: Structural Crystallography and Crystal Chemistry, 32 (1976) 1856-1858.

[16]L. Havlak, J. Fábry, M. Henriques, M. Dušek, Structure determination of KScS2, RbScS2 and KLnS2 (Ln= Nd, Sm, Tb, Dy, Ho, Er, Tm and Yb) and crystal–chemical discussion, Acta Crystallographica Section C: Structural Chemistry, 71 (2015) 623-630.

[17]W. Bronger, Ueber ternäre Sulfide mit Lanthanoiden und den Alkalimetallen Rubidium oder Cäsium, (1973) .

[18]W. Bronger, J. Eyck, K. Kruse, D. Schmitz, Ternary rubidium rare-earth sulphides; synthesis and structure, Eur. J. Solid State Inorg. Chem, 33 (1996) 213-226.

[19]W. Bronger, W. Brüggemann, M. Von der Ahe, D. Schmitz, Zur Synthese und Struktur ternärer Chalcogenide der Seltenen Erden AlnX2 mit A≙ alkalimetall und X≙ Schwefel, Selen oder Tellur, Journal of alloys and compounds, 200 (1993) 205-210 DOI.

[20]R.D. Shannon, Revised effective ionic radii and systematic studies of interatomic distances in halides and chalcogenides, Acta Crystallographica Section A: Crystal Physics, Diffraction, Theoretical and General Crystallography, 32 (1976) 751-767 DOI.